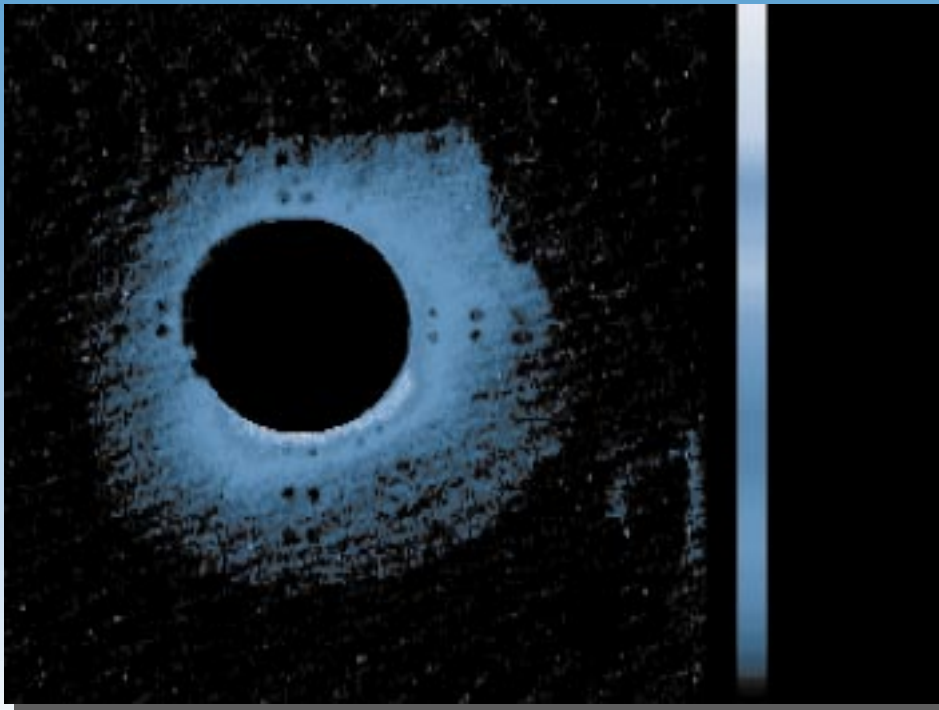


INERTIAL CONFINEMENT FUSION

Lawrence
Livermore
National
Laboratory

ICF Quarterly Report

October—December 1997, Volume 8, Number 1

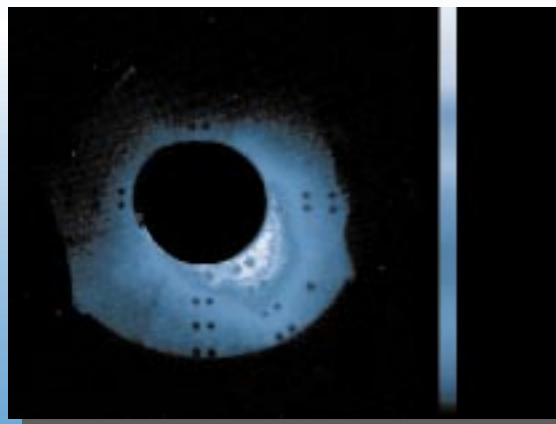


*Hohlraum Radiation-
Drive Measurements
on the Omega Laser*

*Optimization of Beam
Angles for the
National Ignition
Facility*

*High-Energy X-Ray
Microscopy at the
National Ignition
Facility*

*Laser—Electron
Conversion Efficiency
at Intensities Greater
than 10^{19} W/cm²*



*Large-Aperture Color
Separation Gratings
for Diverting
Unconverted Light
Away from the
National Ignition
Facility Target*

*Hohlraum Energetics with Smooth
Laser Beams*

The Cover: These 2D images of backscattered laser light come from stimulated Brillouin scattering off an aluminum scatter plate mounted around the lens of one Nova laser beam. The measurements show the beneficial effect of laser smoothing techniques in reducing beam steering in gas-filled inertial confinement fusion hohlraums. For smoothed laser beams (top picture), a fraction of the incident laser light is scattered back almost straight into the lens (which is represented by the black circle in the center of the image). This observation is a clear improvement over unsmoothed laser beams for which the backscattered laser light is spatially shifted by up to 8° in the lower right direction away from the straight backward direction (lower picture). This shift is an indication of filamentation and deflection (steering) of the laser beams in the underdense plasma of a gas-filled hohlraum. Its reduction for smoothed beams is related to the suppression of filamentation and is important for controlling laser pointing in ignition experiments. This data is described more fully in the article "Hohlraum Energetics with Smooth Laser Beams" on p. 7.

UCRL-LR-105821-98-1
Distribution Category UC-712
October–December 1997

Printed in the United States of America
Available from
National Technical Information Service
U.S. Department of Commerce
5285 Port Royal Road
Springfield, Virginia 22161
Price codes: printed copy A03, microfiche A01.

This document was prepared as an account of work sponsored by an agency of the United States Government. Neither the United States Government nor the University of California nor any of their employees makes any warranty, express or implied, or assumes any legal liability or responsibility for the accuracy, completeness, or usefulness of any information, apparatus, product, or process disclosed, or represents that its use would not infringe privately owned rights. Reference herein to any specific commercial products, process, or service by trade name, trademark, manufacturer, or otherwise, does not necessarily constitute or imply its endorsement, recommendation, or favoring by the United States Government or the University of California. The views and opinions of authors expressed herein do not necessarily state or reflect those of the United States Government or the University of California and shall not be used for advertising or product endorsement purposes.

The ICF Quarterly Report is published four times each fiscal year by the Inertial Confinement Fusion/National Ignition Facility Program at the Lawrence Livermore National Laboratory. The *ICF Quarterly Report* is also on the Web at <http://lasers.llnl.gov/lasers/pubs/icfq.html>. The journal summarizes selected current research achievements of the LLNL ICF/NIF Program. The underlying theme for LLNL's ICF/NIF Program research is defined within DOE's Defense Programs missions and goals. In support of these missions and goals, the ICF/NIF Program advances research and technology development in major interrelated areas that include fusion target theory and design, target fabrication, target experiments, and laser and optical science and technology.

While in pursuit of its goal of demonstrating thermonuclear fusion ignition and energy gain in the laboratory, the ICF/NIF Program provides research and development opportunities in fundamental high-energy-density physics and supports the necessary research base for the possible long-term application of inertial fusion energy for civilian power production. ICF technologies continue to have spin-off applications for additional government and industrial use. In addition to these topics, the *ICF Quarterly Report* covers non-ICF funded, but related, laser research and development and associated applications. We also provide a short summary of the quarterly activities within Nova laser operations, Beamlet laser operations, and NIF laser design.

LLNL's ICF/NIF Program falls within DOE's national ICF program, which includes the Nova and Beamlet (LLNL), OMEGA (University of Rochester Laboratory for Laser Energetics), Nike (Naval Research Laboratory), and Trident (Los Alamos National Laboratory) laser facilities. The Particle Beam Fusion Accelerator and Saturn pulsed power facilities are at Sandia National Laboratories. General Atomics, Inc., develops and provides many of the targets for the above experimental facilities. Many of the *Quarterly Report* articles are co-authored with our colleagues from these other ICF institutions.

Questions and comments relating to the technical content of the journal should be addressed to the ICF/NIF Program Office, Lawrence Livermore National Laboratory, P.O. Box 808, Livermore, CA, 94551.

Work performed under the auspices of the U.S. Department of Energy by Lawrence Livermore National Laboratory under Contract W-7405-Eng-48.

INERTIAL CONFINEMENT FUSION

ICF Quarterly Report October–December 1997, Volume 8, Number 1

In this issue:

Foreword iii

Hohlraum Radiation-Drive Measurements on the Omega Laser 1

This article reports on experiments performed on the Omega laser in which the radiation drive is measured through the laser entrance hole. The measurements are analyzed and compared well with 2D LASNEX simulations. These results increase our confidence in our ability to predict radiation drive in laser driven hohlraums.

Hohlraum Energetics with Smooth Laser Beams 7

The article describes laser backscattering and x-ray drive measurements in gas-filled hohlraums. The experiments show improved energy coupling and reduced backscattering losses to a few percent level for NIF-like laser beam smoothing techniques.

Optimization of Beam Angles for the National Ignition Facility 15

The NIF laser now being built will have 48 beams passing through 72 ports on the target chamber. The locations of the ports have been chosen to optimize the flexibility and performance of the cylindrical indirect-drive option, while allowing direct-drive and tetrahedral indirect-drive experiments to be performed.

High-Energy X-Ray Microscopy at the National Ignition Facility 23

This paper describes analytical and numerical investigations performed to examine and rank x-ray imaging options for the NIF, which is currently under construction at Lawrence Livermore National Laboratory.

Laser–Electron Conversion Efficiency at Intensities Greater than 10^{19} W/cm² 28

High-intensity laser–matter interactions above 10^{19} W/cm² are now experimentally accessible for the first time, and are of great interest because of the possibility of high-gain fusion in the “fast ignitor” concept. This paper presents measurements of the electrons produced by such an intense laser pulse incident on a massive solid target. Total conversion efficiency, mean electron energy, and electron cone-angle measurements are presented, demonstrating the importance of the target material in these high-intensity interactions.

Large-Aperture Color-Separation Gratings for Diverting Unconverted Light Away from the National Ignition Facility Target 33

Color-separation gratings offer a versatile way to diffract the unconverted laser light away from an ICF target. To demonstrate the feasibility of this concept, we have fabricated color-separation gratings at full NIF aperture for use on the Beamlet laser. This article discusses the theory, fabrication, and optical performance of the full-aperture color-separation grating.

Scientific Editor

Michael D. Feit

Publication Editor

Jason Carpenter

Designer

Pamela Davis

Technical Editors

Cindy Cassady
Steve Greenberg
Robert Kirvel
Al Miguel

Classification Editor

Roy Johnson

Art Staff

Norm Calderon-Zablocki
Clayton Dahlen
Sandy Lynn
Kathy McCullough
Janet Orloff

Program Updates

A-1

Publications and Presentations

B-1

FOREWORD

This issue of the *ICF Quarterly Report* focuses on the final section of the 192-arm, 1.8-MJ National Ignition Facility (NIF). We describe both technological advances necessary for optimal utilization of the delivered energy and the hohlraum physics resulting from extremely high energy densities.

Two articles belong to the first category. The conversion of infrared light to ultraviolet occurs at the tripler in the NIF's Final Optics Assembly. It is then necessary to separate any unconverted (first- and second-harmonic) light from the tripled-frequency light passed to the target. "Large-Aperture Color-Separation Gratings for Diverting Unconverted Light Away from the NIF Target" (p. 33) describes the design and fabrication of novel diffraction gratings that fulfill this function. In both direct- and indirect-drive ICF, the symmetry of the capsule as it compresses is crucial. The NIF will have 48 clusters of four beams incident on targets. "Optimization of Beam Angles for the National Ignition Facility" (p. 15) presents the rationale used to assign beam angles for cylindrical indirect drive while still allowing direct-drive and tetrahedral indirect-drive experiments to be performed.

The high-energy environment near the NIF target complicates high-spatial-resolution x-ray microscopy, which has proved very useful in ICF studies. "High-Energy X-Ray Microscopy at the National Ignition Facility" (p. 23) investigates target-mounted pinholes and reflective-optic imaging systems as short- and long-term approaches. "Hohlraum Radiation-Drive Measurements on the Omega Laser" (p. 1) combines experiments and computer simulations to clarify previous discrepancies between radiation temperatures measured through side holes on cylindrical hohlraums with those predicted from simulations. Side-hole measurements "see" a limited area of the opposite hohlraum wall and miss some laser hot spots that contribute significantly to the radiation temperature. The new results indicate the considerable advantage of measuring radiation temperature through the laser entrance hole (LEH) rather than through a side hole. Measurements made through the LEH are in much better agreement with simulations. "Hohlraum Energetics with Smooth Laser Beams" (p. 7) correlates measured radiation temperature with losses due to stimulated Brillouin scattering and stimulated Raman scattering. Our results demonstrate that beam smoothing with kinoform phase plates and smoothing by spectral dispersion is successful in limiting such scattering losses in low- Z , gas-filled hohlraums to a few percent at a laser intensity of $2 \times 10^{15} \text{ W/cm}^2$ and only 7% at an intensity of $4 \times 10^{15} \text{ W/cm}^2$.

The "fast ignitor" approach to laser fusion uses an ultrashort, intense laser pulse to create forward-directed "hot electrons" in the coronal plasma surrounding a target precompressed by another laser pulse. At the high laser intensities involved (on the order of 10^{19} W/cm^2), plasma electrons oscillate at relativistic energies. The feasibility of such a scheme depends, in part, on the efficiency with which laser energy can be transferred to forward-directed plasma electrons. "Laser-Electron Conversion Efficiency at Intensities Greater than 10^{19} W/cm^2 " (p. 28) presents the first experimental demonstration of 30 to 40% conversion for 400-fs pulses of intensity 2 to $4 \times 10^{19} \text{ W/cm}^2$.

Michael D. Feit
Scientific Editor

HOHLRAUM RADIATION-DRIVE MEASUREMENTS ON THE OMEGA LASER

<i>C. Decker</i>	<i>P. Amendt</i>	<i>J. Wallace*</i>	<i>G. R. Magelssen*</i>	<i>D. Bradley**</i>
<i>R. E. Turner</i>	<i>H. N. Kornblum</i>	<i>N. D. Delamater*</i>	<i>J. A. Oertel*</i>	<i>W. Seka**</i>
<i>O. L. Landen</i>	<i>B. A. Hammel</i>	<i>P. Gobby*</i>	<i>J. Knauer**</i>	<i>J. M. Soures**</i>
<i>L. J. Suter</i>	<i>T. J. Murphy*</i>	<i>A. A. Hauer*</i>	<i>F. J. Marshall**</i>	

Introduction

In the laser-driven, indirect-drive fusion scheme,¹ laser beams are focused through the laser entrance holes (LEHs) onto the inside wall of a high-Z enclosure (hohlraum). The laser light is absorbed and converted into soft x rays that fill the hohlraum. These x rays heat a target capsule in the center so rapidly that ablation of the outer surface occurs. The rocket-like outward expansion of this material causes a reaction—an inward implosion of the remaining capsule material. For this reason, the x-ray radiation is referred to as the drive. Detailed knowledge of the radiation drive is of great interest and has been the objective of many hohlraum experiments over the last decade.^{2–6} The radiation is often characterized by a radiation temperature, T_r , which is defined by equating the total frequency-integrated radiation flux to a blackbody flux, $\sigma(T_r)^4$, where σ is the Stefan–Boltzmann constant.

Time-dependent radiation temperatures have been measured extensively on Lawrence Livermore National Laboratory’s Nova⁷ laser using an absolutely calibrated, filtered diode array called Dante.^{8,9} In the Nova experiments, the Dante diagnostic was set up to measure the radiation flux emerging from a hole in the side of a hohlraum with a Dante angle (θ_D in Figure 1) of 90°. Because this method only measures the radiation flux coming off the indirectly heated wall opposite the hole, the flux must be divided by the wall’s effective reflectivity, or albedo, to obtain the true radiation temperature near the wall.^{4,9} The albedo depends upon the material opacity, which varies with time, and must be calculated analytically or numerically. Although the peak temperatures measured through the “side holes” agree well with simulations,⁹ at early times the simulations underestimate the drive. This discrepancy has been attributed to

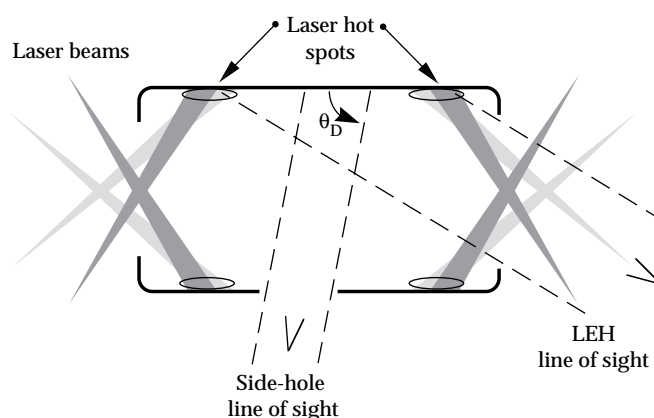


FIGURE 1. A typical laser fusion hohlraum showing the Dante diagnostic’s lines of sight through the side hole and the LEH. (50-00-0598-1159pb01)

uncertainties in the low-temperature opacities, and to scattered or reflected laser light hitting that part of the wall being measured.

The opacity is determined using an average atom model called XSN.¹⁰ At high temperatures (>200 eV), the wall losses modeled with XSN are quite close to those calculated with the more sophisticated STA^{11,12} model and with experiments.^{13,14} However, XSN opacity multipliers of 1.5 are needed to agree with the STA estimates at lower temperatures (<150 eV).¹⁵ The early time drive can also be recovered using a 1.5 multiplier on the XSN opacity and allowing 10% of the laser light to strike the wall, or by using a factor-of-three multiplier with no incident laser light.

Recently, proof-of-principle hohlraum experiments have been done at the Laboratory for Laser Energetics’ Omega laser facility. As many as 40 of Omega’s 60 beams irradiated Nova-scale hohlraums with up to 20 kJ of 351-nm wavelength light, delivered in a 1-ns flat-top pulse.^{16,17} Unlike experiments on Nova with a single

*Los Alamos National Laboratory, Los Alamos, NM

** Laboratory for Laser Energetics, University of Rochester, Rochester, NY

laser cone at an angle of 50° relative to the hohlraum axis, the laser beams for these experiments were distributed into three cones at angles of 21° , 42° , and 59° .

Thin-wall hohlraums were used to limit debris in the chamber and to allow both the laser spots and the imploded cores to be imaged.¹⁸ These hohlraums were constructed with $2\text{-}\mu\text{m}$ Au interior walls with a $100\text{-}\mu\text{m}$ -thick CH external overcoat for structural support. Their inside diameters were $1600\text{ }\mu\text{m}$; their lengths varied from 2100 to $2800\text{ }\mu\text{m}$, and some had a $500\text{-}\mu\text{m}$ -diam diagnostic hole drilled through their side.

In this article, we report on drive measurements and present 2D LASNEX¹⁹ simulations of these experiments. (Details about hohlraum simulations with LASNEX can be found in Reference 5.) In order to link this work to previous Nova experiments, we used the traditional side-hole technique,⁴ and also measured the radiation flux through the LEH for the first time. Our experimental results and simulations indicate that the drive measurements made through the LEH are superior to those done through the side-hole. There is good agreement between the LEH experimental data and the simulations. In particular, the early time discrepancy seen in previous Nova experiments is no longer there. Furthermore, our simulations suggest that the radiation flux emerging from the LEH might be more representative of the drive on the capsule, because the line of sight through the LEH sees both the wall and the laser hot spots (Figure 1) as the capsule does, whereas the side hole's line of sight only allows sampling the indirectly heated wall.

Experiments

The Dante diagnostic,⁸ which measures the radiation flux, is a ten-channel array of absolutely calibrated x-ray vacuum photodiode detectors combined with Al, Cr, and Ni photocathodes. Various thin filters and grazing-incidence mirrors are placed in front of the detectors, giving each channel a significant response in different parts of the spectrum. The spectral coverage ranges from 50 eV to 3000 eV, and the diodes' outputs are recorded on 5-GHz bandwidth oscilloscopes. The system has a temporal response on the order of 200 ps. The data is analyzed (at 100-ps intervals) to find a smoothed spectrum that is consistent with the signal from each channel. Because the channels have some overlap in their spectral coverage, the task of smoothing the spectrum is well constrained. While some variation is possible in the details of the spectrum (by varying the amount of smoothing allowed), the integral over all energies changes little with these variations. As mentioned earlier, this flux (watts per steradian [W/sr] from a hole of known area and view angle) is conveniently characterized by a radiation temperature T_r , even though the smoothed spectrum is not necessarily Planckian (as shown later). To ensure that the Dante diagnostic was collecting radiation only along the direct line of sight and that a negligible amount of radiation was

reaching it through the thin Au walls, shots with hohlraums having no diagnostic side hole were also measured from the side.

For some drive measurements, the radiation temperature was measured through the side hole ($\theta_D = 79^\circ$ in Figure 1). The hohlraums used were $2800\text{ }\mu\text{m}$ long and were shot with 15 kJ of energy, using the two laser cones at 42° and 59° . Because T_r was only measured through the side hole in the Nova shots, Nova experiments complementary to those done with Omega (using identical thin-walled hohlraums at a similar laser power) were also done. The T_r measurements for the Omega and Nova thin-walled hohlraums and the simulated temperatures are shown in Figure 2.

The 10-eV difference between the Omega and Nova shots is due to beam-pointing differences. This difference is predicted both by the simulations and by simple view-factor calculations. The T_r measured on Omega is colder, because the laser spots are further from the mid-plane area viewed by Dante. The simulations for the thin-walled hohlraums are similar at early times to those done previously for thick-walled ($25\text{-}\mu\text{m}$ Au-wall) Nova hohlraums⁹ in that they also underestimate the temperature. However, we also found that the peak temperatures from the thin-walled hohlraums from both Omega and Nova were consistently 10 to 20 eV below their predicted values. This result contrasts with that for the thick-walled Nova hohlraums, where the simulated peak T_r was always within a few eV of the experiment.^{4,9}

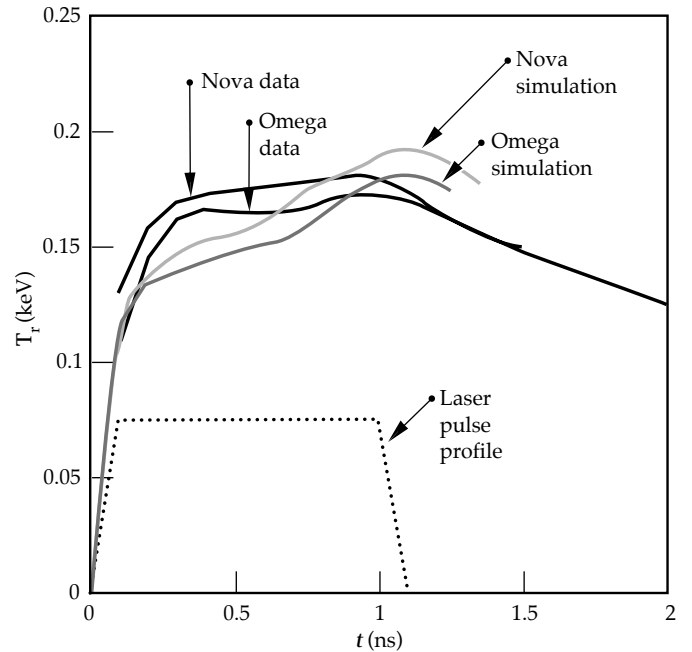


FIGURE 2. Radiation temperatures of Omega and Nova experiments taken from the hohlraums' side-hole line of sight (black lines) and the corresponding LASNEX simulations (gray lines). (50-00-0598-1160pb01)

From these thin-walled hohlraum experiments, it might appear that they are cooler than their thick-walled counterparts.^{4,9} However, simulations for hohlraums with Au wall thickness of 2 μm and 25 μm give identical radiation temperatures. This result is consistent with previous simple estimates¹ showing that the burn-through time for 2 μm of Au, at $T_r = 200$ eV, is on the order of 2 ns, which is longer than the laser pulse's duration. Moreover, as we will show, temperatures measured through the LEH are indeed as hot as predicted.

We now believe that the discrepancy in peak T_r , as measured through the side-hole, is due to the way the holes were fabricated rather than to the wall thickness. For the thick-walled hohlraums used in previous Nova experiments, the side holes were lined with Be washers to prevent them from closing up. In contrast, the side holes on the thin-walled hohlraums were not lined. They were simply drilled straight through, which makes the hole more susceptible to closure and tunnel obstruction effects.

Experiments on Nova were recently done with thick-walled hohlraums having holes constructed in the same way as those of the thin-walled hohlraums. Their peak temperatures were also consistently 10 to 12 eV below predictions. These experiments clearly showed that how the hole is fabricated has an effect on the measurements.

However, rather than dwelling on improvements to the diagnostic side hole, we decided to investigate a new method of measurement. We chose to measure the radiation temperature through the LEH.

Due to the "soccer ball" symmetry of Omega,²⁰ many hohlraum orientations give an identical laser irradiation pattern. In one orientation, the Dante diagnostic viewed the hohlraum through the LEH at an angle of 37.4°. Besides measuring a flux that is more representative of the capsule drive, other practical advantages result from this measurement technique:

- Because the LEH is 2.5 times larger than the diagnostic hole, hole closure should be a less significant problem.
- The LEH viewing method is less invasive; a hole in the side of the hohlraum disturbs the cylindrical symmetry (which is amenable to 2D modeling) and adds to the radiation losses.
- The laser-heated blowoff seen through the LEH is hotter and less dense than the blowoff seen through the side hole; it should therefore be more transparent to the x-ray radiation that we are measuring.
- Typically, the capsules block Dante's view of the wall across from the side hole, but LEH measurements can be made simultaneously with the implosions.
- Viewing the laser hot spots gives better measurements of hard x rays.

Comparison to Simulations

Figures 3a and 3b show the radiation temperatures as measured through the LEH (along with the corresponding simulation data) for a 2100- μm - and a 2300- μm -long hohlraum, respectively. Each shot had an energy of 15 kJ, but with 42° and 59° cone angles, respectively. There is good agreement between simulation and experimental data over the duration of the laser pulse. In particular, there is good agreement at early times. At 300 ps, the simulated and measured temperatures agree to within 5 eV. By comparison, there is a 20-eV discrepancy when the temperature is measured through the diagnostic hole in the side of the hohlraum, as described in the previous section. The insert in Figure 3b plots a typical measured spectrum, showing its non-Planckian distribution due to line emission in the coronal plasma.

The good agreement during the laser pulse between measurements through the LEH and the simulations indicates that we are accurately modeling the physics of the laser hot spot. When viewing the 2100- μm -long hohlraum at 37° through the LEH, we "see" six laser spots. These spots constitute 28% of the wall area under observation, which, in turn, equals 12% of the interior surface. However, simulations show that at $t = 300$ ps these laser hot spots account for over 70% of the flux. Therefore, at early times the radiation flux seen by the capsule and through the LEH is dominated by the laser-irradiated hot spots. At peak drive, the flux from the indirectly heated wall exceeds that from the hot spots. There is still good agreement up to 1.3 ns, because the indirectly heated wall is hot and correctly modeled.

Beyond this time, modeling and experiment diverge. However, with arguments based on energetics, it is difficult to explain how a hohlraum could continue to cool so rapidly. For this reason, we suspect that this late time discrepancy might be related to opacity modeling in the rapidly cooling plasma accumulating at the LEH. Indeed, more sophisticated opacity models¹¹ show that the plasma in the LEH becomes more opaque in the thermal x-ray region than is predicted by the XSN model used in the simulations.

The good agreement between experiment and simulation is also seen for longer-duration, shaped laser pulses. In order to study time-dependent symmetry, several shots were done with a 2-ns stepped, shaped pulse. For these shots, the Dante diagnostic measured the radiation temperature through the LEH. In Figure 4, we show these measurements, along with the data from corresponding simulations. The shape of the laser pulse is shown in Figure 4a. For these longer pulses, there is sufficient time for the Au plasma ablating from the wall to fill the hohlraum.

LASNEX simulations indicate that electron densities between 10 and 20% of the critical density for 0.351- μm light ($9 \times 10^{21} \text{ cm}^{-3}$) are achieved. As a result of this plasma filling, there was a substantial

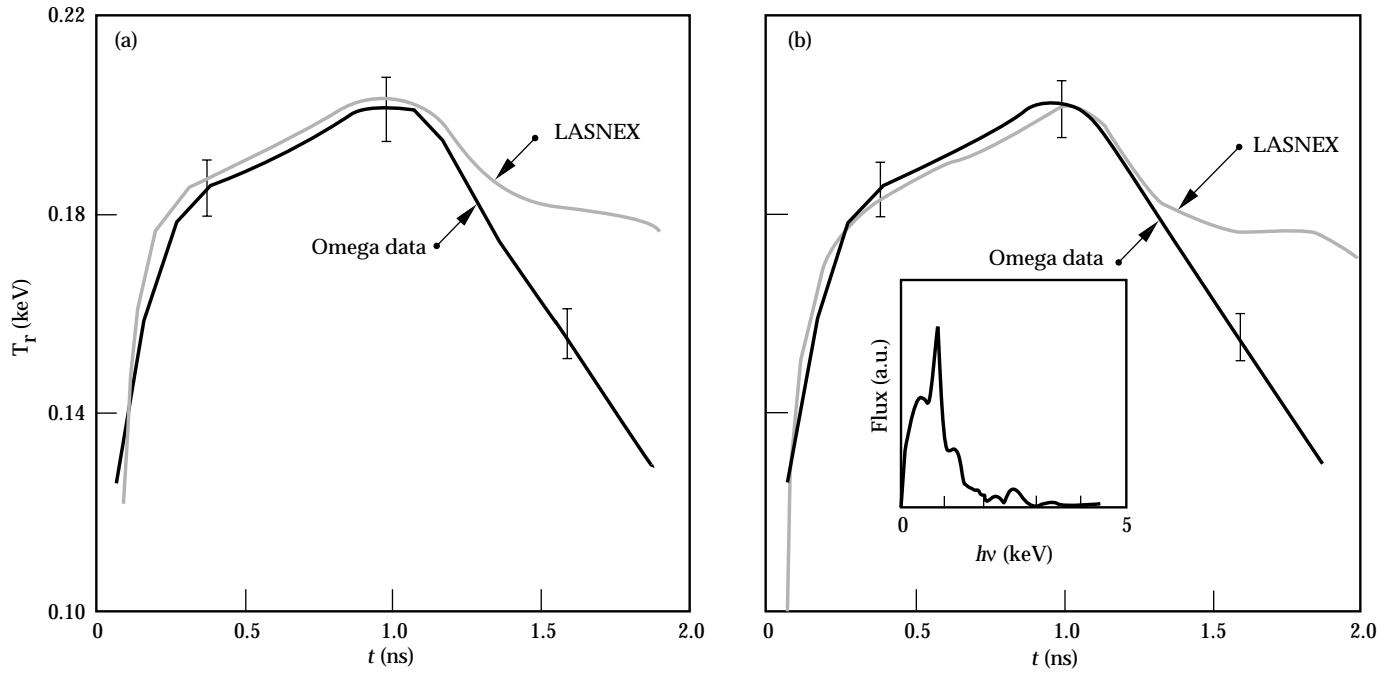


FIGURE 3. Radiation temperature seen through the LEH (black line) and the corresponding LASNEX simulations (gray line) for hohlraum lengths of (a) 2100 μm and (b) 2300 μm . (The error bars show the 3% uncertainty in T_r that is typical for Dante measurements.) Insert in (b): spectrum of the radiation flux at 1.0 ns. (50-00-0598-1161pb01)

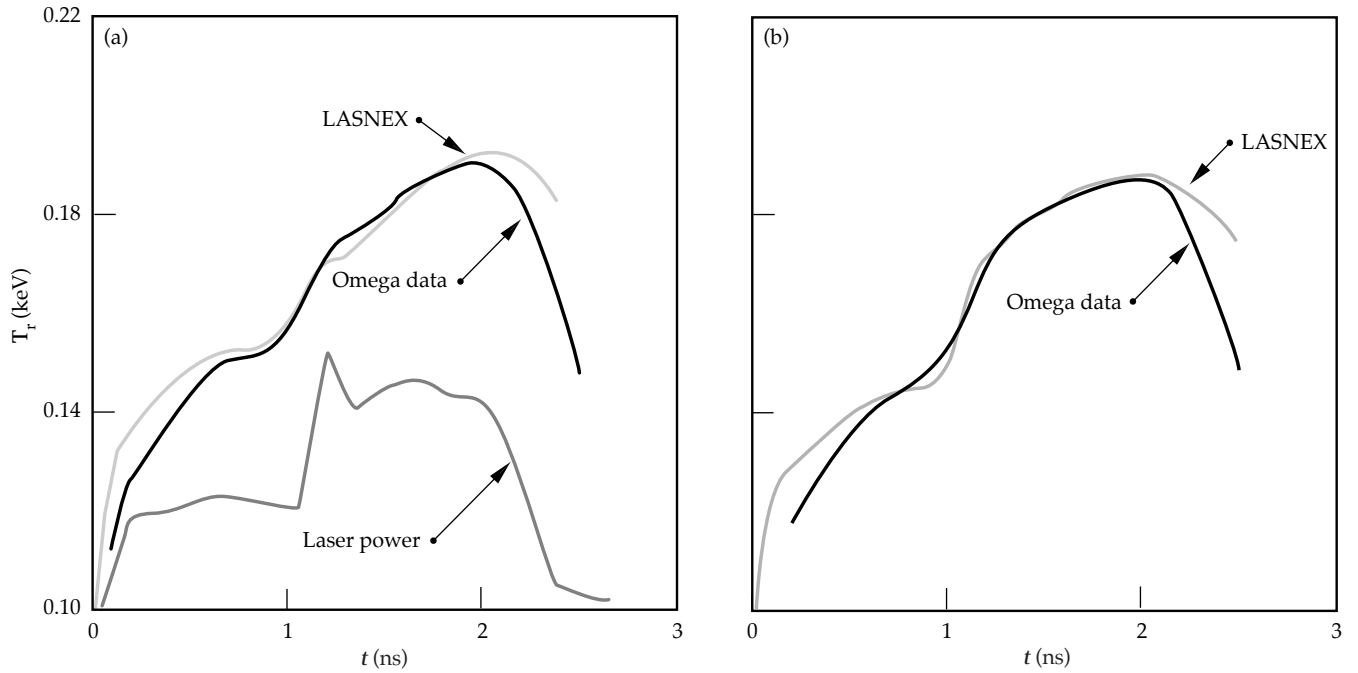


FIGURE 4. Radiation temperature seen through the LEH (black line) along with the LASNEX simulation (gray line) for stepped, shaped laser pulses. The hohlraum lengths are (a) 2100 μm and (b) 2200 μm , respectively. The laser power, shown as the dark gray line in (a), is given in arbitrary units to show the pulse shape. (50-00-0598-1162pb01)

amount of measured stimulated Brillouin scattering (SBS) backscatter (10 to 20%). By comparison, the backscatter levels for the 1-ns pulses were always below a few percent. In the simulations, we reduced the incident laser power consistent with the measured backscattered levels over the second nanosecond of the laser pulse. Once again, as shown in Figure 4, there is a good agreement between the experiments and simulations.

Analysis of the LEH Line of Sight

We now examine how the radiation flux on the capsule compares to that emerging through the LEH in simulations. Consider a 2100- μm -long hohlraum being driven by 15-kJ laser at cone angles of 42° and 59° . In Figure 5 we have plotted the simulated temperatures of the flux on the capsule, of the flux through the LEH at 37.4° , of the flux through the side hole, and of the total flux (integrated over all angles) leaving the LEH. Our plot shows that the total LEH flux provides the measurement closest to the actual capsule drive. Next closest is the single line-of-sight LEH measurement at 37.4° , which is a bit higher than the capsule flux—but much closer than the single line-of-sight measurement made through the side hole.

In general, inferring true capsule drive from measurements made along any single line of sight requires albedo/geometry corrections. However, the simulated and experimental temperatures are in much better agreement for the LEH line-of-sight measurement, and it requires less correction than does the side-hole line of sight. For these reasons, we believe that temperature measurements through the LEH are more representative of the drive on the capsule.

Finally, we looked at the angular dependence of the radiation flux [$\sim(T_r)^4$] through the LEH. In Figure 5, the black lines in the insert are polar plots of the intensity per steradian (I/sr) of the radiation emerging from the simulated LEH (in arbitrary units) at 300 ps and 1 ns. For contrast, the gray lines show the Lambertian I/sr with the same integrated power (171 eV and 199 eV). A Lambertian intensity assumes a uniform wall temperature; the angular dependence comes from the projected area of the hole.

At small polar angles, where the diagnostic views the opposite LEH, the simulated LEH's I/sr is much less than the equivalent Lambertian. The intensity rises rapidly as the LEH line of sight begins to view an admixture of re-emitting wall and hot spots. The

simulated I/sr then drops roughly as the cosine of the polar angle ($\cos \theta$), since the projected area of the LEH decreases at larger angles.

At later times, when the wall albedo has risen and the emission is not so dominated by hot spots, the I/sr at angles greater than 25° from the polar axis is approximately Lambertian. Consequently, measurements made from any larger angle would provide fairly representative data about the total radiation energy escaping from the LEH.

At earlier times, when the hot spots dominate, the I/sr has more structure. A better diagnostic technique for measuring the capsule drive, especially at earlier times, would be to measure emission at several angles, thereby allowing us to properly perform the angular integration. We have long-term plans to develop such a diagnostic array.

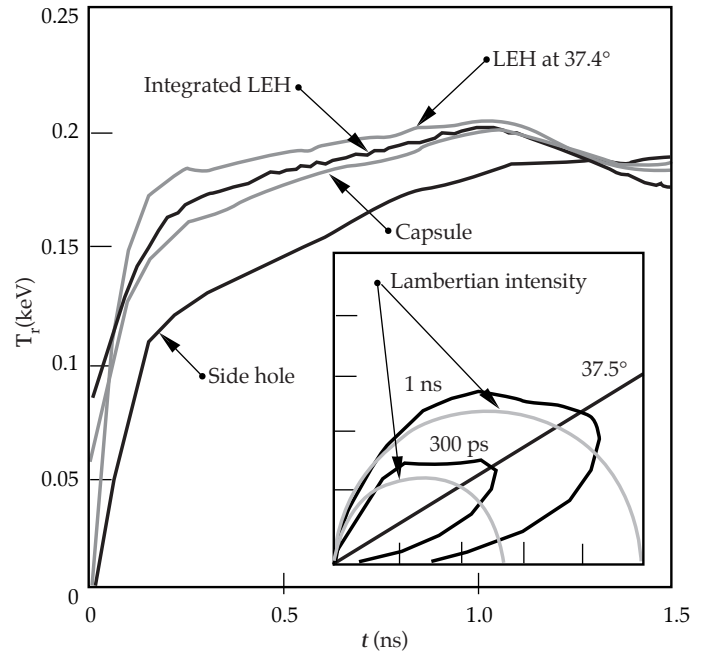


FIGURE 5. A simulation of the flux $T_r(t)$ onto the capsule compared to the flux as seen through the LEH at 37.4° , the total flux out of the LEH (integrated over all angles), and the total flux through the side hole. Insert: The radiation flux out of the LEH (in arbitrary units) vs the viewing angle, at two times, in polar coordinates. The equivalent Lambertian fluxes (light gray lines) are also shown.

(50-00-0598-1163pb01)

Conclusions

Measuring the radiation drive through the LEH appears to be a much better diagnostic of the drive than is measuring through a side hole. At the LEH, hole closure, uncertainties in the low-temperature opacity, and stray laser light do not appear to be the problems they are at the side hole. Moreover, the raw (uncorrected) temperature is more representative of the capsule drive. We plan to develop this method further to allow measuring future hohlraums, such as those that will be used at the National Ignition Facility.

Acknowledgments

We wish to acknowledge our useful conversations with M. Rosen, and the help given by C. Barnes and R. Watt in the proposal of and preparation for the indirect-drive experiment.

References

1. J. Lindl, *Phys. of Plasmas* **2**, 3933 (1995).
2. R. Sigel, R. Pakula, S. Sakabe, and G. D. Tsakiris, *Phys. Rev. A* **38**, 5779 (1988).
3. H. Mishimura et al., *Phys. Rev. A* **44**, 8323 (1991).
4. R. L. Kauffman et al., *Phys. Rev. Lett.* **73**, 2320 (1994).
5. L. J. Suter et al., *Phys. Rev. Lett.* **73**, 2328 (1994).
6. A. Hauer et al., *Rev. Sci. Instrum.* **66**, 672 (1995); R. L. Kauffman et al., *Rev. Sci. Instrum.* **66**, 678 (1995).
7. E. M. Campbell et al., *Rev. Sci. Instrum.* **57**, 2101 (1986).
8. H. N. Kornblum, R. L. Kauffman, and J. A. Smith, *Rev. Sci. Instrum.* **57**, 2179 (1986).
9. L. J. Suter et al., *Phys. of Plasmas* **3**, 2057 (1996).
10. D. E. Post et al., *Atom. Data Nucl. Data Tables* **20**, 397 (1977).
11. A. Bar-Shalom et al., *Phys. Rev. E* **51**, 4882 (1995).
12. A. Bar-Shalom et al., *Phys. Rev. A* **40**, 3183 (1989).
13. J. L. Porter et al., *ICF Quarterly Report* **4**(4), 125 (1994).
14. T. J. Orzechowski et al., *Phys. Rev. Lett.* **77**, 3545 (1996).
15. M. D. Rosen, *Phys. of Plasmas* **3**, 1806 (1996).
16. J. M. Soures et al., *Bul. Am. Phys. Soc.* **41**, 1420 (1996).
17. T. J. Murphy et al., *Bul. Am. Phys. Soc.* **41**, 1420 (1996).
18. N. D. Delamater et al., *Phys. of Plasmas* **3**, 2202 (1996).
19. G. Zimmerman and W. Kruer, *Comments Plasma Phys.* **11**, 51 (1975).
20. J. D. Schnittman and R. S. Craxton, *Phys. of Plasmas* **3**, 3786 (1996).

HOHLRAUM ENERGETICS WITH SMOOTH LASER BEAMS

S. H. Glenzer

B. A. Hammel

*M.-C. Monteil**

G. F. Stone

R. L. Berger

R. L. Kauffman

J. D. Moody

L. J. Suter

*M. A. Blain**

R. K. Kirkwood

T. J. Orzechowski

R. E. Turner

S. N. Dixit

O. L. Landen

D. M. Pennington

T. L. Weiland

K. G. Estabrook

B. J. MacGowan

Introduction

The controlled and efficient coupling of laser or ion-beam energy to a fusion target is a key issue in inertial confinement fusion research. In the indirect-drive approach,^{1,2} current ignition designs for the National Ignition Facility (NIF) use high-Z hohlraums as radiation enclosures that are heated with shaped, high-power laser beams with more than 1-MJ energy. At the inner wall of the hohlraum, the heater beam power is converted into soft x rays characterized by a radiation temperature T_{rad} (Refs. 3–6). The x rays drive the implosion of the fusion capsule by x-ray ablation pressure. Integrated radiation-hydrodynamic LASNEX simulations of both the hohlraum and capsule conditions show a significant fusion yield of 16 MJ when using hohlraums filled with a low-Z gas.^{2,7,8} The gas inhibits movements of the laser absorption and x-ray emission region and prevents early axial stagnation of the high-Z plasma blowoff. These are important properties of gas-filled hohlraums for maintaining radiation symmetry and a symmetric, high-convergence, high-yield implosion of the fusion capsule.

We present complementary measurements of radiation temperatures and stimulated scattering losses arising from stimulated Brillouin scattering (SBS) and stimulated Raman scattering (SRS)^{9,10} from laser-driven, ignition-type hohlraums. We show that the x-ray production in gas-filled hohlraums is reasonably well described by radiation-hydrodynamic LASNEX^{11,12} modeling and by scaling laws¹³ when taking into account the scattering losses. The experiments further show that laser-beam smoothing techniques are successful for the controlled and efficient production of ignition-relevant hohlraum plasmas. This result was obtained with two different laser pulse shapes. One resulted in laser intensities of 2×10^{15} W/cm² to study

hohlraums heated with the same intensities as those planned for the NIF. In addition, hohlraum conditions were investigated with a second laser pulse shape with higher intensities, reaching 4×10^{15} W/cm², to investigate scalings and the physics of high-temperature hohlraums.

In this study, we demonstrate that SBS and SRS losses from hohlraums heated with intensities of 2×10^{15} W/cm² can be controlled and reduced to the 3% level by applying laser-beam smoothing techniques. For higher heater-beam intensities of 4×10^{15} W/cm², the best smoothing condition resulted in a maximum loss of 7%. These findings are consistent with experimental observations and calculations showing that filamentation and gain for SBS and SRS are reduced in hohlraum plasmas by the suppression of hot spots in the smoothed laser beams. In the 2×10^{15} W/cm² case, the radiation temperature increases by ~ 15 eV, showing clear evidence of improved laser-energy coupling into the hohlraum. Table 1 identifies the acronyms used in this article.

TABLE 1. List of acronyms and definitions.

FABS	full-aperture backscattering diagnostic
KPP	kinoform phase plate
LEH	laser entrance hole
NBI	near-backscattering imager
NIF	National Ignition Facility
PCD	photoconductive detector
PS22	pulse shape number 22: 7-TW foot to 17-TW peak power, total energy ≈ 29 kJ (see Figure 6b)
PS26	pulse shape number 26: 5-TW foot to 25-TW peak power, total energy ≈ 31 kJ (see Figure 7c)
RPP	random phase plate
SBS	stimulated Brillouin scattering
SRS	stimulated Raman scattering
SSD	smoothing by spectral dispersion

*Centre D'Etudes de Limeil-Valenton, Villeneuve Saint-Georges, France

Experiment

The experiments were performed at the Nova laser facility at Lawrence Livermore National Laboratory.¹⁴ As shown in Figure 1, we used cylindrical hohlraums that were 2.75 mm long and 1.6 mm in diameter, the standard size for capsule implosions^{15,16} and current benchmarking experiments^{17–19} at Nova. On each side, five laser beams enter the hohlraum through laser entrance holes (LEHs). In addition to empty hohlraums, we shot hohlraums filled with 1 atm of methane (CH_4) and used 0.35- μm -thick polyimide to cover holes. The hohlraums were heated with a total of ten shaped laser beams of 2.4-ns duration. The pulses rose from a 7-TW foot to 17-TW peak power (pulse shape number 22, hereafter PS22) or from 5 TW to 25 TW (pulse shape number 26, PS26). Total energies supplied to the target were 29 kJ and 31 kJ, respectively.

Experiments were performed with standard, unsmoothed Nova beams and with two types of beam-smoothing conditions. The beams were smoothed by using kinoform phase plates (KPPs),^{20,21} which break each beam into many several-millimeter-scale beamlets. The diffraction-limited focal spots are then superposed in the target plane, producing an intensity envelope without large scale-length inhomogeneities, but consisting of fine-scale hot spots (speckles). The focal spot was further smoothed through the use of smoothing by spectral dispersion (SSD).²² In essence, the bandwidth of 0.22 nm at 1ω , together with a dispersive grating in the beamline, serves to move the speckles in the focal plane on time scales (~ 5 ps) that are short compared with that required for hot spots to form a filament in the plasma (~ 10 to 20 ps). The configuration resulted in peak laser intensities of 2 to 4×10^{15} W/cm² at the LEHs, values that are comparable to those anticipated in NIF hohlraums (namely, 2×10^{15} W/cm²).

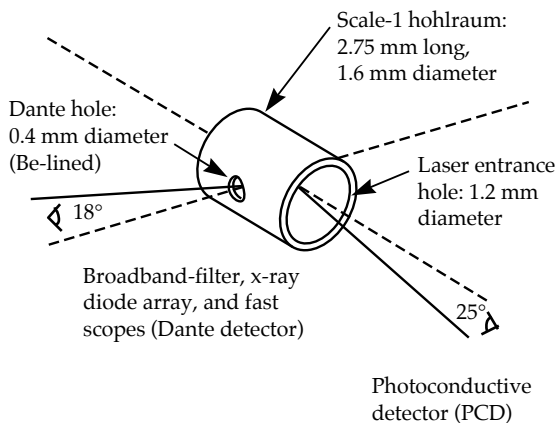


FIGURE 1. Schematic of a hohlraum target showing the views of the detectors. (08-00-0598-1178pb01)

Radiation temperatures were measured with a broadband-filter, x-ray diode array, and fast scopes (Dante detector).²³ This instrument measures the radiation flux per steradian, temporally and spectrally resolved $\phi(t, \nu)$, emitted along the collimated line of sight from the indirectly heated wall opposite a 450- μm -diam diagnostic hole in the side of the hohlraum (see Figure 1). We obtained the hohlraum wall temperature by

$$\nu(t) = \sigma [T_{\text{wall}}(t)]^4 A_d, \quad (1)$$

where $\nu(t)$ is the frequency-integrated radiation flux (0 to 2 keV) emitted from the wall through a diagnostic hole (area A_d), and σ is the Stefan-Boltzmann constant. Closure effects of the diagnostic hole at late times were mitigated using a Be-lined hole. In addition to Dante measurements, we fielded a photoconductive detector (PCD)²⁴ on the PS26 experiments, which provided a radiation-temperature measurement through the 1.2-mm-diam LEH at a polar angle of 25°, for which closure effects are less important.²⁵

We used three independent detection systems for a complete measurement of the scattering losses. Back-scattering into the lens of one of the Nova laser beams was detected with a full-aperture backscattering diagnostic (FABS).²⁶ The light was imaged onto a frosted silica plate and detected temporally and spectrally resolved. For this purpose, we used properly filtered diodes with a temporal resolution of up to ~ 100 ps, a 0.25-m spectrometer for SRS, and a 0.75-m spectrometer for SBS. The spectrometers were equipped with optical streak cameras, resulting in a temporal resolution of ~ 30 ps. The entire detection system was absolutely calibrated in situ by retroreflecting 8% of a full-power laser shot into the detector. Light scattered at larger angles, up to 22°, was measured with a near-backscattering imager (NBI).²⁷ This device consisted of a calibrated Al scatter plate mounted around the lens and 2D imaging detectors for SBS and SRS. Light scattered at larger angles was collected with calibrated diodes.

Experimental Results and Discussion

Figure 2 compares experimental wall temperatures from Dante and time-integrated SBS and SRS losses of CH_4 -filled and empty hohlraums for various beam-smoothing conditions. Data is shown for the PS22 experiments only because no measurements were performed for PS26 without laser-beam smoothing. We observe a clear correlation of these quantities. For gas-filled hohlraums, the total scattering losses are reduced from $18\% \pm 3\%$ for unsmoothed laser beams to $3\% \pm 1\%$ when applying KPPs plus 0.22-nm SSD.

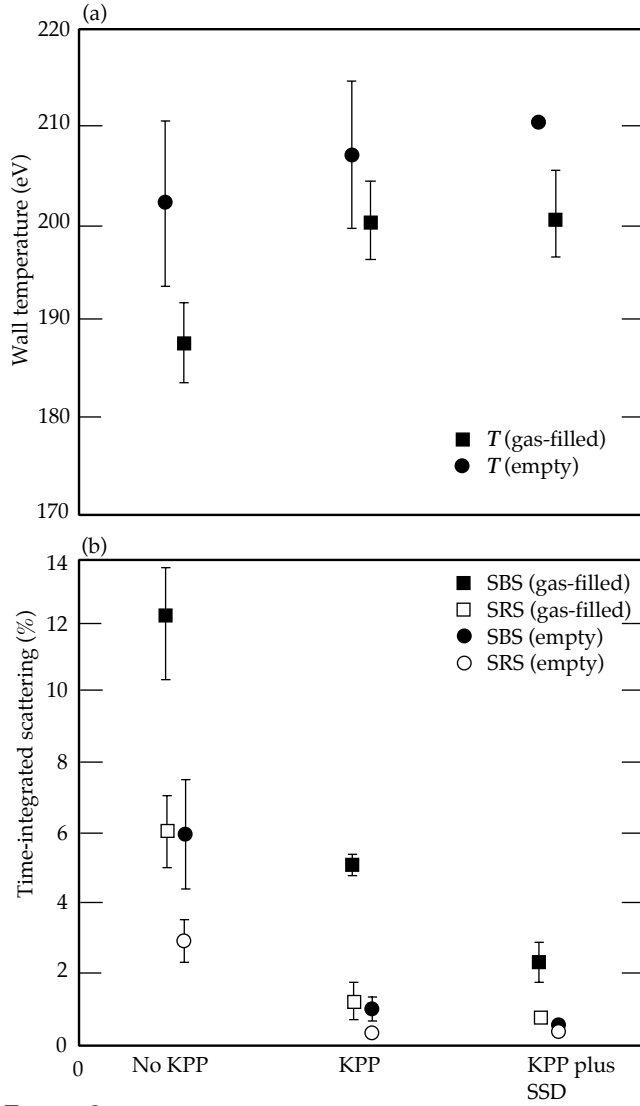


FIGURE 2. (a) Peak hohlraum wall temperatures for various laser beam smoothing conditions. Error bars are rms values. (b) Time-integrated stimulated Brillouin and Raman scattering losses for gas-filled and empty hohlraums. Total energy loss for gas-filled hohlraums decreases from 18% for unsmoothed beams to 4% for beams smoothed with KPP plus SSD. For empty hohlraums, the reduction is from 9 to 1%. (08-00-0598-1180pb01)

Simultaneously, the temperatures increase by 15 eV. These results were found to be insensitive to variations in laser-beam focusing or to the laser power during the low-intensity foot. For hohlraums heated with smoothed laser beams, LASNEX simulations²⁵ show that the Dante-measured radiation temperatures may be 5 eV higher than those for unsmoothed beams merely due to suppression of laser-beam deflection.^{28,29} This result is expected because unsmoothed Nova beams are deflected away from the midplane of the hohlraum, where wall temperatures are measured. The additional 10-eV increase in hohlraum temperatures observed in this study for smoothed laser beams is consistent with the reduction of backscatter losses,

and it is clear evidence of improved energy coupling into the hohlraum.

Our scattering measurements indicate that filamentation of the laser beams is suppressed when applying beam smoothing, thus explaining the low scattering losses in the present experiments. Figure 3 shows SRS spectra at $1.8 \text{ ns} < t < 2 \text{ ns}$ for the various smoothing conditions. The long-wavelength Raman feature at 550 nm plasma originates from plasma regions with $T_e = 3 \text{ keV}$, $n_e = 7 \times 10^{20} / \text{cm}^3$. Using LASNEX simulations of the low-density plasma, which have been benchmarked against Thomson scattering measurements,¹⁹ we find that the scattering at 550 nm arises from the CH plasma in the LEH region of the hohlraum. The width of 30 nm for the best smoothing condition (KPP plus SSD) is consistent with calculations of the damping and growth rate of electron plasma waves using the experimental parameters ($T_e = 3 \text{ keV}$, $n_e = 7 \times 10^{20} / \text{cm}^3$, $\theta = 180^\circ$ angle of observation, $2 \times 10^{15} \text{ W/cm}^2$, and $\lambda_0 = 351.1 \text{ nm}$) in addition to estimates for the length of the interaction using simulated density gradients. The Raman signal at shorter wavelengths, $400 \text{ nm} < \lambda < 530 \text{ nm}$, originates from plasma regions with much lower densities (1 to 7% n_{cr}) than the average density of the methane plasma. The appearance of SRS from such low densities can be interpreted as an indication of filamentation of the laser beams.²⁶ The short-wavelength Raman signal is gradually suppressed with improved beam smoothing because of the reduction of energy in hot spots, which produce filamentation (KPP only), and the reduction of the filamentation rate of hot spots (with additional SSD).

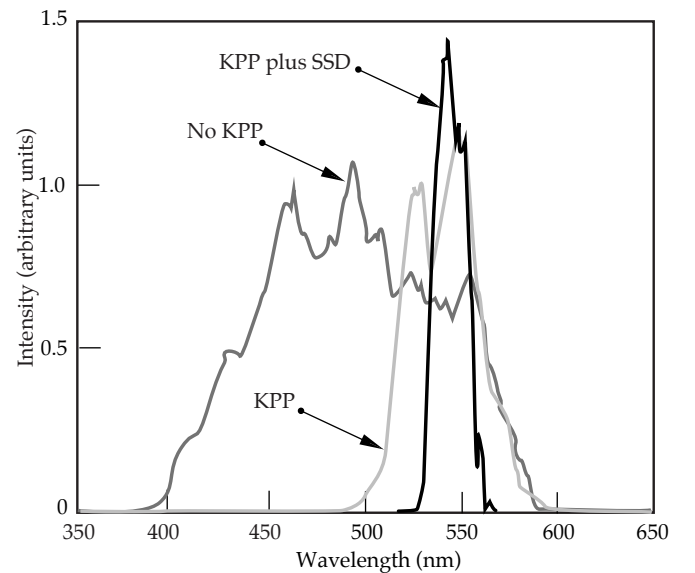
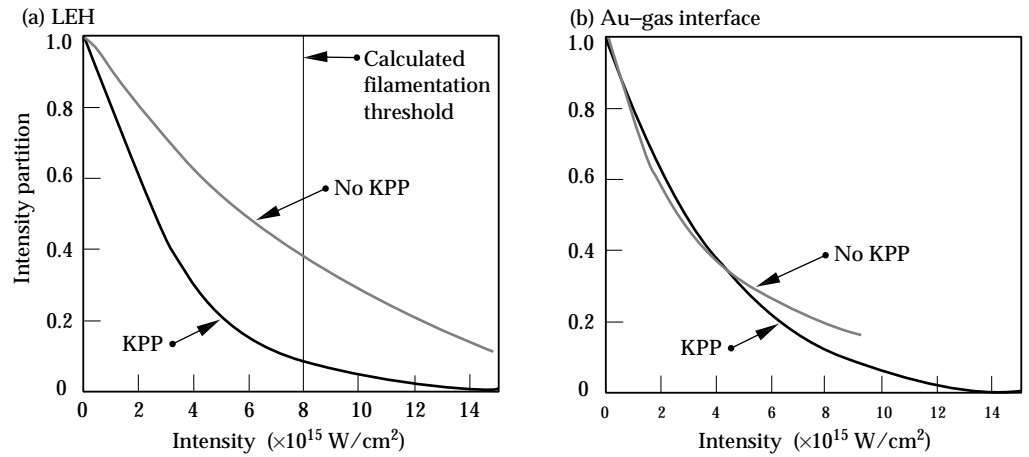


FIGURE 3. SRS spectra from gas-filled hohlraums at $1.8 \text{ ns} < t < 2 \text{ ns}$ for various smoothing conditions. With improved smoothing, the spectra narrow from 180 to 30 nm. (08-00-0598-1182pb01)

FIGURE 4. Intensity distribution in the laser beams (a) at the LEH and (b) at the Au-gas interface. At the LEH, more than 30% of an unsmoothed Nova beam exceeds the filamentation threshold. For a KPP-smoothed beam, only ~5% is above that threshold. This comparison is less favorable at the Au-gas interface. (08-00-0598-1183pb01)



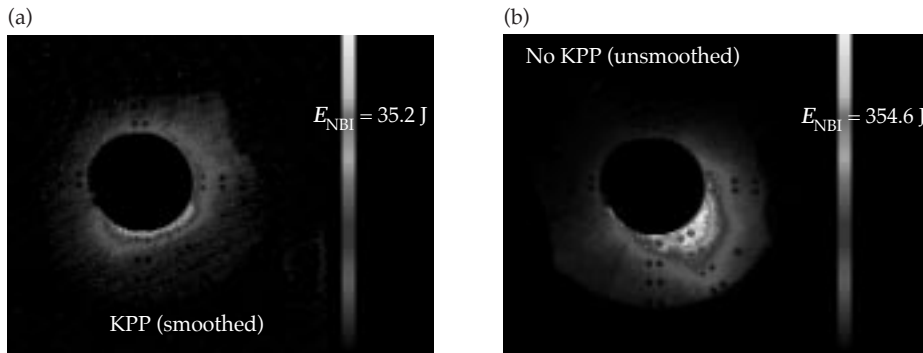
These experimental observations are consistent with calculations of the filamentation threshold.^{30–32} For our plasma conditions, they show that the laser beams filament for intensities of $I > 5$ to $8 \times 10^{15} \text{ W/cm}^2$. For unsmoothed laser beams, more than 30% of the laser beam exceeds this threshold in the LEH region, where Raman scattering occurs (see Figure 4a). On the other hand, a smoothed laser beam shows a significantly smaller fraction of high-intensity spots. Typically less than 5% of a Nova beam smoothed with a KPP is above the filamentation threshold; therefore, such beams are more stable against filamentation.

The favorable intensity distribution in the KPP-smoothed laser beams at the LEH explains the reduction of SRS losses by a factor of 6. Figure 4a shows the intensity distribution in the beam at the LEH, and Figure 4b shows the intensity distribution at the Au-gas interface. Absorption of the laser beam is neglected in these calculations. The intensity distribution in the beam at the LEH is more favorable than at the Au-gas interface, where calculations show the highest gain for SRS. Therefore, we expect a smaller reduction of SRS losses when applying beam smoothing. This picture is

consistent with a reduction of the SRS losses by only a factor of 2 when applying KPP smoothing as observed in the experiment (Figure 2b).

F3D simulations of filamentation and SRS in flowing Au plasma have shown that the SRS with random phase plate (RPP) or KPP illumination is reduced modestly when SSD is added. The simulations are about 50 ps long and use plasma parameters deduced from LASNEX and an average laser intensity of $3 \times 10^{15} \text{ W/cm}^2$. The simulation assumes that the interaction occurs near the focal plane of an $f/4$ optic such that the hot-spot structure has the characteristic size of $f/4$ speckles and a speckle intensity distribution $P(I) = [\exp(I/I_0)]/(I_0)$. The length of the Au region, $210 \mu\text{m}$, is similar to the LASNEX simulations (with an axial flow gradient that limits the gain of SRS), but the transverse size of the simulation region is much smaller than the laser beam spot size. The reduction is similar to that observed in the experiments and is associated with the control of hot-spot self-focusing.

The suppression of filamentation in the low-Z plasma for smoothed beams is also consistent with the spatially resolved measurements of the SRS signal.



	No KPP	KPP
% in lens	40	85
angle	8°	2°

FIGURE 5. Spatial dependence of the Brillouin backscattered light from gas-filled hohlraums. Data is shown (a) for a KPP-smoothed beam and (b) for an unsmoothed beam. SRS from a KPP-smoothed beam is directed almost straight back into the lens, whereas the centroid of an unsmoothed beam is shifted 8° downward. (08-00-0598-1185pb01)

Figure 5 shows the backscattered SBS light observed with the NBI detector. For smoothed laser beams (Figure 5a) the Brillouin signal is scattered back almost straight into the lens (which is represented by the black, circular surface in the center of the image). Only a small spatial shift of the backscattered light of $2^\circ \pm 1^\circ$ can be seen. On the other hand, unsmoothed laser beams show a backscattered Brillouin signal that is spatially shifted by up to $8^\circ \pm 1^\circ$ away from the straight-backward direction (Figure 5b).

These observations can be interpreted in the following way. As laser beams traverse the low-density plasma on their way to the hohlraum wall, they filament in the low-Z plasma in the LEH region and are deflected towards the LEH. SBS occurs when the beam reaches the high-Z Au plasma of the hohlraum wall and is scattered back, but will not retrace the incoming path, resulting in a spatial shift of the SBS signal as observed with the NBI detector. This interpretation is consistent with so-called spot motion experiments^{18,33} and with calculations³⁴ for unsmoothed laser beams. The experiments described by Delamater et al.¹⁸ and Kauffman et al.³³ show a deflection of laser beams toward the LEHs, which was greatly reduced when beam-smoothing techniques were applied. The calculations by Hinkel et al.³⁴ show a deflection of unsmoothed laser beams by about 6° for parameters similar to those in this study. Those results are in reasonable agreement with the observation in Figure 5.

For unsmoothed beams, our measurements with the FABS and the NBI show that 40% of the SBS light is scattered straight back into the lens, and 60% is scattered at larger angles. The light is mostly scattered in the downward direction, which is consistent with a deflection of the incoming laser beam toward the LEH. For smoothed beams, on the other hand, more than 85% of the light is scattered straight back into the lens, indicating that beam deflection is effectively suppressed.

Figure 6a compares the measured and calculated hohlraum wall temperatures as a function of time for a PS22 experiment. The calculations use corrected pulse shapes; i.e., scattering losses due to SBS and SRS were subtracted to obtain the laser power absorbed in the hohlraum, as shown in Figure 6b. Some discrepancies between the measured and calculated temperatures can be seen during the low-intensity foot with $t > t_0 + 1$ ns, and at the end of the hohlraum heating for $t > t_0 + 2$ ns. In the first case, we typically observe that the LASNEX simulations underestimate the temperatures by 10 to 15 eV. We observe this discrepancy when using higher laser intensities during the foot of the pulse, as in the PS22 experiments. A model was developed¹² that accounts for this underestimation. The model postulates that energy is transported directly to the hohlraum wall, seen by the Dante detector, due to laser sidescattering or electron transport. The result is a larger wall temperature than

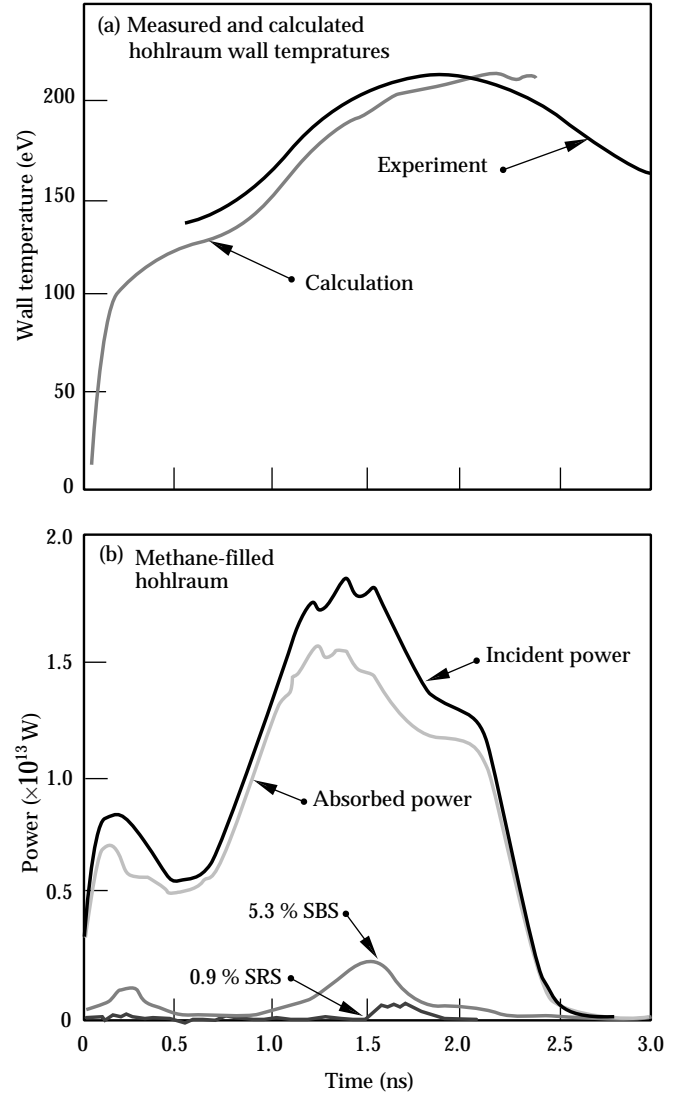


FIGURE 6. (a) Experimental hohlraum-wall temperature for a gas-filled hohlraum heated with PS22 (not albedo corrected) as a function of time from the Dante detector. (b) Laser power with scattering losses as function of time. (08-00-0598-1186pb01)

that calculated. This model has not yet been confirmed experimentally. However, in ignition experiments, radiation temperature in the foot can be readily adjusted to provide appropriate initial shocks for the implosion of the fusion capsule by reducing the laser power during the foot. The LASNEX calculations agree well with the peak temperature seen with Dante.

The LASNEX simulations of x-ray flux were post-processed to match the viewing angle of both detectors. In addition, calculations were performed to estimate the effect of the Be-lined Dante “washer” on the modeled temperatures. The liner can affect the hohlraum temperature both by absorbing radiation and by injecting low-Z material into the hohlraum. We cannot model the structure directly because it is a 3D

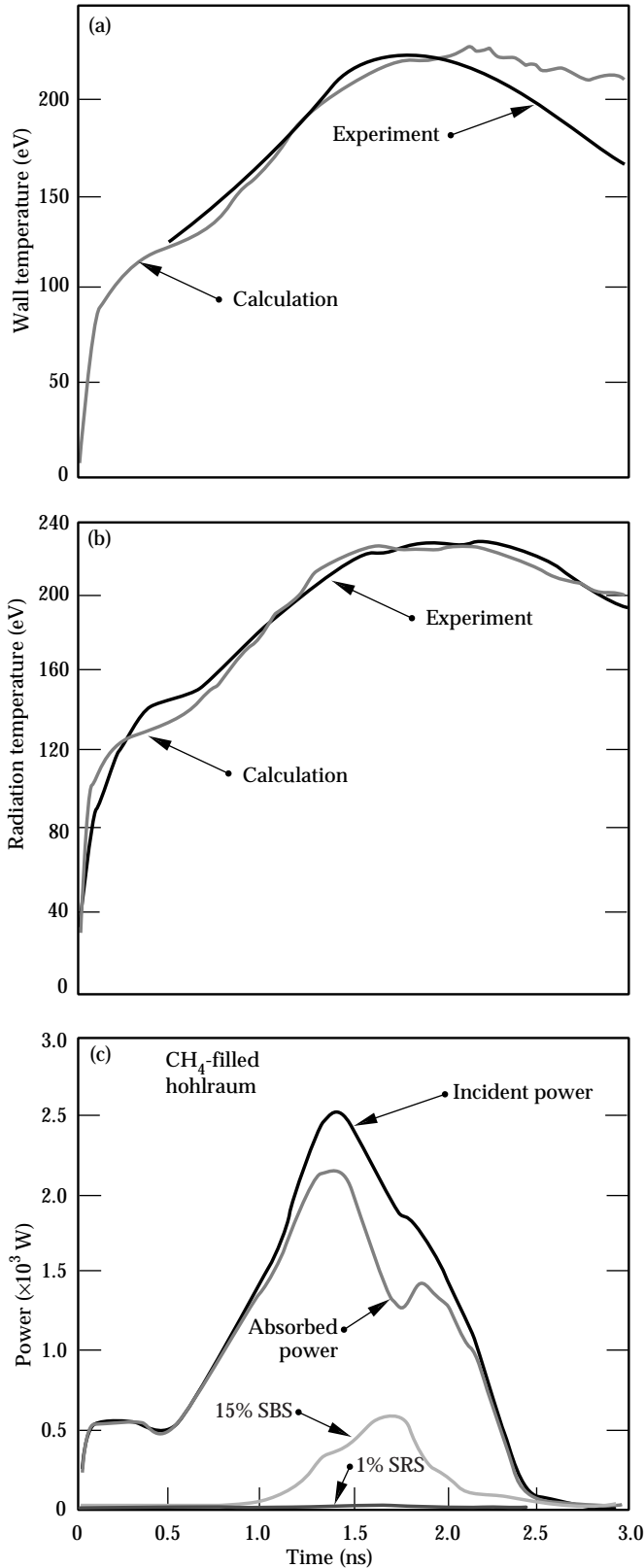


FIGURE 7. (a) Experimental hohlraum-wall temperature for a gas-filled hohlraum heated with PS26 (not albedo corrected) from the Dante detector, and (b) radiation temperature from the PCD. (c) Laser power with scattering losses as function of time. (08-00-0598-1189pb01)

feature on the side of the hohlraum. However, we can attempt to approximate its effect through simulations that include a Be sphere in the center of the numerical hohlraum that has the same area as the Be washer. During the period of peak drive, these simulations result in a temperature that averages approximately 3 eV cooler (not shown) than simulations without the Be sphere.

Figure 7a shows the measured hohlraum-wall temperature as a function of time for an experiment with PS26. The measurements of radiation temperature compare well to the results for detailed radiation hydrodynamic modeling. In particular, at the peak of the x-ray drive at $t > t_0 + 1.8$ ns, the measured and calculated temperatures match well. Once again, the calculations use corrected pulse shapes with SRS and SRS losses subtracted (see Figure c). To estimate the hohlraum radiation temperature T_{rad} for the purpose of simulating capsule implosion dynamics, we must include the fact that the capsule is irradiated by x rays from both the indirectly and directly heated hohlraum wall. To infer T_{rad} , we use the time-dependent albedo $\alpha(t)$, which is the ratio of the re-emitted flux over the incident flux,

$$\sigma[T_{\text{wall}}(t)]^4 = \alpha(t) \sigma[T_{\text{rad}}(t)]^4. \quad (2)$$

For our conditions, we calculate with LASNEX a maximum albedo of $\alpha \approx 0.8$, resulting in a correction of 11 eV at the peak of the x-ray drive. Figure 7b, which shows the hohlraum radiation temperature as a function of time from the PCD, indicates the validity of this approach.

For both types of experiments, we find smaller temperatures for $t > t_0 + 2$ ns than the values calculated with LASNEX. It is plausible that the effects of diagnostic hole closure start to become important at that time because the laser power is decreasing, and calculations show that cold blowoff plasma from the walls starts to move into the line of sight of the detector. More recently, we began working on a detailed experimental verification of the calculated, averaged charge number Z of the gold plasma. The charge number is an important parameter in calculations of radiation production. Testing the calculations might help us to understand the observed discrepancy at late times in that a possible overestimation of Z at late times will result in an overestimation of the radiation temperature as well.

When comparing the scattering losses for both types of experiments at different laser power (Figures 6b and 7c), we find that SRS losses increase significantly when increasing the laser power from PS22 to PS26. On the other hand, the losses by SRS are constant at approximately 1% of the incident laser energy. The SRS result

can be explained because the optical measurements for PS26 show narrow SRS spectra and no obvious beam deflection, very similar to the PS22 experiments described above. Figure 8 compares scattering losses observed with PS22 and PS26 for the various experiments. The increase of SBS losses with increasing laser power is not yet understood. The increase could be due to larger gain for the higher intensities encountered with PS26, or to the (spatial) laser amplitude modulations at the high fluences. Calculations are presently being performed to resolve this issue. Although most of the losses for PS26 occur after the maximum laser intensity, so that peak radiation temperatures are not affected, apparently SSD must be applied to reduce the scattering losses to acceptable small levels (5 to 10%).

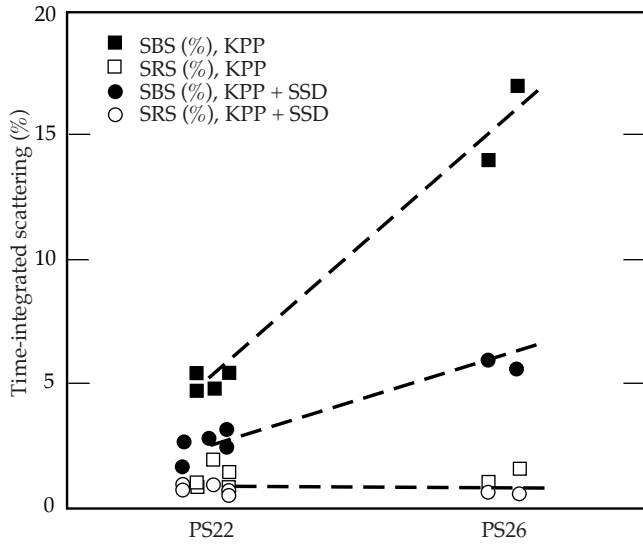


FIGURE 8. Comparison of total SBS and SRS losses for PS22 and PS26 in gas-filled hohlraums. The increase of the losses for PS26 could be related to higher gains or to laser amplitude modulations. (08-00-0598-1193pb01)

Figure 9 is a summary of the experimental hohlraum radiation temperatures obtained with varying (absorbed) laser power. The peak temperatures agree, within a standard deviation of 4 eV, with LASNEX modeling. The experimental peak radiation temperatures (after albedo correction) are plotted as a function of the laser power integrated over the high-intensity part of the laser drive $0.8 \text{ ns} < t < 1.8 \text{ ns}$ (see Figures 6b and 7c). For gas-filled hohlraums, we achieve peak radiation temperatures of 215 eV for PS22, and 232 eV for PS26. The data is compared to detailed LASNEX calculations and to the results of the Marshak scaling for ablative heat waves^{3,4}

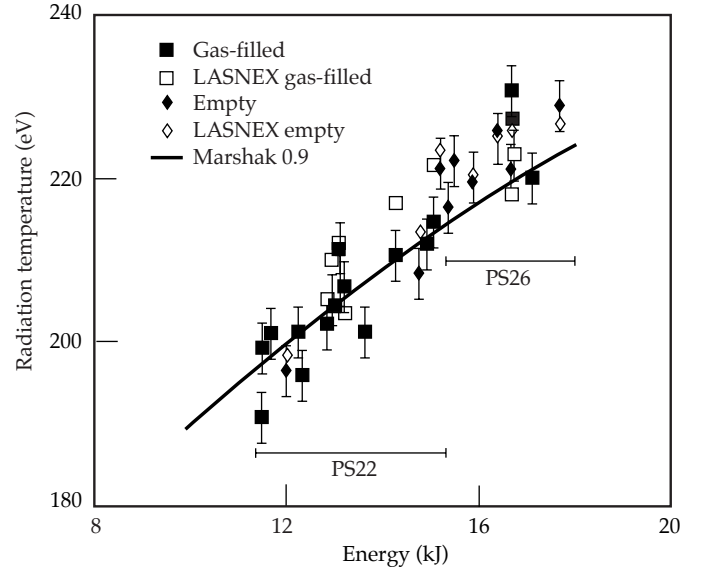


FIGURE 9. Experimental peak radiation temperatures of gas-filled and empty hohlraums for experiments with varying absorbed laser power during the high-intensity part of the pulse. The error of the individual data points is estimated to be 4 eV. Detailed LASNEX calculations agree with the experiments to within a standard deviation of 4 eV. Both the experiments and the calculations follow the scaling from Reference 13. (08-00-0598-1194pb01)

$$\eta P = AS_a + (A_{\text{hole}} + A_{\text{cap}})S_r. \quad (3)$$

This relation equates the power of the laser beams P with the absorbed flux S_a in the hohlraum wall of area A and the reradiated flux S_r through holes (area A_{hole}) or on the capsule (area A_{cap}). For Figure 4, we used constants from Reference 13 and a laser conversion of $\eta = 0.90$. The laser pulse was integrated only over the high-power part (0.8 to 1.8 ns), therefore neglecting the contribution of the low-power foot to the radiation temperature. This simplified model compares well to a more detailed scaling developed in Reference 35, which includes the foot contribution and results in $\eta = 0.85$. These values are in reasonable agreement with LASNEX simulations, which result in $\eta = 0.8$ to 0.9 (Ref. 12). The radiation temperatures of both the gas-filled and empty hohlraums compare well with each other and follow the scaling.

Conclusions

We have demonstrated effective coupling of laser power in gas-filled inertial confinement fusion hohlraums by controlling and reducing laser scattering losses with laser beam smoothing techniques. This is an important result for present target designs of future ignition experiments, e.g., at the NIF. For the large-scale-length hohlraums of the NIF, calculations show that a symmetric high-yield capsule implosion

can be achieved when filling the hohlraum with a low-Z gas to reduce the inward motion of the Au blowoff plasma from the hohlraum walls. We expect laser backscattering losses, which are caused by the addition of the gas, to be reduced when using laser beam smoothing with KPPs and by spectral dispersion. These techniques were included in the NIF design. Future experiments at Nova will test the specific SSD design that will be used in the NIF. It will also be important to extend the laser backscattering measurements of this study by using an $f/8$ focusing lens, which will be used at the NIF, and by testing other laser beam smoothing techniques, such as polarization smoothing, that might further reduce backscattering losses. In addition to new experiments, we are working on a more detailed comparison of the trends observed in the scattering measurements with calculations using the laser-plasma interaction code F3D.

The beneficial effects of the laser beam smoothing techniques were clearly seen in the radiation-temperature measurements of this study. We showed that radiation temperatures of both gas-filled and empty scale-1 hohlraums increase with KPP and KPP plus SSD and exceed 230 eV. They are reasonably well described by radiation hydrodynamic (LASNEX) modeling and scalings. The peak temperatures agree with the modeling, with a standard deviation of 4 eV, thus increasing our confidence in calculations for future inertial confinement fusion experiments.

Acknowledgments

We thank R. W. Lee for helpful criticism. The support of the crew of the Nova laser facility and of M. Rushford is greatly appreciated.

References

1. J. H. Nuckolls, *Phys. Today* **35** (9), 24 (1982).
2. J. D. Lindl, *Phys. Plasmas* **2**, 3933 (1995).
3. R. E. Marshak, *Phys. Fluids* **1**, 24 (1958).
4. R. Sigel et al., *Phys. Rev. Lett.* **65**, 587 (1990).
5. H. Nishimura et al., *Phys. Rev. A* **44**, 8323 (1991).
6. R. L. Kauffman et al., *Phys. Rev. Lett.* **73**, 2320 (1994).
7. S. W. Haan et al., *Phys. Plasmas* **2**, 2480 (1995).
8. W. J. Krauser, *Phys. Plasmas* **3**, 2084 (1996).
9. W. L. Kruer, *The Physics of Laser Plasma Interactions* (Addison-Wesley, New York, 1988).
10. T. P. Hughes, *Plasmas and Laser Light* (John Wiley and Sons, New York, 1975).
11. G. B. Zimmerman and W. L. Kruer, *Comments Plasma Phys. Controlled Fusion* **2**, 85 (1975).
12. L. J. Suter et al., *Phys. Rev. Lett.* **73**, 2328 (1994); L. J. Suter et al., *Phys. Plasmas* **3**, 2057 (1996).
13. R. Sigel et al., *Phys. Rev. A* **38**, 5779 (1988).
14. E. M. Campbell et al., *Rev. Sci. Instrum.* **57**, 2101 (1986).
15. B. A. Hammel et al., *Phys. Rev. Lett.* **70**, 1263 (1993).
16. M. D. Cable et al., *Phys. Rev. Lett.* **73**, 2316 (1994).
17. A. A. Hauer et al., *Phys. Plasmas* **2**, 2488 (1995).
18. N. D. Delamater et al., *Phys. Plasmas* **3**, 2022 (1996).
19. S. H. Glenzer et al., *Phys. Rev. Lett.* **79**, 1277 (1997).
20. S. N. Dixit et al., *Optics Lett.* **21**, 1715 (1996).
21. Y. Kato et al., *Phys. Rev. Lett.* **53**, 1057 (1985); D. M. Pennington et al., *Proc. SPIE* **1870**, 175 (1993).
22. R. H. Lehmberg and S. P. Obenschein, *Opt. Commun.* **46**, 27 (1983); S. Skupsky et al., *J. Appl. Phys.* **66**, 3456 (1989).
23. H. Kornblum et al., *Rev. Sci. Instrum.* **57**, 2179 (1986).
24. D. R. Kania et al., *Rev. Sci. Instrum.* **61**, 2765 (1990); L. S. Pan et al., *Appl. Phys. Lett.* **57**, 623 (1990).
25. C. Decker et al., *Phys. Rev. Lett.* **79**, 1491 (1997).
26. B. J. MacGowan et al., *Phys. Plasmas* **3**, 2029, (1996).
27. R. K. Kirkwood et al., *Rev. Sci. Instrum.* **68**, 636 (1997).
28. H. S. Rose, *Phys. Plasmas* **3**, 1709 (1996).
29. J. D. Moody et al., *Phys. Rev. Lett.* **77**, 1294 (1996).
30. E. M. Epperlein and R. Short, *Phys. Fluids B* **4**, 2211 (1992).
31. R. L. Berger et al., *Phys. Fluids B* **5**, 2243 (1993).
32. V. Yu. Bychenkov et al., *Phys. Rev. E* **52**, 6759, (1995).
33. R. L. Kauffman et al., *Phys. Plasmas* **5**, 1927 (1998).
34. D. S. Hinkel et al., *Phys. Rev. Lett.* **77**, 1298 (1996).
35. E. Dattolo, H. Dumont, Y. Saillard, and J.-P. Jadaud, private communication (1995).

OPTIMIZATION OF BEAM ANGLES FOR THE NATIONAL IGNITION FACILITY

S. M. Pollaine

S. W. Haan

Introduction

The National Ignition Facility (NIF), now being built at Lawrence Livermore National Laboratory, is a 1.8-MJ Nd-glass laser with 192 beamlets. The beamlets are grouped into 48 quads of 4 beamlets each. The spherical target chamber has 72 ports arranged in ten rings at latitudes 23.5°, 30°, 44.5°, 50°, 77.5°, 102.5°, 130°, 135.5°, 150° and 156.5°, with 4, 4, 8, 8, 12, 12, 8, 8, 4, and 4 ports, respectively, per ring evenly spaced azimuthally within each ring. The locations of the NIF ports have been chosen to optimize flexibility and performance so that three different drive options are possible—direct drive and two types of indirect drive. This article describes the rationale for choosing the final NIF beam angles to maximize flexibility regarding the three different drive options.

Inertial confinement fusion (ICF) has two main approaches: indirect drive¹ and direct drive.² In both cases, a thin, spherical, hollow shell (capsule) containing deuterium–tritium (DT) fuel is subjected to intense radiation, causing the shell to implode. The implosion compresses the fuel and brings it to a density and temperature at which a runaway nuclear fusion reaction occurs. In direct drive, a laser is used to directly irradiate the capsule. In indirect drive, the laser is directed into a hohlraum containing the capsule, generating secondary x rays that irradiate the capsule. In both approaches, the outer layers of the irradiated capsule are ablated, causing high pressures that compress the DT fuel, and raising the density and temperature to the point at which a nuclear fusion reaction occurs.

For significant burn to occur, it is important that the shell remain spherical up to the point of ignition, requiring, in turn, a very uniform radiation flux on the shell. The capsule must be compressed by a factor of 30 to 40 (Ref. 3), which requires a drive asymmetry of less than roughly 1%.

Drive asymmetry can be expressed as a sum of spherical harmonics:

$$f(\theta, \varphi) = \sum_{l,m} a_{lm} Y_{lm}(\theta, \varphi) , \quad (1a)$$

where $Y_{lm}(\theta, \varphi)$ are the spherical harmonics,

$$\iint Y_{lm}(\theta, \varphi) Y_{l'm'}(\theta, \varphi) \sin(\theta) d\theta d\varphi = \delta_{ll'} \delta_{mm'} , \quad (1b)$$

l ranges from zero to infinity, and m ranges from $-l$ to $+l$. If the flux asymmetry is azimuthally symmetric, then $a_{lm} = 0$ for $m \neq 0$, and it becomes convenient to expand the asymmetry as a sum of Legendre polynomials:

$$f(\theta, \varphi) = \sum_l a_l P_l(\cos \theta) , \quad (2a)$$

where

$$\int_{-1}^1 P_m(x) P_n(x) dx = \frac{\delta_{mn}}{n + 1/2} . \quad (2b)$$

The NIF will allow for two indirect-drive options: cylindrical indirect drive and tetrahedral indirect drive. In cylindrical indirect-drive geometry, the hohlraum has the shape of a cylinder, with the laser entrance holes (LEHs) at the ends of the cylinder, and the laser beams are arranged in rings on the hohlraum wall. In the NIF, 48 quads of 4 beamlets each will be

pointed to illuminate the hohlraum wall in two rings per side, an inner ring on the waist plane at 90° and an outer ring at about 50° from the hohlraum axis, as shown in Figure 1. Because of the approximate azimuthal symmetry and left/right symmetry, the capsule flux asymmetry has components consisting primarily of the even Legendre polynomials. As the hohlraum walls move inward, the location of the rings on the walls changes. The second Legendre polynomial P_2 of the capsule flux asymmetry can be eliminated in a time-varying way by varying the relative power between the inner and outer rings. The fourth moment P_4 can be averaged to zero by choosing a suitable hohlraum length. Higher moments are small because of the smoothing effect of x-ray transport between the walls and the capsule.⁴

Tetrahedral indirect drive, which uses a hohlraum that is spherical instead of cylindrical, is a new form of indirect drive.^{5,6} Instead of two LEHs, four LEHs are arranged in a tetrahedral configuration. Figure 2 shows a tetrahedral hohlraum with some of its beams. This configuration leads to greater radiation losses, but there are some symmetry advantages. Instead of distinct rings on the hohlraum wall, the beams are scattered all over the hohlraum wall. In all formulations considered to date, an identical pattern of beams goes through each of the four holes, and it is this requirement that has impacted the selection of the NIF beam angles.

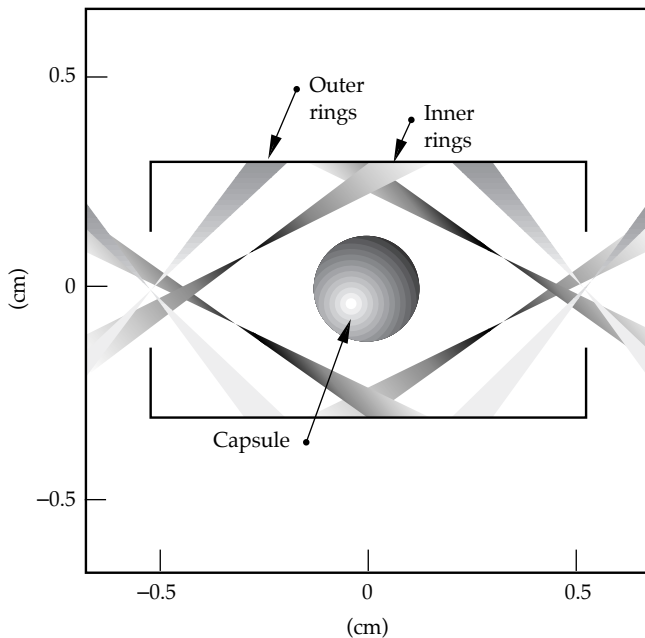


FIGURE 1. Cylindrical hohlraum, showing the inner and outer rings of beams and the capsule at the center. (50-04-0197-0162pb01)

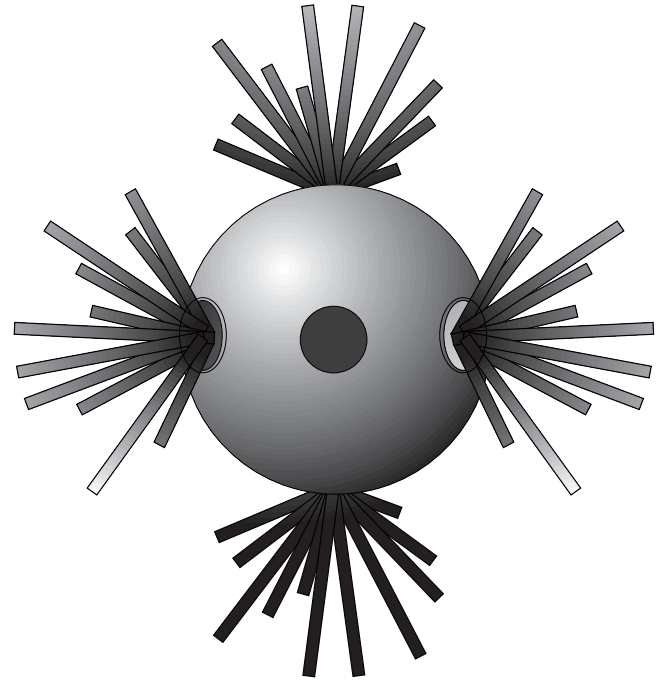


FIGURE 2. A tetrahedral hohlraum with eleven beams going through each laser entrance hole. (The hohlraum shown would be about 8 mm in diameter.) (50-04-0197-0163pb01)

Requirements of Cylindrical Indirect Drive

As shown in Figure 1, cylindrical hohlraums on the NIF will be illuminated by a ring of beams on the waist plane at 90° , called the inner rings, and by a ring of beams on each side at about 50° , called the outer rings. The flux asymmetry at the capsule will be mostly P_2 and P_4 . The positive P_2 contribution from the outer rings must balance the negative P_2 contribution from the inner rings and the lack of radiation from the LEHs. As the albedo of the hohlraum wall increases, the importance of the lack of radiation from the LEHs increases, which makes P_2 more negative. As time advances, the walls move in, causing the emission of radiation to move out towards the LEHs, which makes P_2 more positive. Thus, the relative power balance between the inner and outer beams must be changed to keep $P_2 = 0$.

The first NIF target designs put the inner and outer beams on two lines of latitude per side on the target chamber at about 33° and 61° . In 1991, these angles were reduced to 26° and 54° . Later, we found it desirable to decrease the maximum angle to 50° to increase

clearance through the LEH. As the design of the laser progressed, it was found that there was insufficient room on the target chamber for eight ports in each line of latitude. Thus, the eight ports at 26° were split into two rings of four ports each at 23.5° and 30° , and the eight ports at 50° were split into two rings of four ports each at 46.5° and 50° , with the azimuthal angles of each of the two subrings interleaved and evenly spaced. These angles were selected because they provided the minimum separation necessary for the ports to fit on the target chamber. We have now switched ring 3 from 46.5° to 44.5° to accommodate direct drive and to increase flexibility. Ring 3 can be moved outwards to form a two-ring configuration, or it can be moved inwards to form a three-ring configuration, as shown in Figure 3.

As shown in Table 1, we examined four sets of ring angles in detail. For the sets with ring 3 at 46° , ring 3 was moved in by $300\text{ }\mu\text{m}$ to form a 3-ring configuration, or it was moved out by $341\text{ }\mu\text{m}$ to form a 2-ring configuration. For each of these sets of ring angles, we moved ring 3 and ring 4 in or out together as a unit to assess the robustness of our hohlraum designs.

Figure 4 shows how the calculated yield, expressed in MJ, varied as a function of the outer beam offset. Each 2D calculation was integrated, in the sense that each included laser beam transport, beam deposition and x-ray production, transport of x rays from the hohlraum wall to the capsule, capsule implosion, and thermonuclear burn. The yield of the first set of ring angles, with ring-3 angle at 41.6° , decreases sharply as the

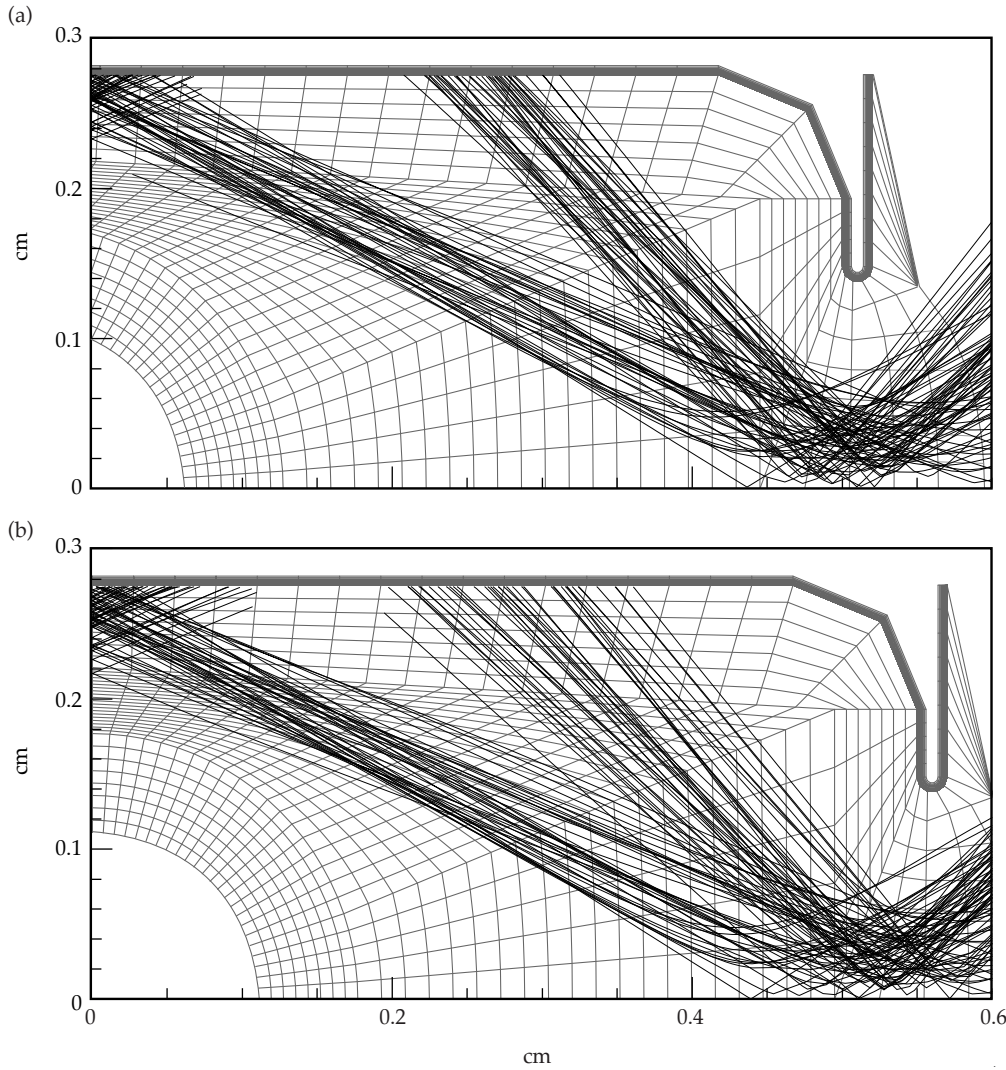


FIGURE 3. Moving ring 3 in or out can give a 2-ring-per-side configuration, or a 3-ring-per-side configuration. (50-00-0598-1164pb01)

TABLE 1. Four sets of ring angles studied, including ring-3 offsets.

Set number	Ring 1 angle (°)	Ring 2 angle (°)	Ring 3 angle (°)	Ring 4 angle (°)	Ring 3 offset (μm)
1	23.5	31.9	41.6	50	0
2	23.5	30	43	50	341
3	23.5	30	43	50	-300
4	23.5	30	46.5	50	0

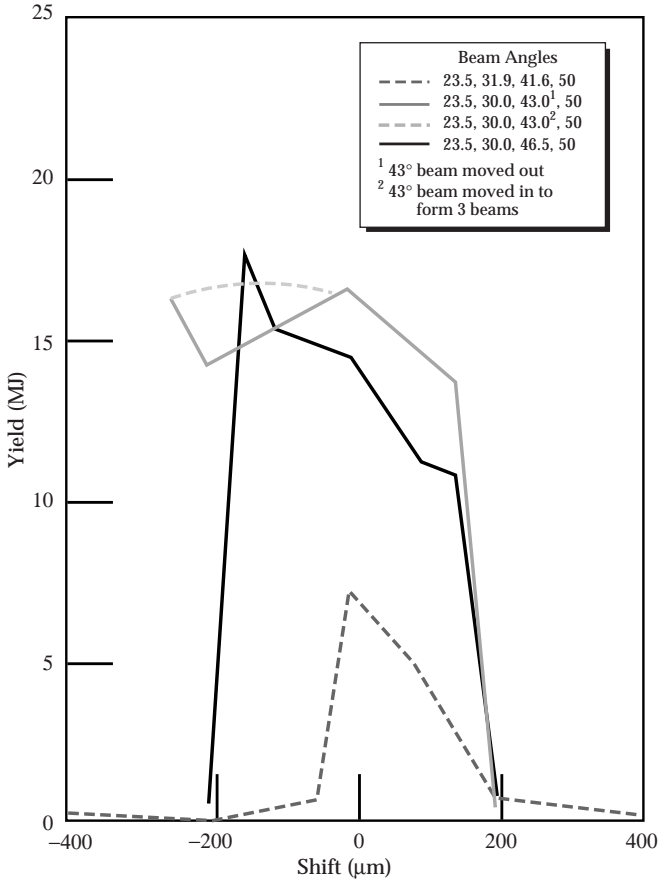


FIGURE 4. The yield vs shift in the outer ring for four different ring configurations. (50-00-0598-1165pb01)

beams are moved in because the beams hit the lip of the LEH. Undoubtedly, the proper offset would expand the range of usable yield. With this caveat, the robustness is relatively insensitive to the ring-3 angle. Because each laser beam is expected to have an rms pointing error of about 50 μm, any ring-3 angle between about 43° and 46.5° would have adequate robustness.

Two considerations drove our choice of the ring-3 angle. The first consideration was to maximize flexibility regarding different configurations. The smaller the ring-3 angle, the greater the distance those beams could

be moved in or out before they hit the LEH. This consideration favors a smaller ring-3 angle. The second consideration was to accommodate ring 5 for direct drive. To avoid a ring of diagnostics on the equator, the ring-5 angle must be smaller than about 78°. As explained in the following section, direct-drive considerations imply that the ring-3 angle must then be larger than about 44°. We chose a value of 44.5° as a compromise between the two considerations.

Requirements of Direct Drive

In direct drive, the laser directly illuminates the capsule. Thus, we require that the laser intensity be uniform to about 1%. We expand the capsule flux asymmetry in spherical harmonics as

$$f(\theta, \varphi) = \sum_{l,m} a_{lm} Y_{lm}(\theta, \varphi) . \quad (3)$$

We assume that all beams produce the same azimuthally symmetric, normalized flux intensity $b(\theta)$ on the capsule, with a Legendre decomposition

$$b_l = \int b(\theta) P_l[\cos(\theta)] d\cos(\theta) / \int b(\theta) d\cos(\theta) , \quad (4)$$

so that b_l is the reduction of mode l due to the beam pattern compared to a delta function. If w_i is the weight, or relative power, of the i th beam, it follows that⁷

$$a_{lm} = b_l \sum_k w_k Y_{lm}^*(\theta_k, \varphi_k) . \quad (5)$$

On the NIF, the direct-drive option has considered $b(\theta)$ in the form of $b(\theta) = \cos^p(\theta)$, with p between 1 and 3, for which

$$b_l = \frac{\Gamma(p+2)\Gamma(l-p-1)\sin[(l-p)\pi/2]}{2^{l-1}\Gamma[(l+p+3)/2]\Gamma(l-p-1)/2)} , \quad (6)$$

a function that decreases as $l^{-(p+3/2)}$. This smooths out the higher modes, so we must select the placement of beams to minimize the lowest modes. If each beam has equal power, which maximizes the available energy, then we require that

$$\sum_i Y_{lm}^*(\theta_i, \phi_i)$$

be as small as possible for the lowest few modes. Given the NIF design, the most important mode to eliminate is $Y_{2,0}$, which is proportional to

$$P_2(\theta) = \frac{3}{2} \cos^2(\theta) - \frac{1}{2} . \quad (7)$$

With direct drive using four ports at 23.5° , eight ports at θ_3 such that $43^\circ < \theta_3 < 46.5^\circ$, and 12 ports on a fifth ring with θ_5 between 75° and 80° , we require that

$$4P_2(23.5^\circ) + 8P_2(\theta_3) + 12P_2(\theta_5) = 0 . \quad (8)$$

If we chose the desired value of $\theta_3 = 43^\circ$, then $\theta_5 = 80.1^\circ$, and the ports came too close to the diagnostic ports on the equator at $\theta = 90^\circ$. Thus, we chose $\theta_3 = 44.5^\circ$, with the corresponding selection of $\theta_5 = 77.5^\circ$.

Requirements of Tetrahedral Indirect Drive

Tetrahedral indirect drive is a third option for ignition on the NIF. The hohlraum is spherical, with four LEHs arranged in a tetrahedral configuration. If exact tetrahedral symmetry were maintained, then the capsule flux asymmetry would have no components of modes $l = 1, 2$, or 5 , and only one component of $l = 3$ and $l = 4$. Exact tetrahedral symmetry inside the hohlraum requires that the beams come in sets of 12, with three beams going through each of the four LEHs, all at the same angle to the normal of the respective LEHs.⁵ To reduce costs, it was determined that the tetrahedral option would only use the ports already selected for cylindrical indirect drive and direct drive. This constraint precludes exact tetrahedral symmetry. We settled for a weaker symmetry in which each LEH has an identical configuration of beams going through it. Although this weaker symmetry brings in components of $l = 1, 2$, and 5 , and extra components of $l = 3$ and $l = 4$, the flux at the capsule is still more symmetric than it would be if this weaker symmetry were violated.

The weaker symmetry constrains the azimuthal rotation of each ring of ports. The four LEHs are arranged with two of the LEHs at $\theta = 54.7^\circ$ [$\arccos(\sqrt{1/3})$], $\phi = [0^\circ, 180^\circ]$, and two at $\theta = 125.3^\circ$, $\phi =$

$[90^\circ, 270^\circ]$. The two LEHs at 54.7° see a given ring of ports rotated 180° with respect to each other. Because the number of ports per ring is even, a rotation of 180° represents no change, so the two LEHs see an identical configuration of ports. The same argument holds for the two LEHs at 125.3° . To compare an LEH at 54.7° with an LEH at 125.3° , we transform $(\theta, \phi) \rightarrow (180^\circ - \theta, 90^\circ - \phi)$. Thus, for example, if ring 1 has a port at $\phi = 15^\circ$, ring 10 must have a port at 75° , and so on for each pair of supplementary rings.

Several other constraints exist for the azimuthal rotation of each ring of ports. These constraints can be expressed most easily in terms of clicks, defined as $\{\phi_i\} = (\{0, 1, 2, \dots, N\} + \text{click}) \times 360^\circ / N$, where N is the number of ports in a given ring, and click k satisfies $0 \leq k \leq 1$. The weak symmetry constraint described in the previous paragraph is equivalent to $k(i) + k(10 - i) = 1$, where $k(i)$ is the click of the i th ring.

We demand that the four ports of the first ring be evenly interwoven with the four ports of the second ring, so that $|k(1) - k(2)| = 1/2$. Similarly, $|k(3) - k(4)| = 1/2$. When combined with the first constraint, then we automatically also have $|k(7) - k(8)| = |k(9) - k(10)| = 1/2$.

To keep the laser from being damaged, we demand that if a beam should miss the target and reach the opposite side of the target chamber, it will not hit another port, where it would then reenter the amplifier chain. This constraint is optimized if $|k(1) - k(10)| = \{1/4 \text{ or } 3/4\}$, $|k(3) - k(8)| = \{1/4 \text{ or } 3/4\}$, and $|k(5) - k(6)| = 1/2$.

To reduce costs, as many ports on the ring at latitude 50° should lie on the same longitude as ports on the ring at latitude 77.5° . Then these aligned ports allow a beam to be switched between them with a fewer number of mirrors. This requirement is equivalent to $3k(4) - 2k(5) = \text{an integer}$. Once satisfied, the corresponding constraint, $3k(7) - 2k(6) = \text{an integer}$, is automatically satisfied as well. However, this constraint precludes $|k(5) - k(6)| = 1/2$. We relaxed this constraint to $|k(5) - k(6)| > 5/16$, which is adequate for the beams to miss the ports on the opposite side of the target chamber.

These five constraints have 16 possible solutions, as follows:

- $\{k(1), k(2)\} = \{1/8, 5/8\} \text{ or } \{3/8, 7/8\} \text{ or } \{5/8, 1/8\} \text{ or } \{7/8, 3/8\}$.
- $\{k(3), k(4), k(5)\} = \{3/8, 5/8, 5/16\} \text{ or } \{3/8, 5/8, 13/16\} \text{ or } \{5/8, 3/8, 3/16\} \text{ or } \{5/8, 3/8, 11/16\}$.
- $\{k(6), k(7), k(8), k(9), k(10)\} = 1 - \{k(5), k(4), k(3), k(2), k(1)\}$.

It has been difficult to choose among the 16 solutions on the basis of tetrahedral performance alone. The other options, cylindrical indirect drive and direct drive, are not affected by the clicks. By default, the laser designers have chosen the following set of clicks: $k = \{14, 6, 6, 14, 13, 3, 2, 10, 10, 2\} / 16$, with the corresponding azimuthal angles of $78.75^\circ, 33.75^\circ, 16.875^\circ, 39.375^\circ, 24.375^\circ, 5.625^\circ, 5.625^\circ, 28.125^\circ, 56.25^\circ, 11.25^\circ$.

Beam Switching

When switching from cylindrical indirect drive to direct drive, the 12 beams going through the ports on latitudes 30° and 50° must be switched to the ports on latitude 77.5° . In general, it is important to minimize the change in longitude when switching from one latitude to another. The tetrahedral indirect-drive option can use any combination of 48 ports out of 72, subject to the constraint that one does not pick two ports that are linked by a beam that switches from one port to another. Thus, the choice of which ports to link when switching from direct to indirect drive affects the tetrahedral option. The most important consideration is that the linkages be symmetric with respect to the four tetrahedral LEHs, so that four-hole symmetry can be maintained.

In selecting which of the 72 ports to use for the tetrahedral option, we require that each beam go through its corresponding LEH at an angle greater than 20° so that it does not hit the capsule at the center of the hohlraum, and at an angle less than 60° so that there is more clearance through the LEH and the beam does not skirt too close to the hohlraum wall as it passes through the hohlraum. We also require that the beams not land too close to an exit LEH; otherwise, the exit LEH may close prematurely. These constraints could not be simultaneously satisfied with all 48 beams. Therefore, only 44 beams, with 11 beams per LEH, will be used for the tetrahedral option. Figure 5 shows which ports will be used by the tetrahedral option and how the beams will be switched between ports. The preliminary NIF design had a switching arrangement that precluded the use of four of these 44 beams, but the final design now allows the use of all 44 beams.

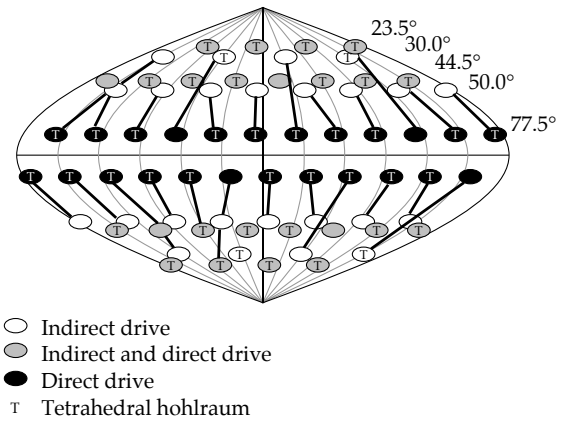


FIGURE 5. Map of beam ports, showing the linkages used in beam switching and which ports are used in the tetrahedral option. If two ports are linked, only one of them can be used for the tetrahedral option. (50-04-0197-0164pb02)

Final Beam Angles

When designing the laser, 24 beams had to be moved about half a degree so there would be room for the beam-lines and mirror mounts. These beams are identified in Table 2, which shows the coordinates for the 72 NIF ports. The table also shows which ports are used by each option, and how the ports are switched from direct to indirect drive. For the tetrahedral option, it shows which of the four LEHs the beam goes through. Each beam port will be located within $1/4$ inch (0.05°) of the designated location.

TABLE 2. Final beam angles (continued next page).

Port Number	Polar angle θ ($^{\circ}$)	Azimuthal angle ϕ ($^{\circ}$)	Moved	Direct (D), Indirect (I), or Tetrahedral (T)	Port switching
1	23.5	78.75	No	D I T1	–
2	23.5	168.75	No	D I T2	–
3	23.5	258.75	No	D I T2	–
4	23.5	348.75	No	D I T1	–
5	30.58	34.33	Yes	I	25
6	30	123.75	No	I T2	28
7	30.58	214.33	Yes	I	31
8	30	303.75	No	I T1	34
9	44.5	16.29	Yes	D I	–
10	44.5	62.46	Yes	D I T1	–
11	44.5	106.29	Yes	D I T2	–
12	44.5	152.46	Yes	D I T2	–
13	44.5	196.29	Yes	D I	–
14	44.5	242.46	Yes	D I T2	–
15	44.5	286.29	Yes	D I T1	–
16	44.5	332.46	Yes	D I T1	–
17	50	39.67	Yes	I	26
18	50	84.38	No	I	27
19	50	129.38	No	I	29
20	50	174.38	No	I	30
21	50	219.67	Yes	I	32
22	50	264.38	No	I	33
23	50	309.38	No	I	35
24	50	354.38	No	I	36
25	77.5	24.38	No	D T1	5
26	77.5	54.38	No	D T1	17
27	77.5	84.38	No	D T3	18
28	77.5	114.38	No	D	6
29	77.5	144.38	No	D T2	19
30	77.5	174.38	No	D T2	20
31	77.5	204.38	No	D T2	7
32	77.5	234.38	No	D T2	21
33	77.5	264.38	No	D T4	22
34	77.5	294.38	No	D	8
35	77.5	324.38	No	D T1	23
36	77.5	354.38	No	D T1	24
37	102.5	5.62	No	D T1	49
38	102.5	35.62	No	D T3	50
39	102.5	65.62	No	D T3	65
40	102.5	95.62	No	D T3	51
41	102.5	125.62	No	D T3	52
42	102.5	155.62	No	D	66
43	102.5	185.62	No	D T2	53
44	102.5	215.62	No	D T4	54
45	102.5	245.62	No	D T4	67
46	102.5	275.62	No	D T4	55
47	102.5	305.62	No	D T4	56
48	102.5	335.62	No	D	68
49	130	5.62	No	I	37
50	130	50.62	No	I	38
51	130	95.62	No	I	40

TABLE 2. Final beam angles (continued).

Port Number	Polar angle θ ($^{\circ}$)	Azimuthal angle ϕ ($^{\circ}$)	Moved	Direct (D), Indirect (I), or Tetrahedral (T)	Port switching
52	130	140.33	Yes	I	41
53	130	185.62	No	I	43
54	130	230.62	No	I	44
55	130	275.62	No	I	46
56	130	320.33	Yes	I	47
57	135.5	27.54	Yes	D I T3	–
58	135.5	73.71	Yes	D I	–
59	135.5	117.54	Yes	D I T3	–
60	135.5	163.71	Yes	D I T3	–
61	135.5	207.54	Yes	D I T4	–
62	135.5	253.71	Yes	D I	–
63	135.5	297.54	Yes	D I T4	–
64	135.5	343.71	Yes	D I T4	–
65	150	56.25	No	I	39
66	149.418	145.67	Yes	I T3	42
67	150	236.25	No	I	45
68	149.418	325.67	Yes	I T4	48
69	156.5	11.25	No	D I T3	–
70	156.5	101.25	No	D I T3	–
71	156.5	191.25	No	D I T3	–
72	156.5	281.25	No	D I T4	–

Conclusion

The NIF laser now being built will have 48 beams passing through 72 ports on the target chamber. The locations of the ports have been chosen to optimize the flexibility and performance of the cylindrical indirect-drive option, while allowing direct-drive and tetrahedral indirect-drive experiments to be performed.

Notes and References

1. J. D. Lindl, *Phys. Plasmas* **2**, 3933–4024 (1995).
2. C. Verdon, *Bull. Am. Phys. Soc.* **38**, 2010 (1993).
3. J. D. Lindl, *Phys. Plasmas* **2**, p. 3934 (1995).
4. S. W. Haan, *Radiation Transport Between Concentric Spheres*, Lawrence Livermore National Laboratory, Livermore, CA, UCRL-ID-118152 (1994); D. Kershaw, private communication.
5. D. W. Phillion and S. M. Pollaine, *Phys. Plasmas* **1**, 2963–2975 (1994).
6. J. D. Schnittman and R. S. Craxton, *Phys. Plasmas* **3**(10), 1–12 (1996).
7. S. M. Pollaine and D. Eimerl, “Modal Analysis of Directly Driven ICF Targets,” accepted by *Nuclear Fusion*.

HIGH-ENERGY X-RAY MICROSCOPY AT THE NATIONAL IGNITION FACILITY

J. A. Koch

*C. Brown**

S. G. Glendinning

D. H. Kalantar

T. W. Barbee, Jr.

P. Celliers

B. A. Hammel

O. L. Landen

G. R. Bennett[†]

L. B. Da Silva

W. Hsing[†]

*J. Seely**

Introduction

X-ray microscopy has made numerous critical contributions to the current state of knowledge in inertial confinement fusion (ICF) research¹ and in other areas of laser-produced plasma research, and we expect it to continue to be vital for experiments at the National Ignition Facility (NIF). Examples of experiments relying on high-energy, high-resolution microscopy include backlit shock radiography for diagnosis of time-dependent radiation symmetry in hohlraums,² emission imaging of doped ICF capsules for diagnosis of temperature and density uniformity in the compressed core,³ and shock trajectory measurements for equation-of-state studies.^{4,5}

Detector-mounted pinholes and slits are typically used in experiments at Nova and at other facilities. However, the extreme environment at NIF implies that there will be an exclusion zone with a radius of ~200 mm, inside of which pinholes and associated shielding mounted to the detector may not survive high-energy experiments. This distance is farther than desired for pinhole imaging due to diffractive degradation of spatial resolution and to decreased collection solid angles for a fixed magnification.

In anticipation of experiments at NIF, we have begun a systematic investigation of various options for x-ray imaging at energies of ~4–13 keV. X-ray sources in this spectral region are generally line emitters, and this implies that high efficiency is needed only over a relatively narrow spectral region containing the emission line of interest. However, various emission lines at different energies are of interest, and this implies that quasi-monochromatic x-ray imaging instruments should have flexibility in operating energy. In addition, minimization of neutron and

high-energy x-ray backgrounds implies that the x-ray detector should ideally be shielded from a direct line of sight to the target, and also implies that at least a moderate spectral selectivity is desirable. The experiments envisaged here have different requirements, but typically include 0.5- to 2-mm fields of view in one or two dimensions, suitability for multiple-frame imaging onto a gated camera for 2D applications, 2- to 10- μ m spatial resolution at the source, magnifications of 4–40 \times , and high efficiency for both emission and absorption geometries.

The options being considered fall into two categories. The first category is short-working-distance, expendable imaging elements, and includes primarily pinholes and their 1D analog, slits. Pinholes have proven to be versatile and simple to use; however, to operate at NIF with useful collection angle and spatial resolution, the pinhole must be mounted well within the exclusion zone, with the result that the pinhole and associated support structure will likely be destroyed during the experiment. One solution is to mount the pinhole on the target rather than on the detector; however, this will add an extra source of exploding debris to the target that could also damage detectors and could damage laser optics. In addition, premature pinhole closure during the experiment is a concern.⁶ Possible options include tamping the pinhole with plastic to mitigate closure during the experiment, and placing a plastic wedge on the target side of the pinhole in order to control its trajectory. Reduced image contrast due to a high-energy x-ray background transmitted through the substrate may also be an issue for some experiments.

The second category is long-working-distance, reusable diagnostics that are designed to survive high-energy experiments, and this category includes primarily reflective-optic imaging systems. Types of imaging systems being considered include metal-mirror Kirkpatrick-Baez (KB) microscopes,⁷ multilayer mirror

*Naval Research Laboratory, Washington, DC

[†]Los Alamos National Laboratory, Los Alamos, NM

KB microscopes,⁸ bent-crystal KB microscopes, single spherical⁹ or toroidal¹⁰ crystal microscopes, and dual spherical-crystal microscopes.¹¹ More complex compound grazing-incidence systems could also be considered, such as Wölter's and similar variations,^{12,13} but in any case versatility, simplicity of alignment, and cost are vital practical considerations.

Our current strategy is to investigate short-working-distance, target-mounted pinholes in Nova experiments while simultaneously investigating reflective optic imaging systems for long-term implementation at NIF. The variety of design options is large, and we begin by systematically investigating the advantages and disadvantages of the simplest reflective optic systems and comparing them to pinholes and slits. We note that the image exposure (e.g., in W/cm^2) obtained on a detector by an imaging system can be written generally as $(\Omega\eta/M_v M_h)I_0$, where I_0 is the spectrally integrated source brightness (e.g., in $W/cm^2 \cdot Sr$), M_v and M_h are the vertical and horizontal magnifications, Ω is the collection solid angle, and η is the collection efficiency including any losses due to reflectivity or bandwidth limitations. The scaled image brightness $\Omega\eta/M_v M_h$ (units of Sr), achievable while meeting a specified requirement for source spatial resolution over a given field of view (FOV), therefore serves as a figure of merit with which to weigh the various options.

Calculations and Results

In a detailed separate paper,¹⁴ we have investigated the achievable image brightness for several options in various configurations using analytical derivations backed by numerical ray tracing. There, we used a geometrical optics analysis to estimate Ω and η for 1D and 2D imaging near 6 keV with the Mn K- α ($E = 5.9$ keV, $\lambda/\Delta\lambda \approx 200$) and the Mn He- α ($E = 6.15$ keV, $\lambda/\Delta\lambda \approx 2000$), comparing the achievable image brightness for an Ir mirror KB; a multilayer mirror KB;¹⁵ a depth-graded multilayer mirror KB;¹⁵ a bent-crystal KB using mica in 3rd order;¹⁶ Si (220) [Ref. 17], LiF (220) [Ref. 17], and Si (422) [Ref. 17]; and a spherical crystal using Si (422) [Ref. 17], CaF_2 (111) in 3rd order¹⁶ and quartz 2243.¹⁸ In this paper we present only the results, and refer the interested reader to Ref. 14 for further details.

In Figures 1 and 2 we plot the estimated image brightness for 2D imagers using the Mn K- α source and the Mn He- α source, respectively, assuming a 200-mm source/optic distance and a magnification $M = 4$, while maintaining a spatial resolution better than $10 \mu m$ throughout a 2-mm FOV. For comparison, we also plot the estimated image brightness for an 8- μm -diam pinhole operating at $M = 4$ with a detector distance of 200 mm. In Figures 3 and 4 we plot the estimated image brightness for 1D imagers using the Mn K- α source and the Mn He- α source, respectively,

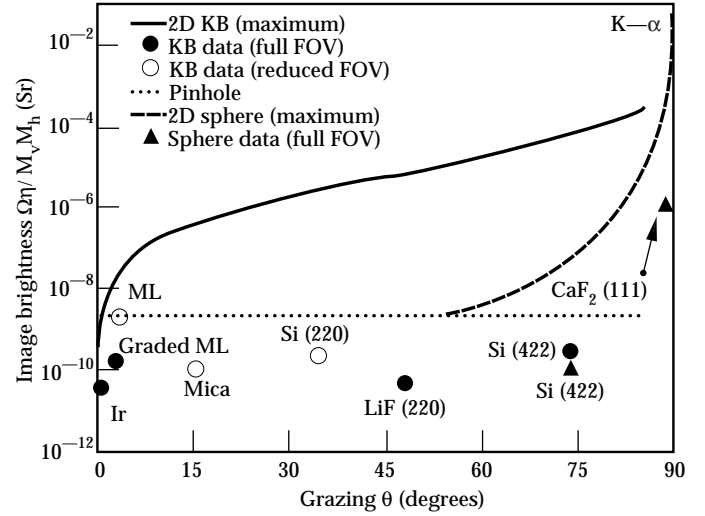


FIGURE 1. Estimated image brightness for several choices of 2D imaging microscope configurations and mirror materials assuming the Mn K- α line is used for imaging. (08-00-0598-1166pb01)

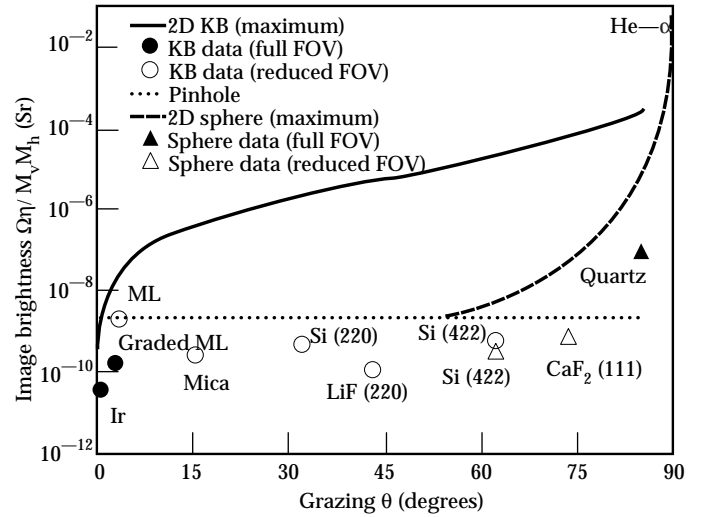


FIGURE 2. Estimated image brightness for several choices of 2D imaging microscope configurations and mirror materials assuming the Mn He- α line is used for imaging. (08-00-0598-1167pb01)

assuming a 200-mm source/optic distance and a magnification $M = 40$ in the spatially resolved dimension, while maintaining a spatial resolution better than $3 \mu m$ throughout a 0.3-mm FOV and integrating over a 0.3-mm region in the nonimaged dimension of the target. For comparison, we also plot the estimated image brightness for a 2.8- μm -wide slit operating at $M = 30$ with a detector distance of 200 mm. Those instruments that are not capable of achieving the required FOVs due to reflector or source bandwidth limits (discussed later) are shown as open circles or triangles in all cases.

We first discuss the results for 2D microscopes. As Figures 1 and 2 show, metal-mirror KB systems generally provide low image brightness compared with other designs for the parameters considered, primarily due to severe obliquity that necessitates small solid angles in order to maintain the desired resolution over the FOV. In addition, surface roughness becomes an increasing problem for higher photon energies, and this can degrade resolution by producing diffuse scattering.

For the parameters considered, a KB using conventional multilayer mirrors is more efficient than one using depth-graded multilayer mirrors. This is because the bandpass of the conventional multilayer mirror is sufficient to avoid chromatic vignetting of the collection angle, caused by the variation in the angle of incidence θ across the mirror surface, while providing a peak reflectivity that is a factor of ~ 4 higher than the depth-graded mirror. We note that in the bent-crystal KB systems, the integrated reflectivity of each crystal considered is small compared with that of a multilayer mirror, and the increased geometrical solid angles achievable at larger θ are more than offset by decreased efficiency, resulting in low image brightness for all bent-crystal KBs investigated.

It is clear in principle from Figures 1 and 2 that for the 2D imaging cases we consider here, spherical crystals operating within ~ 5 – 10° of normal incidence meet the specified requirements for source resolution over a specified FOV while providing the highest efficiency of any system considered. This is because the geometrical optics-limited collection angle is relatively large near normal incidence, because chromatic vignetting of the collection angle is less important near normal incidence since θ varies less across the aperture, and because there is only one reduction in image brightness for crystal efficiency. Indeed, we note that a two-crystal KB using Si 422 mirrors yields an image brightness only slightly higher than that obtained with a single Si 422 spherical crystal, despite the fact that the angle of incidence is far from normal (~ 65 – 70 degrees) and that the geometrical aberration-limited collection angle of the KB is much greater than that of the spherical mirror. Compared with multiple-crystal compound systems,¹¹ the use of toroidal crystals may generally be a more efficient means of increasing image brightness for off-normal angles of incidence by minimizing astigmatism and allowing larger apertures to be used.

While the collection solid angle of a pinhole is small, it has an efficiency of unity, and, for the parameters considered, the near-normal-incidence spherical crystals are the only systems that yield an image brightness larger than that obtainable with the chosen short-working-distance pinhole. Pinholes have compensating disadvantages, however, including possible closure during the experiment,⁶ increased parallax across multiple-frame

images, and high-energy x-ray transmission through the substrate. The last problem could be alleviated by the use of flat multilayer mirrors to reflect the image onto the detector, potentially eliminating a direct line of sight from the detector to the target.¹⁹

Many of the above comments also apply to the 1D imaging results of Figures 3 and 4. The image brightness of all bent-crystal KB systems are relatively low compared with the other systems considered, and are generally even lower than the Ir-mirror KB. However, in the 1D imaging case, the conventional multilayer KB yields an image brightness higher than any spherical

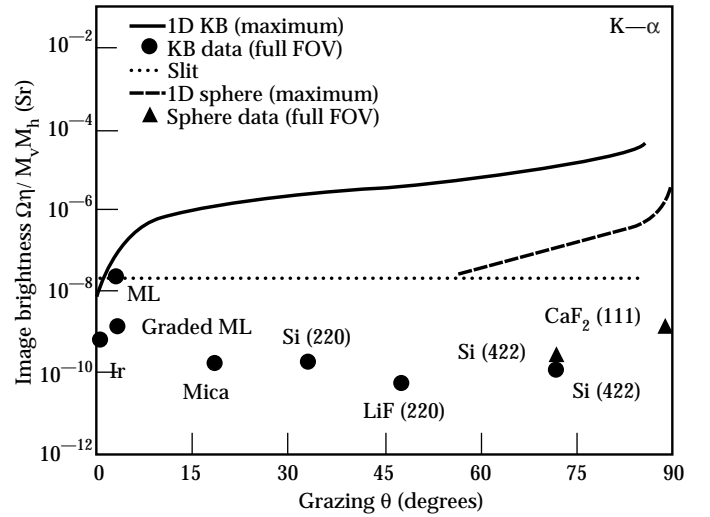


FIGURE 3. Estimated image brightness for several choices of 1D imaging microscope configurations and mirror materials assuming the Mn K- α line is used for imaging. (08-00-0598-1168pb01)

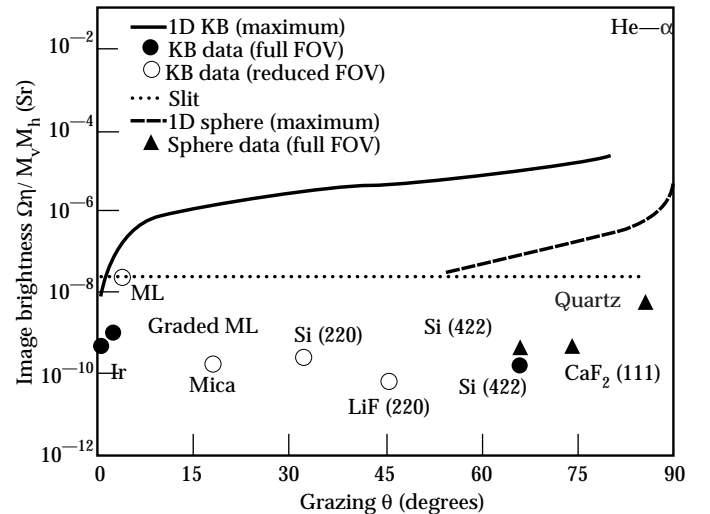


FIGURE 4. Estimated image brightness for several choices of 1D imaging microscope configurations and mirror materials assuming the Mn He- α line is used for imaging. (08-00-0598-1169pb01)

crystal considered, by a factor >10 . Much of this increase is due to the fact that the horizontal KB mirror is configured in this system to operate at $M = 1$, while the spherical crystal must operate with $M = 40$ in both dimensions. In addition, the choice of $M = 1$ eliminates chromatic vignetting of the collection angle in the horizontal dimension because the angles of incidence for all rays from an on-axis source point are equal, thus allowing the full (large) horizontal aperture to be used. We note that a toroidal bent crystal is unlikely to yield a significant increase in image brightness for 1D imaging because high resolution is required in one dimension only. However, the spherical crystal retains the significant practical advantage of simplicity, and the reduction in image brightness is likely to be tolerable in many cases provided the spherical crystal can actually meet the $3\text{-}\mu\text{m}$ source resolution requirement.

The chosen short-working-distance slit in Figures 3 and 4 yields an image brightness equal to or larger than that attainable with any reflective-optic imaging system considered. However, the compensating disadvantages of the pinhole also apply to the slit, and are in fact more significant here because the working distance is very short and the required slit width is very small. Slit closure problems could be minimized by moving the slit and detector farther from the target, at the cost of reduced image brightness and more significant diffraction limitations.

Discussion and Conclusions

It appears that spherical or toroidal crystals may be the most promising general options for high-energy x-ray microscopy applications at NIF. These optics can provide high throughput for 2D applications and can also provide good throughput for 1D applications, provided the operating wavelength matches a useful emission line and provided the bent crystal quality is high. Their simplicity is also attractive, particularly for 2D applications requiring multiple images onto gated microchannel-plate strips. Due to the low integrated reflectivity of most useful high-resolution imaging crystals, toroidal crystals are apparently a more efficient means of increasing collection angles for off-normal angles of incidence than compound-crystal systems.

Multilayer KB systems using spherical mirrors appear to be good options for 1D applications requiring high spatial resolution over narrow FOVs, and are most efficient when mirror bandwidths are just large enough to avoid chromatic vignetting of the collection angle while maintaining the highest possible peak reflectivity. These systems are also good secondary options for 2D applications. More complex multiple-optic compound systems might allow larger collection angles to be used provided the mirror bandwidths are sufficiently large, but their net advantages would have

to be weighed against their significant added complexity and cost, particularly for 2D imaging applications.

It is clear from Figures 1 through 4 that in many cases, the specified FOV cannot be achieved with bent-crystal KB systems or conventional multilayer-coated mirrors, and in some cases cannot be achieved even with near-normal-incidence crystals. This is due to chromatic vignetting of the FOV, caused by finite source linewidths and mirror bandwidths, and is particularly significant with the narrowband He- α source in Figures 2 and 4. For example, the maximum FOV of the multilayer mirror KB is ≈ 0.3 mm in all cases; mica, Si (220), LiF (220), and Si (422) bent-crystal KBs in Figures 2 and 4 have maximum FOVs of 0.06, 0.12, 0.2, and 0.4 mm respectively; and the CaF_2 (111) spherical crystal in Figures 2 and 4 has a maximum FOV of 0.7 mm. This obstacle to further Bragg reflector microscope development could be avoided by introducing apertures on the detector side of the mirrors, as illustrated in Figure 5. Here, the aperture is placed along the chief on-axis reflected ray at a distance $x = 2f$ from the mirror, where $f = Mp/(M + 1)$. The aperture width is chosen to limit the collection solid angle, while the mirror dimension limits the FOV. This geometry is similar to that used in a high-resolution metal-mirror KB microscope at Lawrence Livermore National Laboratory,⁵ where the backlight source was placed on the Rowland circle and the backlight diameter limited the collection solid angle and therefore determined the spatial resolution. However, as noted above, backlit imaging with the source on the Rowland circle will generally be impossible at NIF due to limited flexibility in laser beam pointing. The aperture technique described here does not require a backlight source on the Rowland circle, does not place any limitations on backlight dimensions, and can

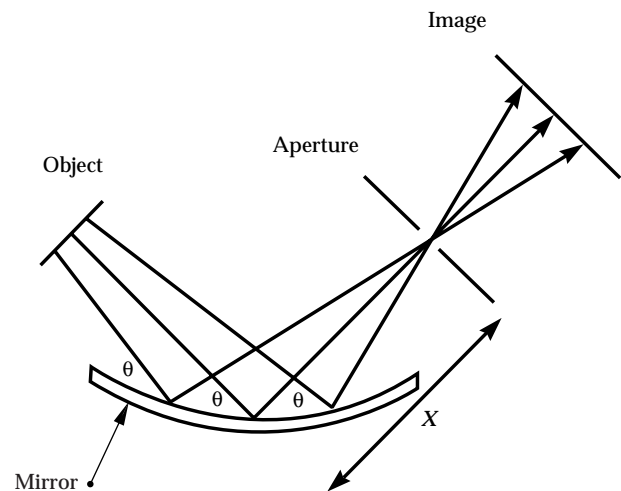


FIGURE 5. Sketch showing how an aperture, placed behind a mirror on the Rowland circle, can be used to minimize chromatic vignetting of the FOV with Bragg reflector mirrors. (08-00-0598-1170pb01)

be used for emission imaging. Further research is required in order to determine the geometrical limitations to the aperture width and thus the collection angle for this geometry.

The general utility of near-normal-incidence spherical or toroidal crystals for high-energy x-ray imaging at NIF and similar future facilities will depend on two main factors. The first is the limited choice of operating wavelengths, dictated by the requirement that θ be near 90° and by the limited number of useful crystal planes. We have begun a systematic search for matches between desirable source emission lines and crystal planes; however, further research will be required in order to determine the actual 2d spacings and integrated reflectivities for these crystals while bent to spherical or toroidal shapes. The second limiting factor for spherical crystal imaging is crystal quality. For high-resolution imaging applications, crystal perfection must be high, because mosaic structure will result in degraded spatial resolution; only highly perfect crystals can be used, and this factor will further limit the choices of operating wavelengths for spherical or toroidal crystals. Additionally, the mechanical properties of bent crystals are also important, as the crystals must retain high perfection while bent to spherical or toroidal shapes. Further research is required in order to assess these issues for specific crystal choices.

Acknowledgment

We gratefully acknowledge the contributions and support of M. Cable, R. Cauble, G. Collins, U. Feldman, J. Kilkenny, B. Remington, and J. Trebes.

References

1. J. Lindl, *Phys. Plasmas* **2**, 3933–4024 (1995).
2. P. Amendt et al., *Rev. Sci. Instrum.* **66**, 785–787 (1995).
3. I. Uschman et al., *Rev. Sci. Instrum.* **66**, 734–736 (1995).
4. B. A. Hammel et al., *Phys. Fluids B* **5**, 2259–2264 (1993).
5. L. B. Da Silva et al., *Phys. Rev. Lett.* **78**, 483–486 (1997).
6. B. A. Remington et al., *Rev. Sci. Instrum.* **63**, 5080–5082 (1992).
7. F. J. Marshall and Q. Su, *Rev. Sci. Instrum.* **66**, 725–727 (1995).
8. J. H. Underwood et al., *Rev. Sci. Instrum.* **67**, 1–6 (1996).
9. C. Brown et al., *Rev. Sci. Instrum.* **68**, 1099–1102 (1997).
10. M. Dirksmüller et al., *Opt. Comm.* **118**, 379–387 (1995).
11. E. Förster et al., *Exp. Tech. Physics* **42**, 19–24 (1996).
12. H. Wölter, *Ann. Physik* **10**, 94–114 (1952).
13. R. Kodama et al., *Opt. Lett.* **21**, 1321–1323 (1996).
14. J. A. Koch et al., *Appl. Opt.* (in press).
15. J. F. Seely et al., *Appl. Opt.* **35**, 4408–4412 (1996).
16. H. T. Yamada et al., Lawrence Berkeley National Laboratory, Berkeley, CA, Report No. LBL-22800 (1986).
17. B. L. Henke, E. M. Gullikson, and J. C. Davis, *Atomic Data and Nuc. Tables* **54** (2) (1993).
18. N. G. Alexandropolous and G. C. Cohen, *Appl. Spectrosc.* **28**, 155–164 (1974).
19. J. L. Bourgade et al., *Plasma Phys. Rep.* **20**, 107–112 (1994).

LASER-ELECTRON CONVERSION EFFICIENCY AT INTENSITIES GREATER THAN 10^{19} W/CM²

K. B. Wharton

J. Moody

B. Hammel

A. A. Offenberger

S. Hatchett

M. Perry

*C. Joshi**

S. C. Wilks

M. Key

V. Yanovsky

Introduction

Experimental investigation of plasma phenomena in ultraintense laser fields, in which electrons oscillate at relativistic velocities, has recently become possible with the advent of multiterawatt, short-pulse lasers. Several mechanisms that can transfer laser energy to the plasma electrons have been described.¹ One proposed application for such energetic electrons is sparking a fusion reaction in the fast-ignitor scheme.² Crucial, but unresolved, issues include the conversion efficiency of laser energy to electron energy, electron directionality, and temperature or mean energy of the electrons. We present the first measurements of the full, forward-hemisphere, laser-to-electron conversion efficiency, directionality, and mean electron energy in laser-solid interactions at incident laser intensities of 2 to 4×10^{19} W/cm². Such parameters will help determine the feasibility of the fast ignitor scheme in future laser facilities, such the National Ignition Facility.

One mechanism for collisionless laser-electron coupling in a plasma is the $-e \mathbf{v} \times \mathbf{B}$ Lorentz force on electrons oscillating in the electromagnetic field of a high-intensity laser. When the laser fields terminate at a critical-density surface, this force can ponderomotively accelerate electrons in the direction of laser propagation.³ Other collisionless laser-electron coupling mechanisms at the critical density include resonance absorption,⁴ parametric instabilities,⁵ and vacuum heating.⁶ Coupling at subcritical densities associated with the excitation of electron plasma waves can also accelerate plasma electrons.⁷ Previous

experiments have measured laser-accelerated electrons at lower intensities.⁸⁻¹⁴ One recent experiment using strongly relativistic intensities ($I\lambda^2 > 10^{19}$ W cm⁻² μm²) measured high-energy electrons in vacuum after leaving a foil target in which they were produced.¹⁵

Experimental Configuration

Our experiments were performed at the Nova laser facility at Lawrence Livermore National Laboratory (LLNL) on a beamline that uses chirped-pulse amplification.¹⁶ This short-pulse system supplies 12 to 30 J of 1.06-μm light in 400 fs. The peak intensity is 10^7 times greater than the amplified spontaneous emission (ASE), which begins about 3 ns before the main pulse. An additional 400-fs prepulse, reaching $\sim 10^{-3}$ of the peak intensity, arrives ~ 2 ns early. The final focusing optic is an $f/3$ off-axis parabola, which produces a measured 15-μm full-width-at-half-maximum (FWHM) focal spot (peak intensity of 4×10^{19} W/cm² for 30 J). Measurements¹⁷ and simulations show that the ASE and prepulse create an underdense plasma in front of the target with a scale length on the order of 10 μm. In this plasma, the intense laser may experience further self-focusing.^{18,19}

Both the temperature and absolute number of the laser-produced electrons were characterized by detecting the electron-induced K_α x-ray emission from buried layers in multilayer targets, which is a well established technique.^{8-12,14} This is an indirect method for measuring electrons before they leave the target via the inner-shell ionization of a tracer material at a known depth in the target. By varying the depth of the tracer layer, an electron spectrum can be inferred from the corresponding change in the K_α x-ray yield.

*University of California at Los Angeles, Los Angeles, CA

In the experiment, P-polarized laser light was incident at 25° to the target normal. The front (laser-incident) layer of the target was a 6- × 8-mm rectangular foil of various materials (CH, Al, or Cu) with a mass per unit area ranging from 0.02 to 0.45 g/cm². The middle layer of the target was a smaller (5- × 7-mm) foil of 50-μm-thick Mo. Electrons produced in the front layer transported into this Mo layer, knocking out inner-shell electrons and creating 17.5-keV K_{α} x rays. Finally, a layer of 1-mm-thick CH (6 × 8 mm) covered the back of the target, which protected the Mo layer from electrons that might return to the target (those pulled back by electrostatic forces). This CH layer stopped electrons with energies less than 300 keV (550-keV attenuation for a double pass), but had a negligible effect on the 17.5-keV x rays. We found that this layer lowered the Mo K_{α} x-ray signal by a factor of ~2, indicating that most of the K_{α} radiation was produced by electrons, not x rays.

We chose Mo for our tracer material so that the characteristic 17.5-keV K_{α} photon energy would be significantly greater than that of the x rays produced by the thermal plasma around the laser focus. This is important for avoiding photopumping of the K_{α} x-ray line.⁸ Spectroscopic measurements of an Al layer buried under a very thin layer of 5-μm CH showed a thermal plasma temperature of 300 to 600 eV in separate experiments with the same laser.²⁰ Further evidence that thermal x rays were unimportant was that the 20- to 30-keV x-ray spectrum was very similar from both the front and back of pure Al and Cu targets, which were optically thick in this energy range. This result signified that these x rays were predominantly bremsstrahlung photons produced throughout the cold target.

K_{α} x rays from the Mo layer were detected by a 16-bit, charged-coupled-device (CCD) detector situated 2.16 m from the target and 45° from the rear target normal. The CCD was filtered with 75 μm of Sn, limiting the x-ray flux and making it unlikely that two high-energy photons would be absorbed in the same pixel. The counts recorded on each pixel were proportional to the x-ray photon energy. We performed a statistical analysis on each set of data to determine what fraction of the signal was obscured by double hits due to the lower-energy x-ray continuum.

The CCD camera was absolutely calibrated with a Cd-109 (22-keV) source at two different occasions during the experiments. The two calibrations agreed to within 3% and allowed us to calculate the number of incident x rays from the measured hits on the camera. To scale the 22-keV calibration energy to the 17.5-keV K_{α} x rays, we assumed that the detector response was proportional to the absorption of the 14-μm-thick Si CCD chip.

Theoretical Analysis

The many possible electron trajectories in the target made a comprehensive analytical description difficult. Instead, we used the electron-photon transport Monte Carlo code ITS to interpret the data.²¹ The output of the ITS code was the number of K_{α} x rays per steradian emitted from a given target in the detector direction, normalized to the number of source electrons. In addition to calculating electron transport and ionization, ITS also computed the x-ray continuum produced by bremsstrahlung of fast electrons and the resulting photoionization of Mo atoms. The photopumped K_{α} x rays were typically 10% of the total.

We assumed that the electron source has the form of a Maxwellian energy distribution, which has been seen in particle-in-cell simulations^{3,19} and in experiments.^{11,15} However, because there is no intrinsic reason for the electrons to be Maxwellian, we also ran ITS simulations of other possible distributions. For a relativistic Maxwellian, the mean electron energy E_0 ranges from $3/2 kT$ (nonrelativistic electrons) to $3 kT$ (highly relativistic electrons). We compared this to the case of a purely exponential spectrum $f(E) = \exp(-E/kT)$, for which $E_0 = kT$. The ITS results were entirely consistent to within 10% for these different spectra, provided that E_0 (not kT) was kept constant. This demonstrated that our technique is not sensitive to the tail of the electron distribution (the slope of which determines kT), but rather to the mean-energy bulk of the distribution. For this reason, our results are not directly comparable to some previous measurements of bremsstrahlung x rays or the high-energy electron tail.¹⁵ However, our technique is appropriate for measurements of absolute conversion efficiency, which depend on the mean energy E_0 .

One assumption required in ITS concerns the cone angle of the electrons. For now, we assume that the electrons spray forward isotropically from the laser focus into a full hemisphere; we further discuss this assumption later. ITS also assumes that the electrons transport through cold material, and the code ignores collective effects, such as self-consistent magnetic^{19,22} and electrostatic²³⁻²⁵ fields. Because of the complexity of the physics involved, our use of ITS is not intended to fully model the experiment, but is used as a benchmark for interpreting the data.

Results

Figure 1 shows the Mo K_{α} yields from the targets with Al front layers, along with the best fits from the ITS code. The slope of the data (on a log plot) is sensitive to the mean energy E_0 of the electrons, whereas the absolute magnitude yields the laser-to-electron

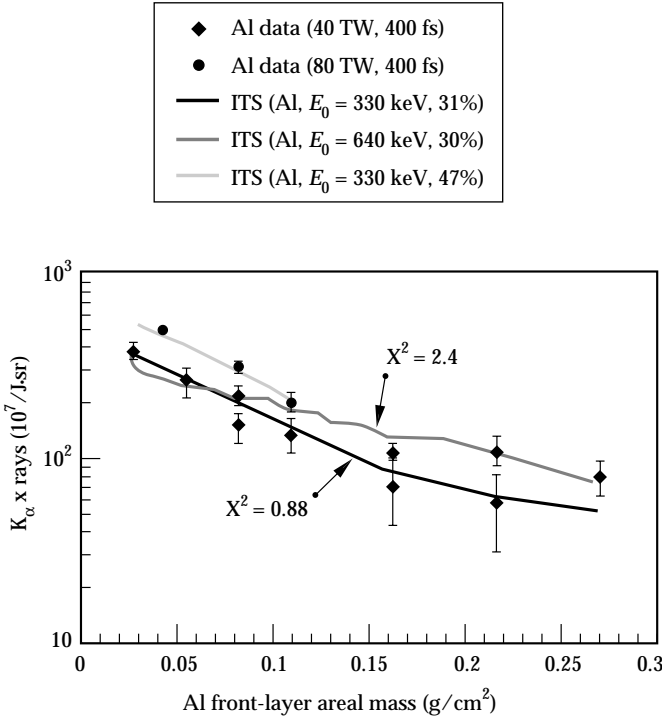


FIGURE 1. K_α signal from Al targets, in units of 10^7 x rays per incident joule and per steradian, vs areal mass of Al front layer of the target. Diamonds are experimental data at intensities of 4×10^{19} W/cm²; circles are data at 2×10^{19} W/cm². The ITS fits are listed by average energy E_0 and conversion efficiency η (in percent); some X^2 fit parameters are shown. All values of η are multiplied by 0.7 if the electrons are assumed to be directed in a 30° half-angle cone. (08-00-0598-1209pb01)

conversion efficiency η . Error bars were computed from a combination of counting errors and fluctuations in the background x-ray noise.

We fit the data with a series of ITS runs, which computed the K_α x-ray yield as a function of the transport-layer thickness for a given electron mean energy E_0 , and then found the conversion efficiency η that minimized the chi-squared (X^2) per degree of freedom. The data at an intensity of 2×10^{19} W/cm² are fit by an ITS run with $E_0 = 330$ keV ($kT = 170$ keV) and $\eta = 31\%$. For this fit, the X^2 is reasonably small (0.88). An ITS run for $E_0 = 640$ keV ($kT = 300$ keV) is also shown, although the X^2 of this fit is much larger (2.4). Three data points at an intensity of 4×10^{19} W/cm² show a greater η (47%), but roughly the same mean energy.

Figure 2 shows the experimental results for CH and Cu targets at a laser intensity of 2×10^{19} W/cm². The CH targets produced the smallest signal, corresponding to $E_0 = 120$ keV and $\eta = 29\%$. The Cu data have the largest error bars, due to higher x-ray noise, but are best

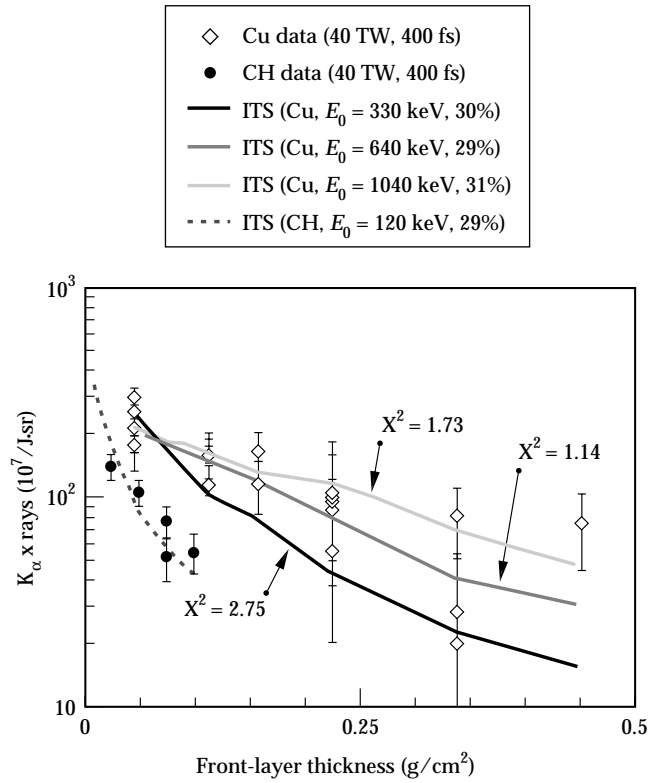


FIGURE 2. K_α signal from the target, with the same units as in Figure 1. Circles are data from CH front-layer targets; diamonds are data from Cu targets, both at 2×10^{19} W/cm². The ITS fits are listed by average energy E_0 and conversion efficiency η (in percent); some X^2 fit parameters are shown. All values of η are multiplied by 0.7 if the electrons are assumed to be directed in a 30° half-angle cone. (08-00-0598-1210pb01)

fit by $E_0 = 640$ keV and $\eta = 29\%$. Higher and lower energy fits to the Cu data are shown as well. The lower-intensity Al data from Figure 1 are at the same intensity, namely 2×10^{19} W/cm²; recall that these data were fit by $E_0 = 330$ keV and $\eta = 31\%$. The data show a change of mean electron energy with target material, although the conversion efficiencies remain roughly constant.

Electron Cone-Angle Measurements

The assumption that electrons are spraying into a full hemisphere might artificially increase the apparent conversion efficiency. To measure the directionality of electrons, a stainless-steel razor blade 750 μ m thick was placed between the back of the target and the CCD detector, creating a 1D penumbral image of the x-ray source on the CCD.^{11,26} Using this configuration, 2×10^{19} W/cm² laser pulses were shot at some of the previously

described targets: CH front layers (varied thicknesses), Mo middle layers, and optional CH back layers to prevent electron double hits. The lack of measured x rays above 6 keV from pure CH targets, along with the opacity of the razor blade to x rays under 25 keV, meant that the size of the 6- to 25-keV x-ray source was a good measure of where the electron beam intersected the Mo layer. Varying the depth of the Mo gave us an estimate of the electron cone angle.

Figure 3 shows the measured spot size of the x-ray source plotted against the buried depth of the 50- μ m Mo layer and compares these values to ITS calculations of the predicted measurements for electron beams with 30° and 90° half-cone angles. The large error bars result from the derivative that is required to extract the spot size from the data. For Mo layers buried 100 to 250 μ m into the target, the data roughly corresponds to an electron cone half-angle of 90°, a full hemisphere. However, for the thicker targets, the x-ray source corresponds closer to an electron beam of a 30° half-cone angle. Although the error bars are large, these data suggest some beaming of high-energy electrons (>200 keV) that penetrate through the thicker targets. The bulk of the

lower-energy electrons seem to be spraying into a full hemisphere. Using ITS to recalculate the conversion efficiencies based on a 30° half-angle electron source lowers η to 0.7 of the 90° values given above. The mean electron energies were not affected.

Applying this beaming effect to the earlier data, our measurements correspond to $\eta = 21\% \pm 5\%$ for all materials at a laser intensity of 2×10^{19} W/cm², and $\eta = 33\% \pm 5\%$ for the high-intensity (4×10^{19} W/cm²) shots on Al targets.

Discussion

The measurements of average energy seem to vary with target material rather than intensity. Our data shows that Cu-produced electrons are the most penetrating, although the error bars on the measurements still allow the possibility that the Al and Cu spectra could be equivalent. The CH electrons are less penetrating and apparently colder, although they seem to have roughly the same conversion efficiency as that for the Al and Cu targets. The conversion efficiency in CH, however, has an additional systematic error because the range of an $E_0 = 120$ -keV electron is smaller than the typical target thickness, which means that in CH we are not measuring the bulk of the electron distribution as we do in Al and Cu.

Bell, Davies, and collaborators have pointed out that strong material-dependent effects may result from differences in target conductivity.^{24,25} Conductivity has long been known to play an important role in shielding the resistive electrostatic field via a return current.²³ In our experiment, the return current also serves as the primary source of hot electrons, because the number of fast electrons we infer from our experiment is much greater than the number of electrons in a cubic laser spot size.

We have performed 1D LASNEX simulations²⁷ in which a high-energy Maxwellian distribution of electrons transport from the center of a solid-density sphere. The return current, heating, conductivity, and electrostatic fields are calculated self-consistently, and they show an ~40% loss of electron energy to resistive electrostatic fields. Other simulations have put this number at 30% (Ref. 25). This loss implies that our measurements of fast electrons place lower bounds on the original electron parameters, ideally requiring a correction for electrostatic effects.

However, electrostatic effects cannot fully explain the observed material dependence because η is not lowered by the same factor as E_0 in the different target materials. Another difference between the target materials is the underdense plasma that the ASE and prepulse form in front of the target. Our 2D calculations with LASNEX show a larger standoff between the critical and solid

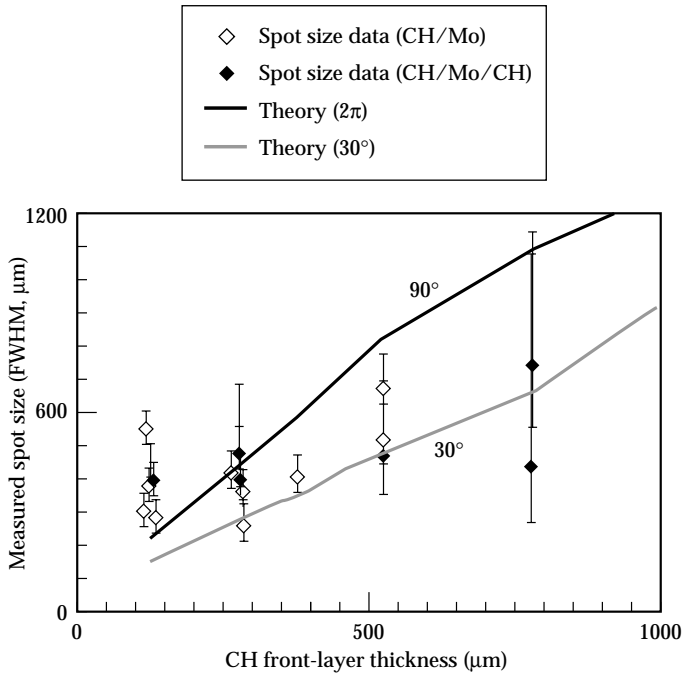


FIGURE 3. Measured size (FWHM in μ m) of the x-ray source plotted against thickness (μ m) of the front CH layer. Open diamonds are from targets with a back layer of 1-mm CH; solid diamonds had no CH back layer. The black line is an ITS fit of the expected results from an unbeamed electron source (90° half angle). The gray line is an ITS simulation of an electron source with a 30° half angle. (08-00-0598-1181pb01)

densities in CH (40 μm), compared to Al (22 μm) and Cu (18 μm). The difference is due to the variation in the Z of the target, and it will affect the intensity distribution of the laser through filamentation instabilities and relativistic self-focusing.^{18,19}

Summary

We have demonstrated a 20 to 30% conversion efficiency from laser energy into forward-propagated electrons in solid targets. The conversion efficiency seems to be a function of intensity, but not target material. A material dependence of electron temperature has been demonstrated for the first time at intensities greater than 10^{19} W/cm². Although this work will need to be extended to intensities of 10^{20} W/cm² to draw firmer conclusions on the feasibility of the fast ignitor fusion concept, this sizable conversion into forward-propagated electrons is an important validation for future research.

Acknowledgments

The authors would like to thank C. Brown, Y. Zakharenkov, J. Koch, and D. Pennington for their valuable contributions and assistance.

Notes and References

1. S. C. Wilks and W. L. Kruer, *IEEE J. Quant. Elec.* **33**, 1954 (1997).
2. M. Tabak et al., *Phys. Plasmas* **1**, 1626 (1994).
3. S. C. Wilks et al., *Phys. Rev. Lett.* **69**, 1383 (1992).
4. N. A. Ebrahim et al., *Phys. Rev. Lett.* **45**, 1179 (1980); F. Brunel, *Phys. Rev. Lett.* **59**, 52 (1987).
5. K. Estabrook and W. L. Kruer, *Phys. Fluids* **26**, 7 (1983).
6. F. Brunel, *Phys. Rev. Lett.* **59**, 52 (1987).
7. D. W. Forslund et al., *Phys. Rev. A* **11**, 670 (1975); G. J. Pert, *Plasma Phys.* **20**, 175 (1978); M. J. Everett et al., *Nature* **368**, 527 (1994); A. Modena et al., *Nature* **377**, 606 (1995).
8. J. D. Hares et al., *Phys. Rev. Lett.* **42**, 1216 (1979).
9. N. A. Ebrahim, C. Joshi, and H. A. Baldis, *Phys. Rev. A* **25**, 2440 (1982); B. Luther-Davies, A. Perry, and K. A. Nugent, *Phys. Rev. A* **35**, 4306 (1986).
10. H. Chen et al., *Phys. Rev. Lett.* **70**, 3431 (1993).
11. A. Rousse et al., *Phys. Rev. E* **50**, 2200 (1994).
12. Z. Jiang et al., *Phys. Plasmas* **2**, 1702 (1995).
13. U. Teubner et al., *Phys. Rev. E* **54**, 4167 (1996).
14. F. N. Beg et al., *Phys. Plasmas* **4**, 447 (1997).
15. G. Malka and J. L. Miquel, *Phys. Rev. Lett.* **77**, 75 (1996).
16. B. C. Stuart et al., *Optics Lett.* **22**, 242 (1997).
17. Y. Zakharenkov et al., *Rev. Sci. Instr.* **68**, 847 (1997).
18. C. E. Max et al., *Phys. Rev. Lett.* **33**, 209 (1974); P. Sprangle et al., *IEEE Trans. Plasma Sci.*, **PS-15**, 145 (1987); W. B. Mori et al., *Phys. Rev. Lett.* **60**, 1298 (1988).
19. A. Puhkov and J. Meyer-ter-Vehn, *Phys. Rev. Lett.* **76**, 3975 (1996).
20. J. Koch et al., *Lasers and Particle Beams* **16**, 225–232 (1998).
21. J. A. Halbleib and T. A. Mehlhorn, *Nucl. Sci. Engr.* **92**, 338 (1986).
22. M. G. Haines, *Phys. Rev. Lett.* **78**, 254 (1997).
23. D. J. Bond, J. D. Hares, and J. D. Kilkenny, *Phys. Rev. Lett.* **45**, 252 (1980).
24. A. R. Bell et al., *Plasma Phys. Control. Fusion* **39**, 653 (1997).
25. J. R. Davies et al., *Phys. Rev. E*, to be published.
26. A. P. Fews et al., *Opt. Commun.* **94**, 259 (1992).
27. G. B. Zimmerman and W. L. Kruer, *Comments Plasma Phys. Control. Fusion* **2**, 85 (1975).

LARGE-APERTURE COLOR-SEPARATION GRATINGS FOR DIVERTING UNCONVERTED LIGHT AWAY FROM THE NATIONAL IGNITION FACILITY TARGET

S. N. Dixit

T. Parham

L. Auyang

M. D. Perry

I. M. Barton

M. C. Rushford

J. A. Britten

L. J. Summers

S. M. Herman

I. M. Thomas

Introduction

Most of the glass, laser-based inertial confinement fusion (ICF) systems around the world today employ nonlinear frequency conversion for converting the 1.053- μm light at the fundamental frequency (referred to as 1ω light) to either its second harmonic (2ω) at 527 nm or to its third harmonic (3ω) at 351 nm. Shorter wavelengths are preferred for laser fusion because of the improved coupling of the laser light to the fusion targets due to reduced fast-electron production at shorter wavelengths. The frequency conversion process, however, is only about 60 to 70% efficient, and the residual 30 to 40% of the energy remains at 1ω and 2ω frequencies. The unconverted light, if permitted to interact with the plasma surrounding the target, could seed the production of fast electrons and could also stimulate the scattering processes in the plasma, scattering the 3ω light into light of longer wavelengths. These processes could prove detrimental to the ICF process itself. It is therefore desirable to move the unconverted light away from the ICF target.

Different strategies have been adapted for diverting the unconverted light away from the fusion target. On the Nova laser system at Lawrence Livermore National Laboratory (LLNL) and on the Phebus laser system at Limeil, France, the chromatic aberration in the focusing lens is used to cast a shadow of a 15-cm-diam circular obscuration at the center of the near-field profile to prevent the 1ω and 2ω light from hitting the target located at the 3ω focus. Here, different focal lengths at the 1ω and 2ω wavelengths lead to scaled-down, quasi-far-field profiles of the input beam at the 3ω focal

plane. The shadow of the obscuration then prevents the unconverted light from hitting the target. At the OMEGA laser system at the University of Rochester, the unconverted light is filtered out using the differing reflectivities of a multilayer turning mirror. In the proposed French Laser MegaJoule (LMJ) design, the unconverted light is prevented from entering the target chamber altogether by the use of high-efficiency diffraction gratings.

Earlier designs for the proposed National Ignition Facility (NIF) at LLNL employed a wedged final focusing lens to divert the unconverted 1ω and 2ω light away from the laser entrance hole and the outer surface of the hohlraum. The increased thickness of the glass in the ultraviolet (UV) beam path leads to a larger nonlinear B-integral, which can degrade the beam quality and focusability of the 3ω light. In addition, larger deflections of the 1ω and 2ω light (if needed) would demand an even thicker wedge on the lens, further exacerbating the B-integral problem.

Recently, we have proposed the use of a color-separation grating (CSG) to move the unconverted light away from the target in the NIF laser.¹ CSGs²⁻⁶ offer a versatile approach to reducing and possibly eliminating the unconverted light at the target region. A CSG (shown schematically in Figure 1) consists of a three-level lamellar grating designed so that nearly all of the 3ω light passes through undiffracted while the residual 1ω and 2ω energy is diverted with high efficiency into higher diffraction orders. The diffraction angle is determined solely by the grating period. Because a CSG profile is only a few wavelengths deep, the CSG can be fabricated on a thinner optic. The reduced amount of fused silica in the beam path lowers the B-integral,

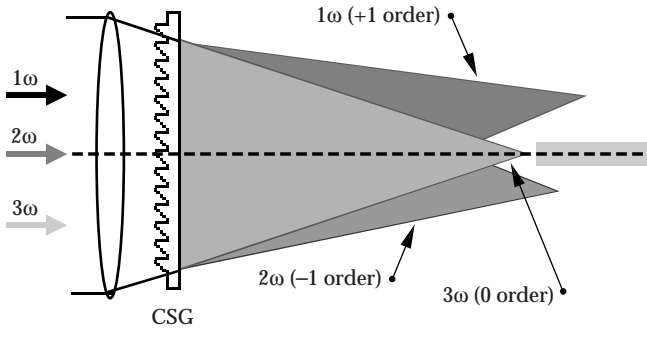


FIGURE 1. Schematic description of a CSG. For the sake of clarity, we have shown only the dominant diffraction orders for 1ω , 2ω , and 3ω wavelengths. In reality, the unconverted light is diffracted into several orders. (70-00-0598-1196pb01)

thereby reducing the nonlinear effects and consequently increasing the safety margin in the operation of high-power fusion lasers such as the NIF.

The current NIF baseline employs a CSG for diverting the unconverted light away from the target. Typical grating periods for NIF color separation are in the 300- μm range. The actual CSG grating period and the orientation of various CSGs on the NIF beams are still being determined. However, to demonstrate the technology of these CSGs, we have fabricated a 345- μm period CSG at the full-NIF aperture using a lithographic process similar to that used in the kinoform phase plate fabrication.⁷ This CSG will be fielded in the upcoming experimental campaign on LLNL's Beamlet (a prototype of a single NIF beamline).

CSG Theory

In this section, we briefly outline the theory of CSGs and discuss the sensitivity of the CSG efficiency to various fabrication parameters. A schematic diagram of a CSG is shown in Figure 1. It consists of a three-level, staircaselike lamellar structure. Although CSGs consisting of more than three levels can be designed, a minimum of three levels is required to achieve the color separation functionality desired on the NIF. The height of each step is chosen so that a relative phase delay of 2π is introduced for the 3ω light. If d denotes the period of the grating, and λ the operating wavelength, then the angle of diffraction for the m^{th} order when light is incident normal to the CSG is given by the standard grating equation

$$\sin[\theta_m(\lambda)] = m \frac{\lambda}{d} . \quad (1)$$

Within the approximations of the scalar diffraction theory,⁸ the diffraction efficiencies in various orders are given by the following equation

$$\eta_m = \left| \sum_{j=1-3} e^{-i\phi_j} \frac{n(\lambda)-1}{n(\lambda_0)-1} \frac{\lambda_0}{\lambda} e^{i2\pi m \epsilon_j} \delta_j \text{sinc}(\pi m \delta_j) \right|^2 , \quad (2)$$

where ϕ_j denotes the phase delay introduced due to the step j at the design wavelength λ_0 (351 nm), and ϵ_j and δ_j denote the locations of the center and the width of each zone within one CSG period. ϵ_j and δ_j are normalized to the grating period. For a regularly spaced grating, $\delta_j = 1/3$ for all j and $\epsilon_j = 1/6, 1/2$, and $5/6$ for $j = 1, 2$, and 3 . The factors multiplying the phase ϕ_j account for the material dispersion and the chromatic dispersion due to the CSG profile.

If $\phi_j = 0, 2\pi$, and 4π for $\lambda_0 = 351$ nm, then the grating appears transparent to the 3ω light, and all the 3ω light passes through undiffracted in the zeroth-transmitted order. Interestingly enough, this three-level lamellar profile also implies a theoretical zeroth-order efficiency of zero for the 1ω and 2ω light in the absence of any material dispersion. The variation of the refractive index with wavelength leads to a small zeroth-order diffraction efficiency for 1ω and 2ω . Table 1 lists the theoretical diffraction efficiencies for a few orders around 0 and for 1ω , 2ω , and 3ω wavelengths. These results are based on the scalar

TABLE 1. CSG diffraction efficiencies in various orders (Eq. 2). Refractive index values for fused silica were used in these calculations. These are $n = 1.44976, 1.46097$, and 1.47672 at $1\omega, 2\omega$, and 3ω respectively.

Diffraction order	1ω efficiency	2ω efficiency	3ω efficiency
-4	0.0002	0.0422	0
-3	0	0	0
-2	0.169	0.001	0
-1	0.003	0.675	0
0	0.005	0.006	1.0
1	0.678	0.005	0
2	0.0007	0.169	0
3	0	0	0
4	0.0422	0.0003	0

theory (Eq. 2), which is valid for grating periods much larger than wavelength. In this limit, the diffraction efficiencies are independent of the CSG period and are also insensitive to the polarization of the light.

It is clear from this table that about 88% of the 1ω light is diffracted into +1, -2, and +4 orders with the remaining energy distributed into many diffraction orders. The three-fold “skipping” of the diffraction efficiency is a consequence of the three-step structure in the CSG period. It is also interesting to note that, while the 2ω efficiencies are approximately the same as the 1ω efficiencies, the sign of the diffraction order is switched between 1ω and 2ω . This symmetry reversal results from the apparent reversal of the “blaze” between 1ω and 2ω . This can be understood as follows. Ignoring, for the simplicity of the argument, the material dispersion effects, the $0, 2\pi$, and 4π phase delays at 3ω appear as $0, 2\pi/3$, and $4\pi/3$ at 1ω and $0, 4\pi/3$, and $8\pi/3$ at 2ω . Because integral multiples of 2π phase can be arbitrarily added to each step without affecting the optical performance, it can be shown that the step structure within a CSG period appears reversed for 2ω wavelength as compared to that for the 1ω wavelength. This is illustrated in Figure 2. This reversed “blaze” leads to a switching of the diffraction efficiencies to opposite orders among the 1ω and the 2ω light, as shown in Table 1.

Actual phase at 3ω		Effective phase at 3ω	
	— 4π		
	— 2π		
— 0		—	— 0
Actual phase at 1ω		Effective phase at 1ω	
	— $4\pi/3$		— $4\pi/3$
	— $2\pi/3$		— $2\pi/3$
— 0		—	— 0
Actual phase at 2ω		Effective phase at 2ω	
	— $8\pi/3$	— $4\pi/3$	
	— $4\pi/3$	— $2\pi/3$	
— 0		—	— 0

FIGURE 2. Effective CSG phase for the converted (3ω) and the unconverted (1ω and 2ω) light. Note that by adding multiples of 2π phase, it can be shown that the “blaze” of the staircaselike CSG profile appears reversed for 2ω light compared to 1ω light. (70-00-0598-1197pb01)

Split Color-Separation Gratings

Eq. 1 indicates that the 1ω diffracted orders will have twice the angular spread as the 2ω diffracted orders. Unconverted light management on systems such as the NIF requires that the 1ω and 2ω light be moved a certain minimum distance away from the center. An improvement in the CSG designs can be achieved by reversing the lamellar CSG profile over half of the beam aperture, as shown in Figure 3. Such CSG profiles will be referred to as split CSGs. In this case, the dominant order for the 2ω light from each half of the beam is diffracted towards the same side, while that for the 1ω light “crosses” over to the opposite side. The larger deviation required to accommodate the crossover for the 1ω orders is provided by the larger 1ω diffraction angles. This translates into higher CSG periods for split CSGs to achieve a certain color separation compared to standard CSGs. For example, the CSG period required for moving the unconverted light footprints 1 cm away from the center is $243\text{ }\mu\text{m}$ for a standard CSG, while it is $381\text{ }\mu\text{m}$ for a split CSG. These CSG periods assume a 7.7-m focal length lens and a 400-mm near-field aperture for the beam. Larger CSG periods lead to lower fabrication errors, thereby leading to a higher CSG performance.

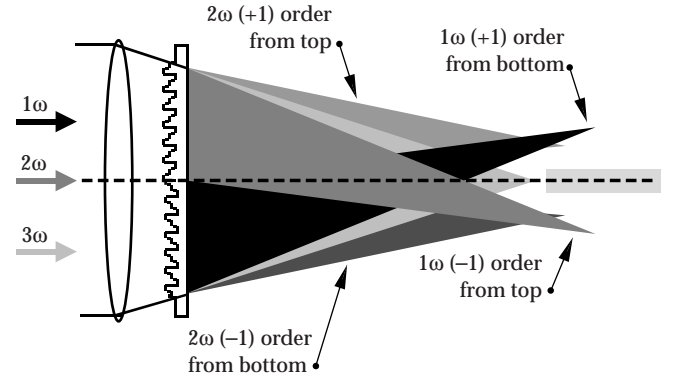


FIGURE 3. Schematic description of a split CSG. Note that the CSG profile is symmetric about the beam center. Again, for the sake of clarity, we have shown only the dominant diffraction orders for 1ω , 2ω , and 3ω wavelengths. In reality, the unconverted light is diffracted into several orders from the top and the bottom halves of the beam. (70-00-0598-1198pb01)

CSG Sensitivity to Fabrication Errors

The three-level CSG profile has to be fabricated using a two-mask lithographic process with either a wet etch or a dry etch into fused silica. The fabrication errors consist of errors in the etch depth and errors due to mask misalignment. Although the theoretical calculations above predict zeroth-order diffraction efficiency of unity for the 3ω light and nearly zero for the residual 1ω and 2ω light, fabrication errors in a practical application reduce the throughput at 3ω and increase the 1ω and 2ω zero-order light. Figure 4 displays the variation of the diffraction efficiency in the zeroth order with the etch depth error in the two steps. From these results we see that the etch depth has to be controlled to within ± 20 nm to maintain desirable 3ω focusing ($>98\%$ without accounting for Fresnel losses) and color separation ($<1\%$) characteristics.

The absolute etch depths required for each step of the CSG depend on its angle of use. In high-power laser systems, the diffractive optics are often used at off-normal angles of incidence to minimize ghost reflection issues. On the NIF, the CSG is planned to be used at 14° angle of incidence, whereas on Beamlet it will be used at 20 to 22° . The optical phase difference (OPD) between the etched and the unetched regions increases at small angles of incidence according to the formula

$$OPD \approx (n-1)t \left(1 + \theta^2 \frac{1}{2n} \right) \frac{2\pi}{\lambda}, \quad (3)$$

where θ is the angle of incidence, n the refractive index of the substrate relative to air (which is assumed to have refractive index 1.0), and t the relative step height between the etched and the unetched regions. This implies that diffractive optics, when used at oblique angles, have to be etched thinner than for normal incidence use. This is illustrated in Figure 5, where we plot the 3ω zeroth-order efficiency vs the CSG use angle for various etch depths for the first step (the second step etch depth is assumed to be twice the first step for simplicity). A 14° -use-angle CSG, for example, has to have an etch depth of 700 to 740 nm to maintain $>98\%$ 3ω zero-order efficiency, while for a 20° -use-angle CSG it has to be in the range 680 to 720 nm.

An additional effect of using the CSG at an off-normal angle is a reduction in the effective grating period by the cosine of the angle of incidence. At a 14° angle of incidence, the effective CSG period is reduced by 3%, while at 22° it is reduced by 7%. This leads to a corresponding increase in the diffraction angles for various orders. If the diffracted orders are required to be propagating at specific angles, then the effect of the CSG tilt can be compensated for in the actual CSG period fabricated.

Mask misalignment and problems associated with undercutting during the lithographic fabrication of a CSG lead to an erosion of the sharpness of the edge between the various steps in the CSG. Types of erosion consist of a rounding off of the edge of the CSG grooves, a lateral shift in the location of the edge, a misaligned overlay, etc. Often more than one type of error occurs in a given fabrication process. The dominant effect of these

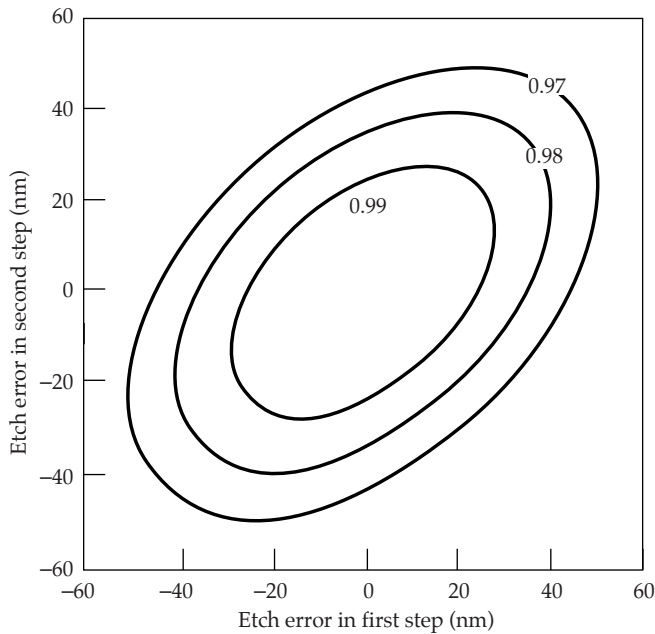


FIGURE 4. A contour map of the 3ω zeroth-order diffraction efficiency of a CSG as a function of the etch depth errors in the two steps. The values against each contour indicate the diffraction efficiency. (70-00-0598-1199pb01)

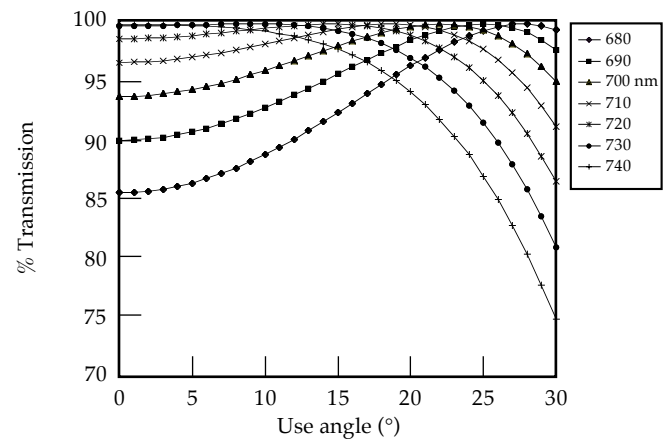


FIGURE 5. Effect of the use angle on the CSG 3ω transmission. Various curves correspond to different step heights for the 2π step. The 4π step is assumed to be twice as deep as the 2π step. (70-00-0598-1200pb01)

edge erosion errors is a loss of the 3ω zeroth-order efficiency. This loss can be simply estimated as the fractional area loss due to the edge degradation. Detailed calculations confirm this. The 3ω zeroth-order efficiency can then be written as

$$\eta_0 \approx \left| 1 - \frac{\Delta_1 + \Delta_2 + \Delta_3}{d} \right|^2 \approx 1 - 2 \frac{\Delta_1 + \Delta_2 + \Delta_3}{d}, \quad (4)$$

where Δ_1 , Δ_2 , and Δ_3 denote widths of the eroded edges. Thus, good alignment and edge definition control are required for maintaining high 3ω throughput. For example, for a CSG with a $300\text{-}\mu\text{m}$ period, a $1\text{-}\mu\text{m}$ -wide edge rounding at each step leads to a 2% loss of efficiency due to edge erosion. It should be mentioned that the 1ω and 2ω zeroth-order efficiencies are less sensitive to the effects of edge degradation and etch depth errors.

Fabrication of a Full-Aperture CSG for the Beamlet Laser

To demonstrate the concept of unconverted light management using CSGs, we fabricated a standard CSG having a $345\text{-}\mu\text{m}$ period in a Beamlet-size fused silica substrate ($\sim 400 \times 400\text{ mm}$) using a lithographic process and wet-etching process.^{7,9} This particular CSG period was chosen because we had previously fabricated CSGs at this period at smaller apertures¹ and also because this period is of the same magnitude required for the baseline NIF operation. The CSG fabrication method is schematically illustrated in Figure 6. The CSG substrate is first coated with a thin layer of chrome, and a layer of photoresist is deposited over it. This photoresist layer is then exposed to UV light from an arc lamp through a binary (in transmission) photomask. The exposed photoresist is developed away, and the chrome layer in these areas is removed using a chrome etch. This clears areas on the fused silica substrate that are subsequently etched in a buffered hydrofluoric acid solution. The etch depth is controlled by the time duration of the etch. Following the etching to a desired depth, the remaining photoresist is washed off. At this step, one set of the CSG grooves has been fabricated. This entire sequence of steps is repeated for a second time with a second photomask to etch the second set of steps in the CSG substrate. The second mask pattern is aligned carefully to the first etched pattern in the substrate by using a set of precisely located alignment fiducials. Finally, at the end of the sequence of steps using the second mask, the remaining chrome (over the grooves corresponding to zero phase) is etched off.

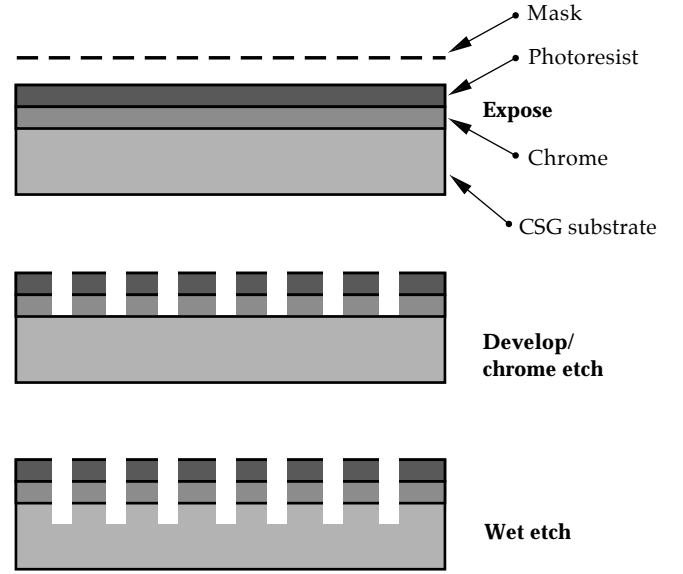


FIGURE 6. Schematic illustration of the various steps in the fabrication of a CSG by lithographic methods. (70-00-0598-1201pb01)

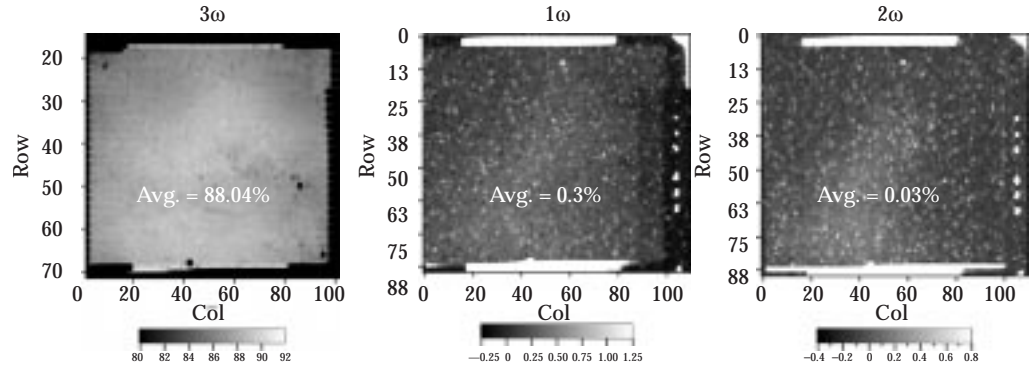
The binary photomasks required for the CSG fabrication were patterned in a chrome layer coated over a fused silica substrate using the large-aperture photoplotter developed at our laboratory. The available plotting area for the photoplotter is about $1 \times 1\text{ m}$ sq. The pixel positioning and the pixel size are accurate to $\sim 0.5\text{ }\mu\text{m}$ each over the entire plotting area. We believe that the edge definition through the sequence of the lithographic steps mentioned above erodes to $\sim 1.5\text{ }\mu\text{m}$. This leads to an $\sim 2.5\%$ reduction in the 3ω zeroth-order throughput.

We tried to achieve the desired etch depths of 720 and 1440 nm for the two CSG steps by first etching to 80% of the desired value, measuring the step height in a few selected places on the substrate, and then completing the remaining etch using an adjusted (if needed) etch rate. The etch depths on the finished parts were in the range of 704 to 743 nm (for the 2π steps) but varied somewhat over the 40-cm part. We believe this is due to a variation in the surface quality on the substrate that, as we shall see below, affects the uniformity of the 3ω diffraction efficiency.

Optical Performance

We characterized the optical performance of the CSG by measuring the zeroth-order transmission efficiencies 1ω , 2ω , and 3ω light. These measurements were carried out by scanning the full-size optic across an $\sim 5\text{-mm}$ collimated beam and collecting the transmitted light. The optic was not antireflection (AR) coated for these

FIGURE 7. Measured 1ω , 2ω , and 3ω zeroth-order transmission of a full-aperture (40-cm-sq) CSG. These measurements were carried out at 22° angle of incidence. The substrate was not AR-coated in these measurements. (70-00-0598-1202pb01)



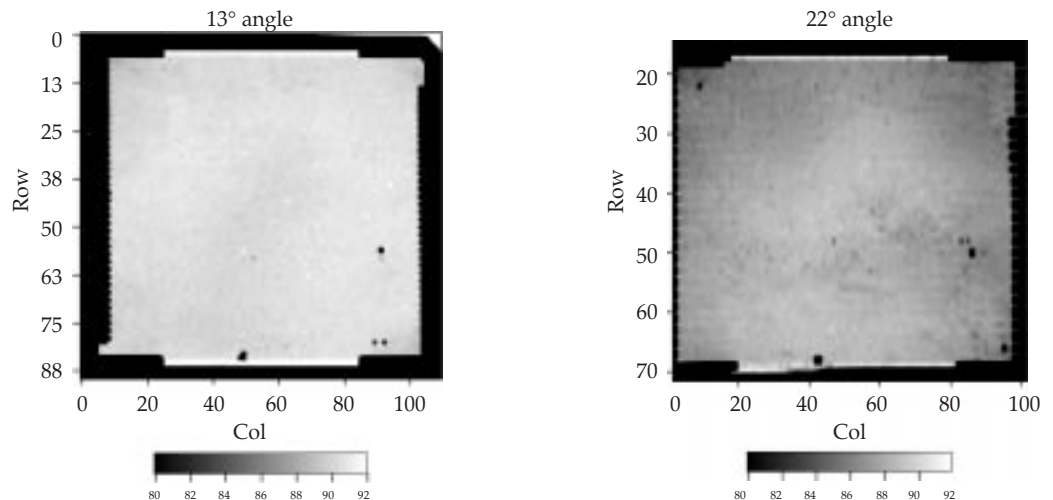
measurements. The measured transmission efficiencies are shown in Figure 7. We see from this data that excellent 1ω and 2ω suppression ($<1\%$ for each color) is achieved while the 3ω zeroth-order transmission is in the range of 86 to 89%, with an average value of 88%. Note that the 3ω transmission of an uncoated fused silica flat substrate is 92.5%. When normalized to this value, we can deduce that the normalized CSG efficiency is about 95%. Considerable variation of the 3ω zeroth-order transmission is observed across the 40-cm aperture. Through the measurements of the etched step heights using a white light interferometer, we have been able to qualitatively correlate the transmission efficiency nonuniformities to variations in the etch depth. We believe that the physical reason for this variation is an etch rate nonuniformity across the sample possibly introduced during the finishing process. The measured etch depths together with the data in Figure 5 indicate that at the NIF use angle of 14° , the expected variations in the 3ω zeroth-order transmission efficiency would be reduced. This was verified by measuring the transmission of this CSG at 13° . The results, shown in Figure 8,

indicate that diffraction efficiencies at this angle are in the range of 89 to 91%, with an average value of 90.7%. When normalized to the uncoated fused silica transmission (92.5%), we obtain a CSG efficiency of 98%.

Effect of Sol-Gel AR Overcoating on the CSG Performance

Optics used in high-power fusion lasers such as Nova and NIF are AR coated with an LLNL-developed sol-gel colloidal silica coating¹⁰ to increase the transmission efficiency. We AR coated a previously fabricated CSG using the dip-coating process normally used to coat Nova and NIF parts. We observed that when the CSG surface was AR coated, the transmission efficiency in the zero order was reduced compared to leaving the CSG surface bare. We found that the AR overcoating the CSG surface causes light to be scattered into the higher-transmitted diffractive orders to a greater extent than it reduces the back-reflection losses. This effect is shown in Figure 9. Approximately 7 to 10% of the total incident light is

FIGURE 8. A comparison of the 3ω zeroth-order transmission efficiencies at 13° and at 22° angles of incidence. Note the increased transmission value as well as its uniformity at 13° angle of incidence. (70-00-0598-1203pb01)



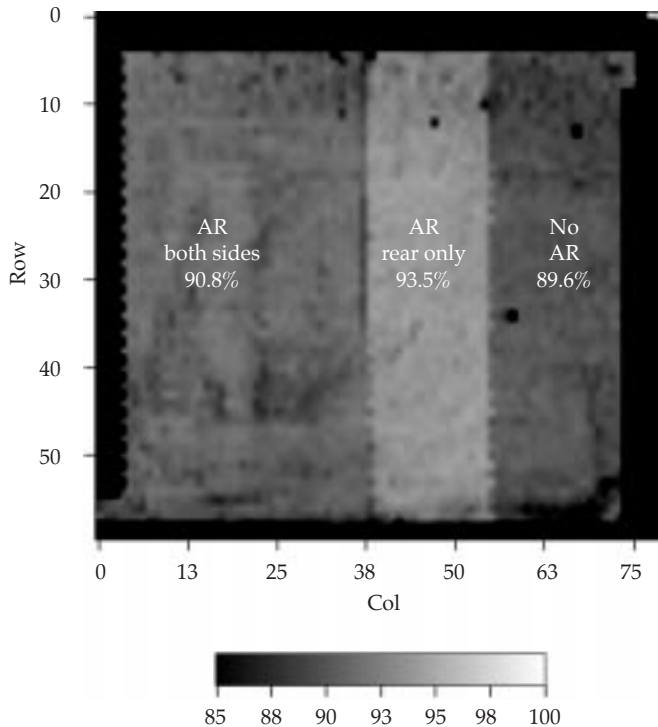
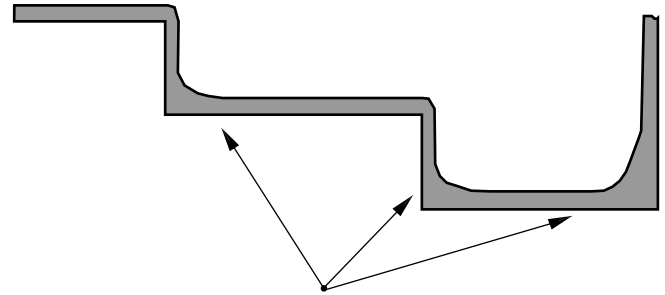


FIGURE 9. Effect of dip-coated porous silica antireflection coating on the 3ω zeroth-order transmission. The entire optic was dip-coated, and portions of the AR coating were stripped off from one or both sides to understand the effect of the AR coating on the CSG performance. (70-00-0598-1204pb01)

directed into the higher-transmitted diffracted orders by this coating, whereas losses into these orders are 2 to 3% for the bare surface. It is worth noting, however, that the zero-order transmission of 1ω and 2ω light is not affected by the AR coating.

Optical microscopy and detailed photometric examination of the amount of light scattered into individual higher-transmitted orders lead to the conclusion that these losses are due to a partial planarization effect of the coating. The coating is applied from liquid suspension by dip coating, a process in which liquid surface tension plays a crucial role. In the vicinity of the edges of the CSG pattern, surface tension effects cause a lateral flow of the liquid film during drying, which partially fills in and rounds the edges of the coated layer, as illustrated in Figure 10. This nonuniformity extends for several micrometers out into the grating line, in effect introducing a net sidewall slope error that, according to calculations, is sufficient to account for the measured zero-order losses.

This surface-tension effect is inherent in the dip-coating process and cannot be mitigated by, for example, changing solvents. The effect of surface tension on planarization is much less, however, for application of the AR coating by a spin-coating process. Preliminary data suggests that spin-coating of the same sol-gel AR



Edge effects disrupt AR performance

FIGURE 10. Schematic illustration of the planarization of the AR coating around the edges of a CSG. The rounded corners lead to a degradation of the CSG efficiency. (70-00-0598-1205pb01)

coating can achieve zero-order transmission efficiencies equal to or slightly better than the 95% NIF specification, although it is not as good as a completely conformal AR coating would be. Conformal coatings are possible if applied by vacuum deposition processes using refractory dielectric materials. Historically, these coatings have not been shown to have the required laser damage resistance, but improvements in the damage resistance of these types of coatings is ongoing. We are continuing to investigate the potential of spin coating the full-aperture CSG using the sol-gel system as well as evaluating the laser damage thresholds of possible hard-coat AR coatings.

Conclusions

In summary, we have designed and fabricated a CSG at NIF aperture sizes for use on the Beamlet laser. When the CSG is uncoated, its normalized optical performance is close to the expected values ($>97\%$ transmission in 3ω zeroth order without accounting for Fresnel losses and $<1\%$ in the 1ω and 2ω zeroth orders). We have observed an ~ 7 to 10% degradation in the 3ω transmission when the substrate is AR coated, and we are currently investigating its causes and possible solutions.

References

1. S. N. Dixit et al., *SPIE* **3047**, 463–470 (1997).
2. H. Dammann, *Appl. Opt.* **17**, 2273–2279 (1978).
3. T. Bett and I. Barton, private communication (AWE Aldermaston, Reading, UK).
4. M. B. Stern and G. J. Swanson, "Color separation echelon gratings," in *1996 Technical Digest Series*, vol. 5, Optical Society of America, April 1996.
5. M. W. Farn et al., *Opt. Lett.* **18**, 1214 (1993).
6. M. W. Farn et al., *NASA Conf. Publ.* **3227**, 409 (1993).
7. M. C. Rushford et al., *SPIE* **3047**, 282–291 (1997).
8. J. W. Goodman, *Introduction to Fourier Optics*, (McGraw Hill, New York, NY, 1988), p. 67.
9. S. N. Dixit et al., *Appl. Optics* **32**, 2543 (1993).
10. I. M. Thomas, *Appl. Optics* **25**, 1481 (1986).

NOVA/BEAMLET/NIF UPDATES

OCTOBER–DECEMBER 1997

R. Ehrlich/S. Burkhart/S. Kumpan

Nova Operations

Nova Operations performed 180 full system shots resulting in 197 experiments during this quarter. These experiments supported efforts in ICF, Defense Sciences, university collaborations, Laser Science, and Nova facility maintenance. At the beginning of the quarter the operation of Nova was reduced to 1.5 shifts. Toward the end of the quarter, Bechtel Nevada agreed to provide support for the operation of the target bay. This increase in staffing will allow Nova to again operate for two shifts per day later in the year, increasing the original goal of 700 experiments in FY98 to 900 experiments.

The final shots were fired into the two-beam target chamber this quarter. The two-beam facility was turned over to the NIF project as scheduled. (This process began in mid-November and was completed by the middle of January.)

The Petawatt system underwent a major reconfiguration to add a deformable mirror to the front end of the beamline. In preparation for focal-spot control test shots early in the next quarter, the deformable mirror was installed in conjunction with Hartmann sensors in the Petawatt master oscillator room (MOR), the beamline 6 output sensor, and the compressed beam diagnostic station. Many new diagnostics were installed on the Petawatt target chamber in preparation for the fast ignitor and radiography experiments that will be performed with focal-spot control.

Beamlet Operations

Beamlet completed a total of 40 shots in 16 shot days this quarter. Pinhole closure experiments were performed in October to evaluate the performance of a conical and pyramidal pinhole design of several sizes. Later in the month we prepared for a beamline reconfiguration of the National Ignition Facility (NIF) baseline

centered lens, because Beamlet had been originally laid out for a wedged lens which diverted the beam by 2.2° . This required us to offset and repoint the beam in a 4-mirror “mirror tower,” which carried the risk of beam rotation and depolarization. Thus the month of November was consumed measuring these beam properties prior to and following the mirror tower installation. In December, we ramped up the 1ω fluence on the mirrors to near their planned operating point, performed an additional week of pinhole closure tests, and assembled, installed and aligned the NIF prototype integrated optics module (IOM) and final optics cell (FOC). The operational and experimental highlights are as follows:

- The pinhole closure campaign was concluded in October, following tests with conical $100\text{-}\mu\text{rad}$ pinholes, conical $150\text{-}\mu\text{rad}$ pinholes, and the new truncated pyramid (square conical) $100\text{-}\mu\text{rad}$ pinhole. The pulse shape at the transport spatial filter was that calculated for the NIF cavity spatial filter in a nominal NIF red line pulse. It required a 20-ns pulse with a contrast of 90:1 at the MOR. The round $100\text{-}\mu\text{rad}$ pinhole showed initial signs of pinhole closure (contrast ratio increases) above 8 kJ, while the pyramidal pinhole closed hard at 7.0 kJ, and even closed for a 2.2-kJ “foot only” pulse. Fortunately these conical pinholes have virtually no backscatter. The conical $150\text{-}\mu\text{rad}$ pinhole remained open with no signs of closure to 12.9 kJ.
- One week was dedicated to measuring the depolarization of Beamlet at the focal plane prior to mirror tower installation. An extensive setup was assembled at the focal plane, and we measured the continuous wave (CW), rod-shot, and system-shot depolarization. We measured 0.18% CW, and only slightly greater for rod and system shots. Following mirror tower installation, the depolarization loss went up to 1%, which is

insignificant for Beamlet. In any case, we attributed the increased loss to alignment issues in the cavity and not the mirrors alone.

- Beamlet was reconfigured for the centered 3ω lens tests in the month of November. All previous 3ω experiments into the focal plane diagnostics (FPD) vessel used the old NIF baseline, the wedged lens, which required the FPD canted by 2.176° counter-clockwise from the 1ω output beamline. Rather than move the FPD, which would have been expensive and time consuming, we shifted the 1ω beam using the Beamlet mirror tower. This required an 18.5-cm beam offset to the south, and involved mixed “s” and “p” reflections
- The last of the thin (35-mm) lenses (L2) and one of the tilted 41-mm-thick lenses (L4) were replaced with 46-mm-thick normal-incidence fused-silica lenses. This was in preparation for the high fluences planned with the centered final focus lens tests commencing in January. Slight damage was found on the vacuum surface of L4, leading to the discovery of FOC back-reflection damage within the transport spatial filter, which has since been corrected.
- We executed 10 shots for the mirror testing, ramping up the fluence on the mirror tower transport mirrors to 8 J/cm^2 in a 3-ns pulse. The ultimate goal to be achieved on a later shot series is 12 J/cm^2 . We are testing mirrors with 45° , “s” polarization from four different vendors.
- Problems associated with FOC assembly caused us to insert a pinhole closure series in the third week of December. The goal for this short series was to confirm the Optical Science Laser (OSL) result that Ta leaf pinholes close slower than an equivalent configuration of stainless steel pinholes. This experiment had to be performed on Beamlet because of the higher axial intensity at focus compared to OSL. As expected, the $\pm 100\text{-}\mu\text{rad}$ Ta pinholes closed about half as fast as the stainless steel.
- FOC assembly problems were resolved by the end of the third week in December, and we were able to successfully assemble the cell. Several procedures were revised to accomplish this goal, including the main FOC assembly procedure. The cell and IOM were installed with initial alignment during the week before Christmas, and high-fluence 3ω experiments are planned for January. The rest of December was spent on focal-plane-diagnostics alignment and on activation of the Schlieren On-Line Imaging of Damage (SOLID) system, which uses dark field imaging of damage sites. It is our primary damage detection system for the final optics damage tests.

National Ignition Facility

Overall progress on the NIF Project remains satisfactory for the first quarter of FY98. Despite some delays resulting from unanticipated site conditions, the discovery of mammoth bones, and the rains in November, the overall Conventional Facilities construction schedule slippage was minimized through the use of overtime work. Work-around plans are now being developed to determine what future work to accelerate over the duration of the construction, through the use of accelerated performance contracts and change orders, to recover the original schedule. In Special Equipment, the Title II reviews are proceeding on schedule, and in Optics, the progress on facilitization contracts and development activities remains satisfactory.

There were no Level 0, 1, 2, 3 milestones due during the first quarter. There were 12 Department of Energy/Oakland Office (DOE/OAK) Performance Measurement Milestones due, and all but one (Conventional Facilities, Complete Target Bay Foundation Walls & Pilasters) were completed. One milestone in the Optics area—awarding the polarizer substrate contract—was completed four months ahead of schedule.

Key Assurance activities during the first quarter to support litigation activities and the recovery of mammoth bones included: providing support to the DOE for the settlement of 60(b) (Agreement to prepare a Programmatic Environmental Impact Study supplement analyses and to conduct specific evaluations and surveillance of potential buried hazardous materials), initiating the NIF Construction Safety Program, interfacing with institutional surveillance for buried hazardous/toxic and/or radioactive materials, initiating the *Final Safety Analysis Report*, conducting assurance audits, interfacing with the Safety Management Evaluation team on construction safety, and supporting environmental permits. All activities are on schedule.

Site and Conventional Facilities

The Title II design effort on the NIF Conventional Facilities continued to wind down during the first quarter, with all Construction Subcontract Packages (CSPs) at either Title II 100% design complete or already Bid and Awarded. CSP-9 (Laser Building Buildout and Central Plant) was awarded in December to Hensel-Phelps of San Jose, California, for \$65.5 million. CSP-6 and CSP-10 (Target Building Shell and Target Building Finish) will be bid as one contract CSP-6/10 (Target Area Building) in February 1998. Parsons Title II engineering design effort will also be complete in February 1998.

Construction of the retaining wall footing at the west end of the Laser Bay was adversely impacted by unanticipated site conditions, design delays in final configuration of the Environmental Protection System,

Walsh Pacific performance problems, and periods of heavy rain during November (see Figure 1). The Target Building portion of the retaining wall footing was remediated and concrete placed in December. Sverdrup (Construction Manager contractor) initially projected a slippage of 10 to 12 weeks in the Conventional Facilities construction schedule, if no activities were accelerated. The current assessment of Project status is that there will be no change to the fourth quarter 01 Level 2 milestone for the end of conventional construction, nor to the fourth quarter 03 Project completion date. However, it is anticipated that there could be a 3 to 6 week impact to the fourth quarter 01 Level 4 milestone for the start-up of the first bundle. There may also be a 6 to 8 week impact to other internal milestones for construction. These impacts are currently being assessed by the construction team and the integrated project scheduling group. Sverdrup is developing a recovery schedule that will require accelerated performance in contracts now being issued and will require change orders to contracts already issued.

Significant work was performed on site to recover and seal rain damaged subgrades, to protect the site by diversion and storage of water during high rainfalls, and to provide all-weather construction access to the jobsite. This site work was performed based upon recommendations from Earth Tech, specialists in wet weather construction from the Seattle area. Sverdrup directed the site remediation activities, and Teichert, a construction subcontractor, performed the work.

Bids were received for CSP-9 (Laser Building Buildout and Central Plant), and the contract was issued to Hensel-Phelps. Competitive bids were received from three bidders with an approximately 2% difference in bids between the two lowest bidders.

Mammoth Bones. Mammoth bones were discovered in the NIF excavation (Switchyard 1 near the Target

Area). The bones were recovered by a multidisciplinary team under the direction of a paleontologist who was recommended by the University of California Museum of Paleontology. A permit for the dig was issued by the Department of the Interior, and in accordance with the National Environmental Policy Act, a Supplemental Analysis was issued by the DOE. The bones were preserved in place, encased in fiberglass reinforced plaster, and carefully removed to safe and secure storage at the LLNL site. The work was accomplished in a manner that minimized delays to construction.

Special Equipment

This quarter the Special Equipment FY98 planning was completed, and the Integrated Project Schedule (IPS) has been updated to include the detail Title II plans. Title II guidance for design deliverables has been issued, and Title II design reviews continue to be held on schedule. Procurement reviews were also held. The reliability, availability, and maintainability (RAM) group is helping to produce prototype test plans and procedures.

Laser Systems. During the first quarter there was substantial progress in design and prototyping efforts in Laser Systems. A key accomplishment was resolving the lack of margin in the gain of the amplifier in the baseline design. This was noted at the Title I review and at the NIF Council review in August 1997. An Engineering Change Request (ECR) to allow 23% explosion fraction operation of the NIF amplifier, resulting in provision for increased capacitance in the pulsed power system, was submitted and approved by the NIF Level 4 Change Control Board (CCB) and by the Level 3 Baseline Change Control Board. This change provides for the addition of capacitors at a later date to provide additional gain in the main amplifier if needed. The change provides important contingency in the event of degradation or failure to meet requirements of the amplifier, flashlamps, pulsed power system, and/or main cavity optics.

Optical Pulse Generation. The 17-GHz phase modulator system required for smoothing by spectral dispersion was assembled and tested this quarter. The primary issues are operation of the modulator system and the appearance of amplitude modulation on the laser pulse due to FM to AM conversion of the modulation frequency. The significant modulation observed when the modulation frequency is applied to the fiber-optic system is substantially reduced when the modulation is applied directly to the preamplifier. In addition, assembly of the low-power side of the PAM prototype is under way, and the PAM optical support structure is in procurement with delivery expected in February.

Amplifier. Several meetings were held this quarter to freeze key elements of the amplifier design that must



FIGURE 1. Target Bay footing construction. (40-60-1297-2604pb01)

be detailed in the next six months. The major action items generated at the Title I Review and the NIF Council Amplifier Status Review have been resolved and documented. Gain and wavefront measurements on AMPLAB during the last quarter have so far validated the Amplifier design. An ECR was drafted and submitted to reflect a proposal to adopt slab sizes negotiated with the French Atomic Energy Commission (CEA). This will assure that the laser glass vendors will produce interchangeable slabs for both projects (NIF and Ligne d'Integration Laser [LIL], France's 8-beam prototype of their Laser Megajoule). Subscale tests validated the proposed blast shield seal design, and a decision was made to incorporate removable blast shields in the NIF amplifiers. A full-scale prototype design has been completed and parts ordered for testing on AMPLAB. Preferred blast shield glass and coating methods were chosen based on analysis and tests during the past quarter. The 40-flashlamp lifetime test fixture has been activated and successfully fired under manual control with a full complement of 40 flashlamps.

Pockels Cell. Assembly of the 4×1 operational prototype plasma electrode Pockels cell (PEPC) was completed during the past quarter, and testing of the device has begun. Two apertures (one-half of the device) have demonstrated switching performance that exceeds the NIF specification. Components for the 4×1 PEPC mechanical prototype have arrived, and assembly is in progress. Mounting, vibration, and other mechanical tests will be performed using this prototype over the next several months. A successful Mid-Title II (65%) design review was held for the PEPC in December. No significant issues were identified.

Power Conditioning: The NIF prototype module was assembled and activated during the past quarter at Sandia National Laboratories, Albuquerque. The module was operated at up to 15 kV for 10s of shots. A prototype embedded controller was installed and tested successfully during operation of the prototype. A request for quotations was issued for procurement of the capacitors for the first article module since these are long-lead components. Bids were received and will be evaluated for an award in January 1998. Test runs were completed on several switches, including two tests of the ST-300 and testing of the Russian reverse-switched-dynistor. In addition, arc-drop measurements were made on the ST-300 switch operating at full current. In response to the approval of ECR 189, preliminary planning and scheduling were done to estimate the ECR's impact on the Title II design process. Tests are now under way on NIF capacitors from four vendors with promising results on each to date.

Beam Transport System. After an intensive campaign to resolve all interface control documents and Mid-Title II action items for the Beam Transport System, over 500 prerelease drawings for the Title II Final Design Reviews (Part 1) were completed in

December. These drawings will undergo final checking and approval in the next quarter. Final Design reviews were held for three major subsystems that are on or near the critical path for laser installation, the Laser Bay structures, spatial filter vacuum vessels, and the Switchyard 2 structure. Construction Management began a significant ramp-up in activity, initiating a series of construction planning sessions that will ultimately produce a more detailed Integrated Project Schedule (IPS). A full-time construction planner was hired, and a preliminary laser installation strategy was established and reviewed. Design and environmental assessments of Special Equipment laydown areas were initiated, and construction is set to be awarded in January.

Integrated Computer Control System (ICCS). All Mid-Title II (65%) Reviews for WBS 1.5 are now completed. The Mid-Title II Review for Integrated Safety Systems, which includes the Personnel Access Control System and t-1 Abort System, Communications System, and Facility Environmental Monitor were completed in a joint session; no major issues were raised by reviewers. The Mid-Title II Review for Supervisory Software Applications was also completed with no major issues raised. The Mid-Title II Review for Integrated Timing System was held; reviewer comments are pending. The testbed front-end processors, prototype console, network switches, and Software Engineering Computer System were moved into the new ICCS Testbed Facility in B481/R1206. Network modeling tools were evaluated for use in simulating the ICCS computer network of approximately 800 processors. The MIL3 Opnet Modeler tool was selected because of its flexibility and its adoption for use at other DOE sites. The prototype front-end processor was upgraded from the original Datacube processor to the NIF configuration comprised of a Sun Enterprise 3000 server, which promises to be far more scalable to NIF requirements than the previous implementation.

Optomechanical Systems Management. The Optical Mounts group held the Mid-Title II review in November. Drawing packages for the optical mount prototypes were completed and released for fabrication. Prototype testing activity increased in the Final Optics group, and substantial optical design and analysis work was performed (e.g., ray tracing for optical configuration and ghost analysis). The frequency conversion verification system design was completed (prototype), and all parts are on order, with some parts received. Optical design accomplishments included completion of the target chamber damage inspection system, approval of prototype optics drawings for the preamplifier module (PAM), receipt of final design report for the main laser cavity and spatial filter lens design, release of optics drawings for the output sensor prototype, and release of large-aperture window drawings into configuration management. Detailed

product data structures (i.e., drawing trees or indented parts lists) were assembled, collated, and updated to a uniform format for all line-replaceable units (LRUs) within Opto-Mechanical Systems.

Optical Design. Detailed lens design for the multi-pass amplifier for the PAM prototype to be built in FY98 was completed this quarter. Fabrication drawings for the prototype were generated, reviewed, approved, and released. The target chamber damage inspection system optical design was also completed, and a comprehensive design report prepared. Optical element fabrication drawings for the output sensor prototype lenses, beam-splitters, and prisms were completed and released through the NIF Product Data Management System for fabrication. A previously reported problem (second-order ghost reflection focusing very close to the Pockels cell) was resolved by shifting the entire periscope structure 120 mm towards the target. In addition, the second stray light workshop was held in November. An update of issues from workshop #1 were presented, the main laser ghosts (including high-order and pencil beams) were reviewed, and the latest results from the extensive modeling of ghost reflections in the final optics were discussed.

Optical Components. The efforts for optics components and production continued on track in the areas of Mirrors, Small Optics, Processing, and Metrology/QA. Some key developments were the completion of efforts to identify all of the small optics required for the NIF in a single spreadsheet, binned into LRUs and types; the modeling of contamination conditions for sol-gel coatings; the completion of demonstrations to vendors and component engineers of the metrology data management system; and the award of the Phase II contract for the LLNL photometer.

Laser Control. The volume of procurements for prototype hardware was increased during the first quarter to provide more opportunities to validate key NIF designs. A few prototypes have already passed NIF life-time-equivalent tests; others have generated data that led to important adjustments in their design or in assembly procedures; and many are now in fabrication. Increasing numbers of detailed drawings were also completed as the mechanical designers gained familiarity with the Pro-E CAD tools in the context of detail production. A Pro-E model of the central part of the Transport Spatial Filter (TSF) and the space below it was nearly completed. This model is a key part of defining interfaces in the area. Mechanical and optical design of the input sensor was a major effort this quarter also. Improved packaging now separates the main beamline components requiring the highest level of cleanliness from other components with relaxed cleanliness specifications, placing them in completely separate modules that can be built, installed, or replaced independently.

Target Experimental Systems. Significant accomplishments in the past quarter were the forming of the first

two (of 18) plates for the aluminum vacuum chamber at Euroform in France (see Figure 2) and completion of most of the Special Equipment utility designs in the Target Area Building and support pads. The 110-mm-thick aluminum plates were warm-formed (316°C) on a 12,000-ton press between two dish shaped dies, and a preliminary inspection was made using a template. The plates matched contour within 5 mm and no thinning was evident. Prototype testing activity increased in the Final Optics group principally for the actuation system components, debris shield cassette components, and the integrated optics module. Testing of the prototype rail mechanism for debris shield removal was also completed, showing significant particle contamination from the rubbing of the slide mechanism with itself. Particle counts indicated more than 1600 particles of 5 μm or larger over a 4-in. wafer, which equates to a cleanliness level of 600 per Mil Std 1240. An ECR was approved by the Level 4 CCB to add a second "cassette" in the final optics assembly (FOA), and the team began implementing the change. This second, removable cassette would be the optical mount for the diffractive optics. A major factor in the decision was a significant reduction in out-year operating costs for a highly flexible target physics program. A complete set of ghost analysis runs was completed for the optical elements within the FOA consistent with the configuration as required by ECR 180. Of the three million ghosts analyzed through 4th order, 6000 had fluences at focus of greater than 1 J/cm². Of those, only two families were at or near optical elements. These were mitigated by adjusting the element spacing in the final optics system. Metrology measurements were made of the mounted crystals used in the recently completed frequency conversion experiments. The 18-in. phase-measuring interferometer in Building 298, with an improved setup, was able to record high-quality transmitted wavefront data that can be used for modeling degradation of frequency conversion due to Δn (change in index of refraction) effects.



FIGURE 2. Forming of Target Chamber plates at Euroform in France. (05-00-0398-0525pb01)

Operations Special Equipment

During the first quarter, Title II design progressed well. Key activities were the preparations for the Mid-Title II (65%) review of the Optics Assembly Building (OAB) Optical Assembly and Alignment Systems and the Transport and Handling 35% Title II Review. A key milestone was completed by getting the LRU and installation schedule under configuration management, including the addition of refurbishing several LRUs per month. In October NIF Procurement awarded two contracts for the Phase 1 Conceptual Design of the Laser Bay Transport System. By the end of the first quarter, the Phase 1 designs were complete at both contractors (RedZone Robotics, Inc. and Mentor AGVS), and the Conceptual Design documents were received. The assembly of the hardware for the cover removal mechanism for the Bottom Loading (BL) Universal Canister was completed, and "dirty testing" of the cover removal has been initiated. The BL canister nitrogen gas purge testing has also started. Eighty percent of the OAB Special Equipment prototype equipment has been procured, and cleanliness and function testing is beginning.

Start-Up Activities

The updated IPS database was functional on October 31, with over 10,000 activities, and is now being used to status the Project each month. The IPS includes Level 0–4 Project milestones, interfaces, and detailed activities; integrates key technology activities and milestones; and includes FY98 Cost Account Plan schedules. To supplement the IPS, a detailed LRU installation plan (in the form of a chart) has been developed, which describes the number of LRUs of each type to be installed on a monthly basis throughout the Special Equipment installation phase of the Project. Early in the quarter the first bundle working group progressed through an initial discussion and flow diagram of all integrated operational test procedures for first laser bundle start-up. Procedures reviewed during October include the Diagnostic Target Shot procedures, the Precision Diagnostics, the Computer Controls System requirements, Target Area Beam Transport, Final Optics Assembly, beam alignment to Target Chamber Center, and an update on the Main Laser activation steps. Several first quarter Start-Up weekly meetings discussed the coordination with NIF/ICF Program ignition planning efforts. An update on hohlraum energetics experiments and backscatter diagnostics planning was presented, followed by a discussion of start-up test criteria and expected laser performance at completion of a laser bundle start-up.

Optics Technology

Key enabling technology areas are coming to critical demonstration points in the second quarter, and the Optics Technology organization is now shifting its focus from the facilitization contracts, which are proceeding without significant problems, towards those demonstrations and preparation for the pending pilot production effort. Tinsley presented its revised facilitization plan based on a delay until March for the beginning of site preparation due to the current weather. To preserve the pilot production schedule, Tinsley has proposed performing its NIF equipment acceptance testing in its existing facility, and then transferring the equipment to the NIF facility in August 1998. Schott's phase II building is now completely enclosed, which will allow them to complete the construction on schedule without weather delays. Hoya's new facility has the offices, conference room, and elevator completed except for furnishings. The Zygo facility modifications are 94% complete, with most of the work remaining in the shipping receiving area. Assembly of the first relay plane machine was completed; a Zygo review team conducted an acceptance audit; and the machine was found to be acceptable. The contract to retrofit and refurbish the 160" continuous polisher at Eastman Kodak has been awarded, and the work is expected to be complete by May. Tinsley has completed a second high-speed lapping and polishing machine as part of lens development. This machine is the third and final of its type to be built during NIF development at Tinsley and incorporates advancements learned from the design, build, and operation of the previous machines. Many of the long-lead components for the four new 1000-L tanks have arrived at LLNL. One of the four glass vessels is at LLNL, the other three are expected to arrive in late January. All four water bath housings, all support framework/spider systems, and nearly all of the control and diagnostic equipment are on site. LLNL has selected coating vendors for opening negotiations for the coating facilitization contract awards. The first full-sized color separation grating was completed and delivered on schedule to Beamlet in November. The part exceeded specifications with <1% 1ω and 2ω zero order transmission. At 92% transmission in the 3ω zero order, it missed the specification of >95%. No antireflection coating is currently known to be compatible with the NIF 3ω fluence targets of 14 J/cm^2 . A plan has been defined to evaluate scandia/silica antireflective coatings from the University of Rochester Laboratory for Laser Energetics and spin-coated sol-gel coatings done at LLNL. Also this quarter, initial inspection of existing 7940/7980 shows <80 μm inclusions have existed in significant quantity in at least some Nova

optics. Evidence was also found that $<30\text{ }\mu\text{m}$ inclusions have damage in the hottest spot on Nova (input SF7 lens), but these bulk damage sites did not grow to $>35\text{ }\mu\text{m}$ at the 1ω fluence of $\sim 15\text{ J/cm}^2$.

Upcoming Major Activities

During the second quarter of FY98, Conventional Facilities construction will complete the Target Bay mat foundations and the backfill of the mass excavation

around the Target Bay. Work on the Optics Assembly Building will begin, and the "Notice to Proceed" will be given for Construction Subcontract Package 9, Laser Building & Central Plant. Special Equipment will continue with several Mid-Title II (65%) Design Reviews, and Title II (100%) Design Reviews will take place in the area of computer systems. In Optics, the activities for bidding and negotiating the optics facilitization contracts will continue.

PUBLICATIONS AND PRESENTATIONS

OCTOBER–DECEMBER 1997

A

Afeyan, B. B., Chou, A. E., Kruer, W. L., Matte, J. P., and Town, R. P. J., *Kinetic Theory of Electron Plasma and Ion Acoustic Waves in Nonuniformly Heated Laser-Plasmas*, Lawrence Livermore National Laboratory, Livermore, CA, UCRL-JC-128687; *Phys. Rev. Lett.* **80** (11), 2322–2325 (1998).

Afeyan, B. B., and Williams, E. A., *A Variational Approach to Parametric Instabilities in Inhomogeneous Plasmas I: Two Model Problems*, Lawrence Livermore National Laboratory, Livermore, CA, UCRL-JC-125312; *Phys. Plasmas* **4**(11), 3788–3802 (1997).

Afeyan, B. B., and Williams, E. A., *A Variational Approach to Parametric Instabilities in Inhomogeneous Plasmas II: Stimulated Raman Scattering*, Lawrence Livermore National Laboratory, Livermore, CA, UCRL-JC-125313; *Phys. Plasmas* **4**(11), 3803–3826 (1997).

Afeyan, B. B., and Williams, E. A., *A Variational Approach to Parametric Instabilities in Inhomogeneous Plasmas III: Two-Plasmon Decay*, Lawrence Livermore National Laboratory, Livermore, CA, UCRL-JC-125314; *Phys. Plasmas* **4**(11), 3827–3844 (1997).

Afeyan, B. B., and Williams, E. A., *A Variational Approach to Parametric Instabilities in Inhomogeneous Plasmas IV: The Mixed Polarization High-Frequency Instability*, Lawrence Livermore National Laboratory, Livermore, CA, UCRL-JC-125315; *Phys. Plasmas* **4**(11), 3845–3862 (1997).

Amendt, P., Bailey, D. S., Celliers, P. M., Glinsky, M. E., Ho, D., London, R. A., Maitland, D. J., Strauss, M., Visuri, S. R., and Young, D. A., *Simulation Studies of Vapor Bubble Generation by Short-Pulse Lasers*, Lawrence Livermore National Laboratory, Livermore, CA, UCRL-JC-126822. Prepared for *BiOS Europe '97*, San Remo, Italy, Sept 4, 1997.

B

Back, C. A., Lee, R. W., Libby, S. B., and Woolsey, N. C., *High Energy Density Implosion Dynamics of Ar-Doped Capsules*, Lawrence Livermore National Laboratory, Livermore, CA, UCRL-JC-129239 ABS. Prepared for *Joint Operations Weapons Operations Group 37*, Los Alamos, NM, Feb 2, 1998.

Banks, P. S., Armstrong, J. P., Feit, M. D., Lee, R. S., Myers, B. R., Nguyen, H., Perry, M. D., Roeske, F., Rubenchik, A. M., and Stuart, B. C., *Pemtosecond Laser Machining*, Lawrence Livermore National Laboratory, Livermore, CA, UCRL-JC-129007 ABS & SUM. Prepared for the *Conf on Lasers and Electro-Optics '98*, San Francisco, CA, May 3, 1998.

Bibeau, C., and Payne, S. A., *Picosecond Nonradiative Processes in Neodymium-Doped Crystals and Glasses: Mechanism for the Energy Gap Law*, Lawrence Livermore National Laboratory, Livermore, CA, UCRL-JC-128623. Submitted to *J. of Luminescence*.

Browning, D., Crane, J. K., Dane, C. B., Henesian, M., Martinez, M., Moran, B., Penko, F., Rothenberg, J., and Wilcox, R. B., *Integrated Optical Pulse Generation System for the National Ignition Facility (NIF) Laser System*, Lawrence Livermore National Laboratory, Livermore, CA, UCRL-JC-128851 SUM. Prepared for the *Conf on Lasers and Electro-Optics '98*, San Francisco, CA, May 3, 1998.

Budil, K. S., Farley, D. R., Murray, S., Peyser, T. A., Remington, B. A., and Weber, S. V., *Nonlinear Rayleigh–Taylor and Richtmyer–Meshkov Mixing Experiments at Nova*, Lawrence Livermore National Laboratory, Livermore, CA, UCRL-JC-125441. Prepared for the *11th Biennial Nuclear Explosives Design Physics Conf*, Livermore, CA, Oct 20, 1997.

Budil, K. S., Perry, T. S., Peyser, T. A., Remington, B. A., and Weber, S. V., *Classical Rayleigh–Taylor Instability Experiments at Nova*, Lawrence Livermore National Laboratory, Livermore, CA, UCRL-JC-128019. Prepared for the 39th Annual Mtg of the American Physical Society Div of Plasma Physics, Pittsburgh, PA, Nov 17, 1997.

C

Camp, D. W., Dovik, M., Kozlowski, M. R., Nichols, M., Raether, R., Sheehan, L. M., and Thomas, I., *Subsurface Damage and Polishing Compound Affect the 355-nm Laser Damage Threshold of Fused Silica Surfaces*, Lawrence Livermore National Laboratory, Livermore, CA, UCRL-JC-129301. Prepared for the 29th Annual Boulder Damage Symp, Boulder, CO, Oct 6, 1997.

Campbell, E. M., Holmes, N. C., Libby, S. B., Remington, B. A., and Teller, E., *The Evolution of High Energy-Density Physics: From Nuclear Testing to the Superlasers*, Lawrence Livermore National Laboratory, Livermore, CA, UCRL-JC-124258; *Laser and Part. Beams* **15**(4), 607–626 (1997).

Campbell, E. M., and Remington, B. A., *NIF: an Experimental Facility for Thermonuclear Fusion and High Energy Density Science*, Lawrence Livermore National Laboratory, Livermore, CA, UCRL-JC-128821 ABS. Prepared for the 14th Annual Mtg of the Japanese Society of Plasma Science and Nuclear Fusion Research, Osaka, Japan, Nov 25, 1997.

Chang, J. J., Bass, I. L., Cochran, C. W., Dragon, E. P., and Ebberts, C. A., *Diode-Pumped Nd:YAG Laser Oscillator with 430 W of IR and 160 W of Green Output*, Lawrence Livermore National Laboratory, Livermore, CA, UCRL-JC-128818 ABS & SUM. Prepared for the 13th Topical Mtg on Advanced Solid-State Lasers, Coeur d'Alene, ID, Feb 2, 1998.

Collins, G. W., Budil, K. S., Cauble, R., Celliers, P., Da Silva, L. B., Foord, M., Gold, D., Holmes, N. C., Ross, M., and Stewart, R., *Equation of State Measurements of Hydrogen Isotopes on Nova*, Lawrence Livermore National Laboratory, Livermore, CA, UCRL-JC-129033. Prepared for the 39th Annual Mtg of the American Physical Society Div of Plasma Physics, Pittsburgh, PA, Nov 17, 1997.

Collins, G. W., Budil, K. S., Cauble, R., Celliers, P., Da Silva, L. B., Foord, M., Gold, D., Hammel, B. A., Holmes, N. C., and Stewart, R., *Shock Temperature and Optical Emission Measurements of H₂ and D₂ along the Principle Hugoniot up to 2 Mbar*, Lawrence Livermore National Laboratory, Livermore, CA, UCRL-JC-129242 ABS. Prepared for the 1998 American Physical Society March Mtg, Los Angeles, CA, Mar 16, 1998.

D

Dane, C. B., Daly, J., Hackel, L. A., and Harrisson, J., *Laser Peening of Metals Enabling Laser Technology*, Lawrence Livermore National Laboratory, Livermore, CA, UCRL-JC-129029. Prepared for the Materials Research Society 1997 Fall Mtg, Boston, MA, Dec 1, 1997.

De Yoreo, J. J., Land, T. A., Lee, J. D., and Orme, C., *Investigating the Surface Morphology and Growth Dynamics of Solution-Based Crystals Using the AFM*, Lawrence Livermore National Laboratory, Livermore, CA, UCRL-JC-129021 ABS. Prepared for the Gordon Research Conf, Thin Film and Crystal Growth Mechanisms, Plymouth, NH, Jul 6, 1997.

De Yoreo, J. J., Land, T. A., Mc Bride, M., Orme, C., and Palmore, J. T., *Investigating the Evolution of Crystal Growth Morphology and Kinetics from Small to Large Molecules Using In Situ Atomic Force Microscopy*, Lawrence Livermore National Laboratory, Livermore, CA, UCRL-JC-129226 ABS. Prepared for the 7th Intl Conf on the Crystallisation of Biological Macromolecules, Granada, Spain, May 3, 1998.

De Yoreo, J. J., Land, T. A., Rashkovich, L. N., Onischenko, T. A., Lee, J. D., Monovskii, O. V., and Zaitseva, N. P., *The Effect of Dislocation Cores on Growth Hillock Vicinality and Normal Growth Rates of KDP {101} Surfaces*, Lawrence Livermore National Laboratory, Livermore, CA, UCRL-JC-126010; *J. Crystal Growth* **182** (3–4), 442–460 (1997).

Dimonte, G., and Schneider, M., *Turbulent Richtmyer–Meshkov Instability Experiments with Strong Radiatively Driven Shocks*, Lawrence Livermore National Laboratory, Livermore, CA, UCRL-JC-126452; *Phys. Plasmas* **4**(12), 4347–4357 (1997).

Dittrich, T. R., Bradley, P. A., Haan, S. W., Hoffman, N. M., Marinak, M. M., McEachern, R. L., Pollaine, S. M., and Wilson, D. C., *Capsule Design for the National Ignition Facility*, Lawrence Livermore National Laboratory, Livermore, CA, UCRL-JC-129247 ABS. Prepared for the Joint Operations Weapons Operations Group, Los Alamos, NM, Feb 2, 1998.

Dittrich, T. R., Tipton, R. E., and Vantine, H. C., *Some Centurion Experiments Revisited*, Lawrence Livermore National Laboratory, Livermore, CA, UCRL-JC-129248 ABS. Prepared for the *Joint Operations Weapons Operations Group*, Los Alamos, NM, Feb 2, 1998.

F

Farmer, J. C., Chase, L., Erlandson, A., Gregg, H., Honea, E., Marshall, C., Parham, T., Payne, S., Siekhaus, W., and Thomas, N., *Atmospheric Tarnishing of Silver-Plated Laser Mirrors*, Lawrence Livermore National Laboratory, Livermore, CA, UCRL-ID-128599.

Feit, M. D., Campbell, J., Faux, D., Genin, F. Y., Kozlowski, M. R., Riddle, R., Rubenchik, A. M., Salleo, A., and Yoshiyama, J., *Modeling of Laser-Induced Surface Cracks in Silica at 355 nm*, Lawrence Livermore National Laboratory, Livermore, CA, UCRL-JC-128363. Prepared for the *29th Annual Symp on Optical Materials for High Power Lasers*, Boulder, CO, Oct 6, 1997.

Feit, M. D., Eimerl, D., Rubenchik, A. M., and Salleo, A., *Pulse Shape and Pulelength Scaling of ns Pulse Laser Damage Threshold due to Rate Limiting by Thermal Conduction*, Lawrence Livermore National Laboratory, Livermore, CA, UCRL-JC-128364. Prepared for the *29th Annual Symp on Optical Materials for High Power Lasers*, Boulder, CO, Oct 6, 1997.

Feit, M. D., Genin, F. Y., Rubenchik, A. M., and Salleo, A., *Grey Haze: Micropit Laser Initiated Surface Damage in Fused Silica*, Lawrence Livermore National Laboratory, Livermore, CA, UCRL-JC-129005 ABS. Prepared for the *Conf on Lasers and Electro-Optics '98*, San Francisco, CA, May, 3, 1998.

Feit, M. D., Komashko, A. M., Perry, M. D., Rubenchik, A. M., and Stuart, B. C., *Modeling of Ultrashort Laser Pulse Material Processing*, Lawrence Livermore National Laboratory, Livermore, CA, UCRL-JC-129006 ABS. Prepared for the *Conf on Lasers and Electro-Optics '98*, San Francisco, CA, May, 3, 1998.

Fernandez, A., Decker, J. Y., Herman, S. M., Phillion, D. W., Sweeney, D. W., and Perry, M. D., *Methods for Fabricating Arrays of Holes Using Interference Lithography*, Lawrence Livermore National Laboratory, Livermore, CA, UCRL-JC-125997; *J. Vac. Sci. Technol. B* **15**(6), 2439–2443 (1997).

G

Genin, F. Y., Dijon, J., Garrec, P., Sheehan, L., and Yoshiyama, J., *Statistical Study of UV Laser-Induced Failure of Fused Silica*, Lawrence Livermore National Laboratory, Livermore, CA, UCRL-JC-129274. Prepared for the *29th Annual Symp on Optical Materials for High Power Lasers*, Boulder, CO, Oct 6, 1997.

Glenzer, S. H., Blain, M. A., Dixit, S. N., Estabrook, K. G., Hammel, B. A., Kauffman, R. L., Kirkwood, R. K., MacGowan, B. J., Suter, L. J., and Turner, R. E., *Energetics of Inertial Confinement Fusion Hohlraum Plasmas*, Lawrence Livermore National Laboratory, Livermore, CA, UCRL-JC-129236; *Phys. Rev. Lett.* **80** (13), 2845–2848 (1998).

H

Hinkel, D. E., Berger, R. L., Langdon, A. B., Powers, L. V., Still, C. H., and Williams, E. A., *Propagation of Realistic Beams in Underdense Plasma*, Lawrence Livermore National Laboratory, Livermore, CA, UCRL-JC-129025. Prepared for the *39th Annual Mtg of the American Physical Society Div of Plasma Physics*, Pittsburgh, PA, Nov 17, 1997.

K

Kalantar, D. H., Chandler, E. A., Colvin, J. D., Remington, B. A., Weber, S. V., and Wiley, L. G., *Developing Solid State Hydrodynamics Experiments on the Nova Laser*, Lawrence Livermore National Laboratory, Livermore, CA, UCRL-JC-129244 ABS. Prepared for the *Joint Operations Weapons Operations Group*, Los Alamos, NM, Feb 2, 1998.

Kalantar, D. H., Chandler, E. A., Colvin, J. D., Failor, B. H., Hauer, A., Lee, R., Remington, B. A., Wark, J. S., Weber, S. V., and Wiley, L. G., *Transient X-Ray Diffraction of Shock Compressed Crystals Using the Nova Laser*, Lawrence Livermore National Laboratory, Livermore, CA, UCRL-JC-129270 ABS. Prepared for the *1998 American Physical Society March Mtg*, Los Angeles, CA, Mar 16, 1998.

Kane, J. O., Arnett, D., Drake, R. P., Glendinning, S. G., Remington, B. A., and Rubenchik, A., *Supernova Experiments on the Nova Laser*, Lawrence Livermore National Laboratory, Livermore, CA, UCRL-JC-129000 ABS. Prepared for the *2nd Oak Ridge Symp on Atomic and Nuclear Astrophysics*, Oak Ridge, TN, Dec 2, 1997.

Kane, J. O., Arnett, D., Drake, R. P., Fryxell, B., Glendinning, S. G., Muller, E., Remington, B. A., and Rubenchik, A., *Supernova Hydrodynamics Experiments on the Nova Laser*, Lawrence Livermore National Laboratory, Livermore, CA, UCRL-JC-129001 ABS. Prepared for the 91st Mtg of the American Astronomical Society, Washington, DC, Jan 6, 1998.

Kauffman, R. L., Dixit, S. N., Glendinning, S. G., Glenzer, S. H., Landen, O. L., MacGowan, B. J., Moody, J. D., Orzechowski, T. J., Pennington, D. M., and Powers, L. V., *Improved Gas-Filled Hohlraum Performance on Nova with Beam Smoothing*, Lawrence Livermore National Laboratory, Livermore, CA, UCRL-JC-128004. Prepared for the 39th Annual Mtg of the American Physical Society Div of Plasma Physics, Pittsburgh, PA, Nov 17, 1997.

Key, M. H., Estabrook, K., Hammel, B., Hatchett, S., Hinkel, D., Kilkenny, J., Koch, J., Kruer, W., Langdon, B., and Lasinski, B., *Hot Electron Production and Heating by Hot Electrons in Fast Ignitor Research*, Lawrence Livermore National Laboratory, Livermore, CA, UCRL-JC-129251. Prepared for the 39th Annual Mtg of the American Physical Society Div of Plasma Physics, Pittsburgh, PA, Nov 17, 1997.

Kirkwood, R. K., Afeyan, B. B., Estabrook, K. G., Glenzer, S. H., Kruer, W. L., MacGowan, B. J., Montgomery, D. S., Moody, J. D., Wharton, K. B., and Williams, E. A., *Observation of the Saturation of Langmuir Waves Driven by Ponderomotive Force in a Large Scale Plasma*, Lawrence Livermore National Laboratory, Livermore, CA, UCRL-JC-128298. Submitted to *Phys. Rev. Lett.*

Kozlowski, M. R., Camp, D., Carr, J., Hutcheon, I., Sheehan, L., Torres, R., and Yann, M., *Depth Profiling of Polishing-Induced Contamination on Fused Silica Surfaces*, Lawrence Livermore National Laboratory, Livermore, CA, UCRL-JC-128355. Prepared for the 29th Annual Symp on Optical Materials for High Power Lasers, Boulder, CO, Oct 6, 1997.

Kruer, W. L., Afeyan, B. B., Chou, A. E., Kirkwood, R. K., Montgomery, D. S., Rambo, P. W., and Wilks, S. C., *Interplay between Laser Plasma Instabilities*, Lawrence Livermore National Laboratory, Livermore, CA, UCRL-JC-129036. Submitted to *Physica Scripta*.

L

Landen, O. L., Bauer, J., Carman, T. S., Hammer, J. A., Koch, J., Nowak, D., Orzechowski, T. J., Perry, T. S., Suter, L. J., and Weiland, T., *Supersonic Diffusive Transport Studies at Nova*, Lawrence Livermore National Laboratory, Livermore, CA, UCRL-JC-129035 ABS. Prepared for Joint Operations Weapons Operations Group 37, Los Alamos, NM, Feb 2, 1998.

Landen, O. L., Edwards, J., Hammer, J. A., Powers, L., Suter, L. J., and Thomas, B. R., *Analytic Limits for Hohlraum Performance*, Lawrence Livermore National Laboratory, Livermore, CA, UCRL-JC-129238 ABS. Prepared for Joint Operations Weapons Operations Group 37, Los Alamos, NM, Feb 2, 1998.

Langer, S. H., Scott, H. A., Keane, C. J., Landen, O. L., and Marinak, M. M., *Yield and Emission Line Ratios from ICF Target Implosions with Multi-Mode Rayleigh-Taylor Perturbations*, Lawrence Livermore National Laboratory, Livermore, CA, UCRL-JC-124484; *J. Quant. Spectrosc. Radiat. Transfer* **58**(4-6), 709-720 (1997).

Latkowski, J. F., and Phillips, T. W., *Monte Carlo Prompt Dose Calculations for the National Ignition Facility*, Lawrence Livermore National Laboratory, Livermore, CA, UCRL-JC-127604. Prepared for the 17th Institute of Electrical and Electronics Engineers/Nuclear and Plasma Sciences Society Symp on Fusion Engineering, San Diego, CA, Oct 6, 1997.

Leboucher-Dalimier, E., Angelo, P., Gauthier, P., Sauvan, P., Poqueresse, A., Derfoul, H., Ceccotti, T., Back, C. A., Shepard, T. D., Forster, E., Uschmann, I., and Vollbrecht, M., "X-Ray Spectroscopy and Imaging of Hot Dense Plasma Created by Colliding Foils. Simulation of Spectra," *J. Quant. Spectrosc. Radiat Transfer* **58**(4-6), 721-735 (1997).

Logan, B. G., and Callahan, D. A., *Beam Charge and Current Neutralization of High-Charge-State Heavy Ions*, Lawrence Livermore National Laboratory, Livermore, CA, UCRL-JC-127486. Prepared for the 12th Intl Symp on Heavy-Ion Inertial Fusion, Heidelberg, Germany, Sept 17, 1997.

London, R. A., Glinsky, M. E., Zimmerman, G. B., Bailey, D. S., Eder, D. C., and Jacques, S. L., *Laser-Tissue Interaction Modeling with LATIS*, Lawrence Livermore National Laboratory, Livermore, CA, UCRL-JC-126806 ABS; *Appl. Optics* **36**(34), 9068-9074 (1997).

M

Marinak, M. M., Haan, S. W., Dittrich, T. R., Tipton, R. E., and Zimmerman, G. B., *A Comparison of Three-Dimensional Multimode Hydrodynamic Instability Growth on Various National Ignition Facility Capsule Designs with HYDRA Simulations*, Lawrence Livermore National Laboratory, Livermore, CA, UCRL-JC-128862. Submitted to *Phys. of Plasmas*.

Marinak, M. M., Budil, K. S., Glendinning, S. G., Haan, S. W., Kilkenny, J. D., Remington, B. A., Tipton, R. E., and Wallace, R. J., *Nonlinear Rayleigh–Taylor Evolution of a Three-Dimensional Multimode Perturbation*, Lawrence Livermore National Laboratory, Livermore, CA, UCRL-JC-129257 DR; *Phys. Rev. Lett.* **80** (20), 4426–4429 (1998).

Meier, W. R., Bangerter, R. O., and Faltens, A., *Systems Modeling for Heavy Ion Drivers—an Induction Linac Example*, Lawrence Livermore National Laboratory, Livermore, CA, UCRL-JC-128679. Prepared for the 17th Institute of Electrical and Electronics Engineers/Nuclear and Plasma Sciences Society Symp on Fusion Engineering, San Diego, CA, Oct 6, 1997.

Mourou, G., Barty, C. P., and Perry, M., *Ultrahigh-Intensity Laser: Physics of the Extreme on a Tabletop*, Lawrence Livermore National Laboratory, Livermore, CA, UCRL-ID-128698.

Munro, D., and Langer, S., *Yorick a Scientific Analysis Environment*, Lawrence Livermore National Laboratory, Livermore, CA, UCRL-TB-128876. Prepared for *Super Computing '97*, San Jose, CA, Nov 15–20, 1997.

N

Nilsen, J., Zhang, J., MacPhee, A. G., Lin, J., Barbee, Jr., T. W., Danson, C., Da Silva, L. B., Key, M. H., Lewis, C. L. S., Neely, D., O'Rourke, R. M. N., Pert, G. J., Smith, R., Tallents, G. J., Wark, J. S., and Wolfrum, E., *Near-Field Spatial Imaging of a Ni-Like Ag 140-A X-Ray Laser*, Lawrence Livermore National Laboratory, Livermore, CA, UCRL-JC-127446; *Phys. Rev. A* **56**(4), 3161–3165 (1997).

Norton, M. A., Boley, C. D., Murray, J. E., and Sinz, K. H., *Laser Ablation of Stainless Steel from 1 J/cm² to 10 KJ/cm²*, Lawrence Livermore National Laboratory, Livermore, CA, UCRL-JC-128857 ABS & SUM. Prepared for the *Conf on Lasers and Electro-Optics '98*, San Francisco, CA, May 3, 1998.

P

Perry, M. D., Brown, C. G., Cowan, T., Hatchett, S., Hunt, A., Key, M., Moran, M., Pennington, D. M., Phillips, T., and Snavely, R. A., *Nuclear Experiments with Petawatt Class Lasers*, Lawrence Livermore National Laboratory, Livermore, CA, UCRL-JC-129003 ABS & SUM. Prepared for the *Conf on Lasers and Electro-Optics '98*, San Francisco, CA, May 3, 1998.

Phillion, D. W., "General Methods for Generating Phase-Shifting Interferometry Algorithms," *Appl. Optics* **36**(31), 8098–8115 (1997).

Pollaine, S. M., and Eimerl, D., *Modal Analysis of Power Imbalance and Pointing Errors for Direct Drive and Tetrahedral Hohlraums*, Lawrence Livermore National Laboratory, Livermore, CA, UCRL-JC-129272. Submitted to *Nuclear Fusion*.

Potapenko, S. Y., De Yoreo, J. J., and Robey, H. F., *Lateral Instability of Macrosteps during Growth from Solution*, Lawrence Livermore National Laboratory, Livermore, CA, UCRL-JC-129048 ABS. Prepared for the 12th Intl Conf on Crystal Growth, Jerusalem, Israel, Jul 26, 1997.

Potapenko, S. Y., Feeney, R. E., and Yeh, Y., *Percolation Model for Antifreeze Glycoprotein Effect on Ice Growth*, Lawrence Livermore National Laboratory, Livermore, CA, UCRL-JC-129049 ABS. Prepared for the 12th Intl Conf on Crystal Growth, Jerusalem, Israel, Jul 26, 1998.

Powers, L. V., Glendinning, S. G., Kauffman, R. L., Landen, O. L., Ress, D. B., Suter, L. J., and Zimmerman, G. B., *Modeling of Soft X-Ray Emission Profiles in Nova Hohlraums*, Lawrence Livermore National Laboratory, Livermore, CA, UCRL-JC-128612. Submitted to *Phys. of Plasma*.

R

Remington, B. A., Budil, K. S., Estabrook, K., Glendinning, S. G., Kane, J., London, R., Managan, R. A., Rubenchik, A., Ryutov, D., and Wallace, R. J., *Supernova Hydrodynamics Experiments on Nova*, Lawrence Livermore National Laboratory, Livermore, CA, UCRL-JC-128863. Prepared for the *Intl Conf on Superstrong Fields in Plasmas*, Varenna, Italy, Aug 27, 1997.

Robey, H. F., and Maynes, D., *Numerical Simulation of the Fluid Dynamics and Mass Transfer in the Rapid Growth of Large KDP Crystals*, Lawrence Livermore National Laboratory, Livermore, CA, UCRL-JC-129254 ABS. Prepared for the 50th Annual Mtg of the American Physical Society Div of Fluid Dynamics, San Francisco, CA, Nov 23, 1997.

Rothenberg, J. E., Moran, B., Wegner, P., and Weiland, T., *Performance of Smoothing by Spectral Dispersion (SSD) with Frequency Conversion on the Beamlet Laser for the National Ignition Facility*, Lawrence Livermore National Laboratory, Livermore, CA, UCRL-JC-128870. Prepared for the *Conf on Lasers and Electro-Optics '98*, San Francisco, CA, May 5, 1998.

Runkel, M., De Yoreo, J., Yan, M., and Zaitseva, N., *Effect of Impurities and Stress on the Damage Distributions of Rapidly Grown KDP Crystals*, Lawrence Livermore National Laboratory, Livermore, CA, UCRL-JC-128091. Prepared for the *29th Annual Boulder Damage Symp*, Boulder, CO, Oct 6, 1997.

Runkel, M., De Yoreo, J., Milam, D., and Sell, W., *Laser Conditioning Study of KDP on the Optical Sciences Laser Using Large Area Beams*, Lawrence Livermore National Laboratory, Livermore, CA, UCRL-JC-128352. Prepared for the *29th Annual Boulder Damage Symp*, Boulder, CO, Oct 6, 1997.

S

Salleo, A., Genin, F. Y., Kozlowski, M. R., Stolz, C. J., and Yoshiyama, J., *Laser-Induced Damage of Fused Silica at 355 nm Initiated at Scratches*, Lawrence Livermore National Laboratory, Livermore, CA, UCRL-JC-128361. Prepared for *29th Annual Symp on Optical Materials for High Power Lasers*, Boulder, CO, Oct 6, 1997.

Sanz, J., and Balmisa, J. M., *ACAB Software Upgrade*, Lawrence Livermore National Laboratory, Livermore, CA, UCRL-CR-128874.

Sheehan, L. M., Camp, D. W., and Kozlowski, M. R., *Application of Total Internal Reflection Microscopy for Laser Damage Studies on Fused Silica*, Lawrence Livermore National Laboratory, Livermore, CA, UCRL-JC-128356. Prepared for the *29th Annual Symp on Optical Materials for High Power Lasers*, Boulder, CO, Oct 6, 1997.

Small, W., Celliers, P. M., Eder, D. C., Heilbron, M., Heredia, N. J., Hussain, F., Kopchok, G. E., London, R. A., Maitland, D. J., and Reiser, K. M., *Temperature Feedback and Collagen Crosslinking in Argon Laser Vascular Welding*, Lawrence Livermore National Laboratory, Livermore, CA, UCRL-JC-128615. Submitted to *Lasers in Medical Science*.

Springer, P. T., Wong, K. L., Iglesias, C. A., Hammer, J. H., Porter, J. L., Toor, A., Goldstein, W. H., Wilson, B. G., Rogers, F. J., Deeney, C., Dearborn, D. S., Bruns, C., Emig, J., and Stewart, R. E., *Laboratory Measurement of Opacity for Stellar Envelopes*, Lawrence Livermore National Laboratory, Livermore, CA, UCRL-JC-127171; *J. Quant. Spectro. Radiat. Transfer* **58**(4-6), 927-935 (1997).

T

Tabak, M., and Callahan-Miller, D., *Design of a Distributed Radiator Target for Inertial Fusion Driven from Two Sides with Heavy Ion Beams*, Lawrence Livermore National Laboratory, Livermore, CA, UCRL-JC-128366 Rev 1. Submitted to *Nuclear Instruments and Methods*.

Tabak, M., and Callahan-Miller, D., *Design of a Distributed Radiator Target for Inertial Fusion Driven from Two Sides with Heavy Ion Beams*, Lawrence Livermore National Laboratory, Livermore, CA, UCRL-JC-128366 Rev 2. Prepared for the *39th Annual Mtg of the American Physical Society Div of Plasma Physics*, Pittsburgh, PA, Nov 17, 1997.

Tabak, M., Callahan-Miller, D., Ho, D. D.-M., and Zimmerman, G. B., *Design of a Distributed Radiator Target for Inertial Fusion Driven from Two Sides with Heavy Ion Beams*, Lawrence Livermore National Laboratory, Livermore, CA, UCRL-JC-128366 Rev 3. Submitted to *Nuclear Fusion*.

Tietbohl, G. L., Bell, P. M., Hamilton, R. M., Horner, J. B., Horton, R. L., Ludwigsen, A. P., Miller, J. L., Olson, W. H., Patel, C. S., and Pennington, D. M., *Engineering the Petawatt Laser into Nova*, Lawrence Livermore National Laboratory, Livermore, CA, UCRL-JC-127749. Prepared for *Optoelectronics and High-Power Lasers & Applications Conf*, San Jose, CA, Jan 24, 1998.

Tokheim, R. E., Curran, D. R., and Seaman, L., *Damage and Hardening Assessments for the National Ignition Facility Target Chamber Design*, Lawrence Livermore National Laboratory, Livermore, CA, UCRL-CR-128686 DR.

W

Wegner, P. J., Auerbach, J. M., Barker, C. E., Brading, K. R., Britten, J. A., Burkhart, S. C., Caird, J. A., Dixit, S. N., Feru, P., and Hennesian, M. A., *Recent Performance Results of the Beamlet Prototype for the National Ignition Facility*, Lawrence Livermore National Laboratory, Livermore, CA, UCRL-JC-128858 ABS & SUM. Prepared for the *Conf on Lasers and Electro-Optics '98*, San Francisco, CA, May 3, 1998.

Wharton, K., Hammel, B., Hatchett, S., Joshi, C., Key, M., Moody, J., Offenberger, A. A., Perry, M., Wilks, S., and Yanovsky, V., *Experimental Measurements of Hot Electrons Generated by Ultra-Intense ($>10^{19}$ W/cm²) Laser-Plasma Interactions on Solid Density Targets*, Lawrence Livermore National Laboratory, Livermore, CA, UCRL-JC-129230. Submitted to *Phys. Rev. Lett.*

Widmayer, C. C., Milam, D., and deSzoeko, S. P., *Nonlinear Formation of Holographic Images of Obscurations in Laser Beams*, Lawrence Livermore National Laboratory, Livermore, CA, UCRL-JC-126969; *Appl. Optics* **36**(36), 9342–9347 (1997).

Wilcox, R. B., Browning, D. F., Feit, M. D., and Nyman, B., *Two-Stage, Co-Pumped Yb:Silica Fiber Amplifiers*, Lawrence Livermore National Laboratory, Livermore, CA, UCRL-JC-128822 ABS & SUM. Prepared for the *Conf on Lasers and Electro-Optics '98*, San Francisco, CA, May 3, 1998.

Wilks, S. C., and Kruer, W. L., *Absorption of Ultra-Short, Ultra-Intense Laser Light by Solids and Overdense Plasmas*, Lawrence Livermore National Laboratory, Livermore, CA, UCRL-JC-125205; *IEEE J. Quant. Elect.* **33**(11), 1954–1968 (1997).

Wood-Vasey, W. M., Berning, M., Budil, K. S., Kane, J., Larsen, J. T., Mikaelian, K. O., Miller, P. L., Peyser, T. A., Remington, B. A., and Rubenchik, A. M., *Computation Modeling of Classical and Ablative Rayleigh–Taylor and Richtmyer–Meshkov Instabilities*, Lawrence Livermore National Laboratory, Livermore, CA, UCRL-JC-129017. Submitted to *Phys. of Plasmas*.

Woods, B., De Yoreo, J., Kozlowski, M., Radousky, H., Wu, Z., and Yan, M., *Photothermal Mapping of Defects in the Study of Bulk Damage in KDP*, Lawrence Livermore National Laboratory, Livermore, CA, UCRL-JC-128353. Prepared for *29th Annual Boulder Damage Symp*, Boulder, CO, Oct 6, 1997.

Woolsey, N. C., Hammel, B. A., Keane, C. J., Back, C. A., Moreno, J. C., Nash, J. K., Calisti, A., Mosse, C., Godbert, L., Stamm, R., Talin, B., Hooper, C. F., Asfaw, A., Klein, L. S., and Lee, R. W., "Spectroscopic Line Shape Measurements at High Densities," *J. Quant. Spectr. & Rad. Trans.* **58**(4-6), 975–989 (1997).

Y

Yan, M., Carman, L., De Yoreo, J. J., Torres, R., Weston, L., and Zaitseva, N. P., *Molecular Defects in KDP Crystals*, Lawrence Livermore National Laboratory, Livermore, CA, UCRL-JC-129022 ABS. Prepared for the *12th Intl Conf on Crystal Growth and the 10th Intl Conf on Vapor Growth and Epitaxy*, Jerusalem, Israel, Jul 26, 1998.

Yoshiyama, J., Camp, D. W., Genin, F. Y., Hutcheon, I. D., Kozlowski, M. R., Salleo, A., Sheehan, L. M., and Thomas, I., *Study of the Effects of Polishing, Etching, Cleaving, and Water Leaching on the UV Laser Damage of Fused Silica*, Lawrence Livermore National Laboratory, Livermore, CA, UCRL-JC-129275. Prepared for the *29th Annual Symp on Optical Materials for High Power Lasers*, Boulder, CO, Oct 6, 1997.

Young, B. K. F., Wilson, B. G., Zimmerman, G. B., Price, D. F., and Stewart, R. E., *Generation and Modeling of Near-LTE Plasmas Using Ultrashort Pulse Laser Heated, Tamped Mid-Z Targets*, Lawrence Livermore National Laboratory, Livermore, CA, UCRL-JC-125388; *J. Quant. Spectro. Radiat. Transfer* **58**(4-6), 991–1000 (1997).

Z

Zaitseva, N., Carman, L., Potapenko, S., Smolsky, I. L., Torres, R., and Yan, M., *Defect Formation during Rapid Growth of Large (40–60) KDP and DKDP Crystals*, Lawrence Livermore National Laboratory, Livermore, CA, UCRL-JC-129024 ABS. Prepared for the *12th Intl Conf on Crystal Growth and the 10th Intl Conf on Vapor Growth and Epitaxy*, Jerusalem, Israel, Jul 26, 1998.

Zapata, L. E., Erlandson, A., Marshall, C., and Rotter, M., *Optical Performance of Large, Flashlamp-Pumped Nd:Glass Amplifier Prototype for the National Ignition Facility*, Lawrence Livermore National Laboratory, Livermore, CA, UCRL-JC-128820 ABS & SUM. Prepared for *Advanced Solid State Lasers and Radiative Processes and Dephasing in Semiconductors Topical Mtg*, Coeur d'Alene, ID, Feb 2, 1998.

Zweiback, J., Ditmire, T., Komashko, A., Perry, M. D., Rubenchik, A. M., and Yanovsky, V., *Pulse Length Effects in Laser Cluster Interactions*, Lawrence Livermore National Laboratory, Livermore, CA, UCRL-JC-129008 ABS & SUM. Prepared for the *Conf on Lasers and Electro-Optics '98*, San Francisco, CA, May 3, 1998.